Heck, Katharina Klara

Modelling and analysis of multicomponent transport at the interface between free- and porous-medium flow - influenced by radiation and roughness

Mitteilungen. Institut für Wasser- und Umweltsystemmodellierung, Universität Stuttgart

Universität Stuttgart

Institut für Wasser- und Umweltsystemmodellierung

Mitteilungen

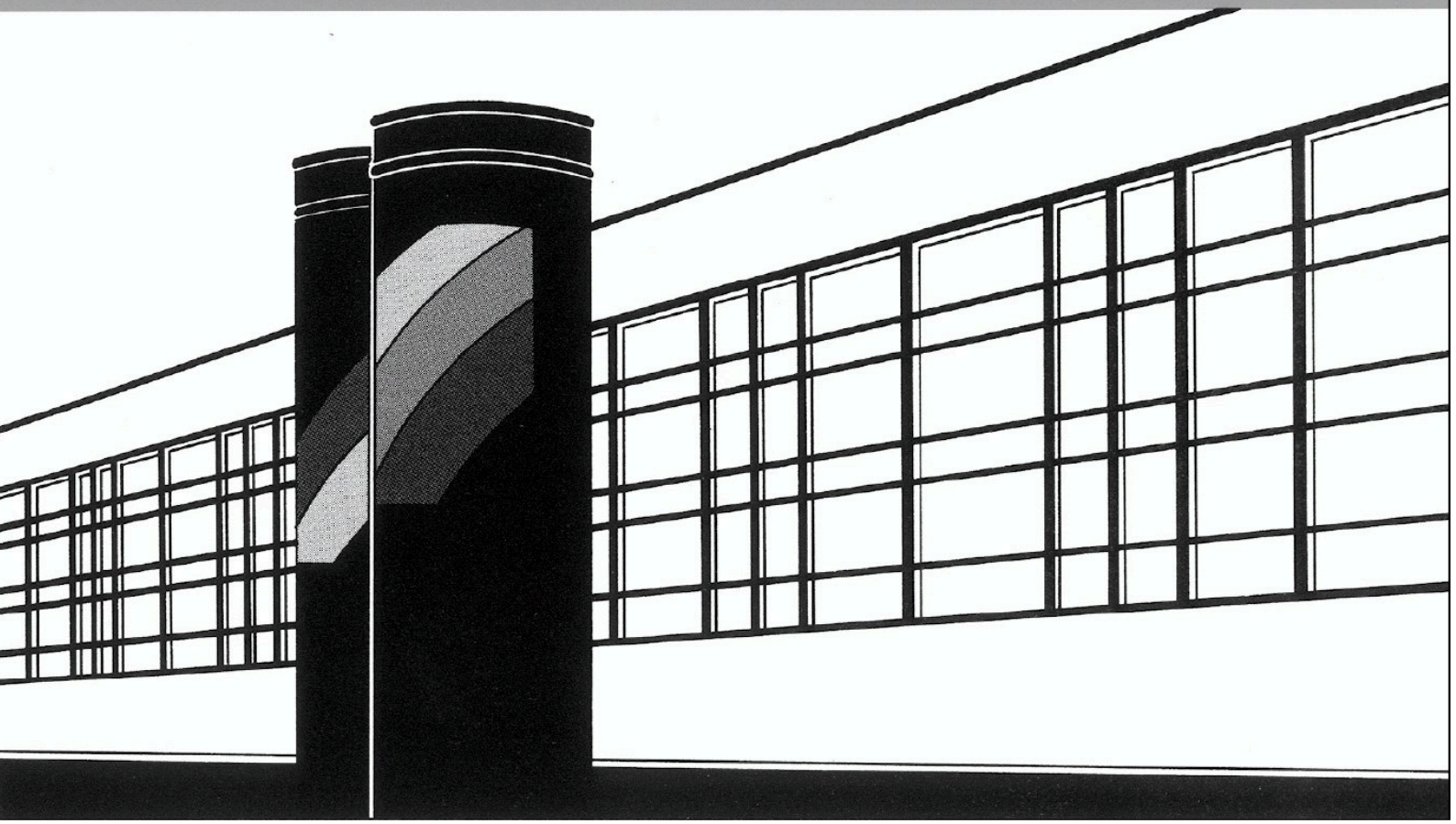

Heft 280 Katharina Klara Heck

Modelling and analysis of multicomponent transport at the interface between free- and porous-medium flow - influenced by radiation and roughness

Modelling and analysis of multicomponent transport at the interface between free- and porous-medium flow - influenced by radiation and roughness

von der Fakultät Bau- und Umweltingenieurwissenschaften der Universität Stuttgart und dem Stuttgart Center for Simulation Science zur Erlangung der Würde einer Doktor-Ingenieurin (Dr.-Ing.) genehmigte Abhandlung

vorgelegt von

Katharina Klara Heck

aus Göppingen, Deutschland

Hauptberichter:	Prof. Dr.-Ing. Rainer Helmig
Mitberichter:	Prof. Dr.-Ing. Joachim Groß
	Prof. Dr. sc. nat. ETH Insa Neuweiler

Tag der mündlichen Prüfung: 17.12.2020

Institut für Wasser- und Umweltsystemmodellierung
der Universität Stuttgart
2021

Heft 280

Modelling and analysis of multicomponent transport at the interface between free- and porous-medium flow - influenced by radiation and roughness

von
Dr.-Ing.
Katharina Klara Heck

Eigenverlag des Instituts für Wasser- und Umweltsystemmodellierung
der Universität Stuttgart

D93 **Modelling and analysis of multicomponent transport at the interface between free- and porous-medium flow - influenced by radiation and roughness**

Bibliografische Information der Deutschen Nationalbibliothek
Die Deutsche Nationalbibliothek verzeichnet diese Publikation in der Deutschen Nationalbibliografie; detaillierte bibliografische Daten sind im Internet über http://www.d-nb.de abrufbar

Heck, Katharina Klara:
Modelling and analysis of multicomponent transport at the interface between free- and porous-medium flow – influenced by radiation and roughness, Universität Stuttgart. - Stuttgart: Institut für Wasser- und Umweltsystemmodellierung, 2021

(Mitteilungen Institut für Wasser- und Umweltsystemmodellierung, Universität Stuttgart: H. 280)
Zugl.: Stuttgart, Univ., Diss., 2021
ISBN 978-3-942036-84-9

NE: Institut für Wasser- und Umweltsystemmodellierung <Stuttgart>: Mitteilungen

Herausgegeben 2021 vom Eigenverlag des Instituts für Wasser- und Umweltsystem-modellierung

Druck: DCC Kästl e.K., Ostfildern

Danksagung

Im Folgenden möchte ich mich bei all jenen bedanken, die mich beim Anfertigen dieser Arbeit begleitet haben. Mein großer Dank gilt dabei im Besonderen Rainer Helmig, der mich stets unterstützt hat und zu jeder Zeit für Diskussionen oder Fragen ein offenes Ohr hatte. Durch seine Begeisterungsfähigkeit und seinen großen Einsatz für seine Mitarbeitenden trägt er sehr viel zur guten Stimmung bei uns am Lehrstuhl bei.
Diese angenehme Arbeitsatmosphäre hat mir geholfen, mich auch in anstrengenden Zeiten mit Begeisterung meiner Arbeit zu widmen. Dazu beigetragen hat natürlich auch die große Unterstützung meiner Kolleginnen und Kollegen in vielen Kaffee- und Mittagspausen und bei der gemeinsamen Arbeit an DuMu^{x}. Ich bin sehr dankbar, Teil dieses tollen Teams zu sein, in dem man sich jederzeit hilft und wertschätzt. Bei Bernd Flemisch möchte ich in diesem Zug vor allem für seine Geduld und Hilfe bei DuMu^{x} bedanken. Holger Class danke ich dafür, dass er sich stets Zeit nimmt, Fragen zu physikalischen Zusammenhängen und fluidmechanischen Grundlagen zu diskutieren und zu erklären. Stefanie Siegert, Prudence Lawday und Beate Spinner danke ich für ihre geduldige Hilfe bei jeglichen administrativen Tätigkeiten und für das offene Ohr bei allen Schwierigkeiten. Für die technische Unterstützung danke ich David Werner und Michelle Hartnick, die jedes Computerproblem schnell und hilfsbereit behoben haben.
Ein großer Dank gebührt auch Joachim Groß, der sich viel Zeit genommen hat, mit mir über kleine und große thermodynamische Fragestellungen zu diskutieren und der mit viel Geduld und Enthusiasmus einen Weg findet, auch komplexe Fragestellungen verständlich zu erklären. Genauso danke ich auch Insa Neuweiler, mit der ich in vielen Projekten sehr gerne zusammengearbeitet habe. Die Diskussionen mit ihr auf Projekttreffen und Onlineterminen haben mir viel geholfen und neue spannende Ideen zu dieser Arbeit beigetragen. I would also like to thank Massimo Rolle, Klaus Mosthaf and Navid Ahmadi for giving me the opportunity to visit them at the DTU and to work together. I learned a lot from all of you and enjoyed the time in Copenhagen very much.
Ein großes Dankeschön auch an meine Familie sowie meine Freundinnen und Freunde, die immer für all meine Freuden und auch Probleme ein offenes Ohr haben. Besonders danke ich meine Eltern, die mich in allen Lebenslagen unterstützen. Mein größter Dank gilt Philipp, der mich auch in stressigen Zeiten zum Lachen bringt und mir Motivation und Rückhalt bietet.
Der Deutschen Forschungsgemeinschaft danke ich für die Förderung des Sonderforschungsbereichs 1313. Das interdisziplinäre Umfeld und die vielen Diskussionen mit anderen Doktorandinnen und Doktoranden haben viel zum Gelingen dieser Arbeit beigetragen.

Contents

List of Figures

List of Tables

Nomenclature

Selected Acronyms

REV	representative elementary volume

Greek Letters

α_ω	$k-\omega$ constant	-
α_{pm}	soil surface albedo	-
α_{VG}	van-Genuchten parameter	Pa^{-1}
β_ω	$k-\omega$ constant	-
β_k	$k-\omega$ constant	-
δ_{ij}	Kronecker delta	-
ϵ_{ff}	atmospheric emissivity	-
ϵ_{pm}	soil surface emissivity	-
η	chemical potential	$\mathrm{J\,mol}^{-1}$
γ	activity coefficient of a component in a mixture	-
λ^{kn}	mean free path of a molecule	m
λ_α	thermal conductivity of the phase	$\mathrm{W\,m}^{-1}\,\mathrm{K}^{-1}$
λ_t	turbulent thermal conductivity	$\mathrm{W\,m}^{-1}\,\mathrm{K}^{-1}$
μ_α^i	dynamic viscosity of the component	$\mathrm{Pa\,s}$
μ_α	dynamic viscosity of the phase	$\mathrm{Pa\,s}$
μ_t	eddy viscosity	$\mathrm{Pa\,s}$
ν_α	kinematic viscosity of the phase	$\mathrm{m}^2\,\mathrm{s}^{-1}$
ω	turbulence frequency	s^{-1}
ϕ	porosity	-
σ_ω	$k-\omega$ constant	-

σ_d	$k-\omega$ function	-
σ_k	$k-\omega$ constant	-
σ_B	Stefan-Boltzmann constant	$\mathrm{W/m^2/K^4}$
θ	soil moisture content	-
$\tilde{\omega}$	$k-\omega$ function	$\mathrm{s^{-1}}$
ϱ	mass density	$\mathrm{kg\,m^{-3}}$
ϱ^i	partial mass density of a component	$\mathrm{kg\,m^{-3}}$
ϱ_m	molar density	$\mathrm{mol\,m^{-3}}$

Vectors and Tensors

$\mathbf{\Gamma}$	matrix of thermodynamic factors	-
τ_g	shear stress tensor	$\mathrm{kg\,s^{-2}\,m^{-1}}$
$\tau_{g,t}$	turbulent shear stress tensor	$\mathrm{kg\,s^{-2}\,m^{-1}}$
$\mathbf{B}$	Maxwell Stefan matrix	$\mathrm{s\,m^{-2}}$
$\mathbf{g}$	gravitational acceleration	$\mathrm{m\,s^{-2}}$
$\mathbf{I}$	identity matrix	-
$\mathbf{J}_{\text{diff}}$	diffusive molar flux	$\mathrm{mol\,s^{-1}}$
$\mathbf{j}_{\text{diff}}$	diffusive mass flux	$\mathrm{kg\,s^{-1}}$
$\mathbf{K}$	intrinsic permeability	$\mathrm{m^2}$
$\mathbf{n}$	normal vector	-
$\mathbf{S}$	strain rate tensor	$\mathrm{s^{-1}}$
$\mathbf{t}_i$	tangential vector	-
$\mathbf{v}$	velocity	$\mathrm{m\,s^{-1}}$
$\mathbf{v}^i$	component velocity	$\mathrm{m\,s^{-1}}$

Roman Letters

c_p	specific heat capacity at constant pressure	$\mathrm{J\,kg^{-1}\,K^{-1}}$
c_s	solid heat capacity	$\mathrm{J\,kg^{-1}\,K^{-1}}$
c_v	specific heat capacity at constant volume	$\mathrm{J\,kg^{-1}\,K^{-1}}$
d	characteristic length	m
d_g	kinetic diameter of a component	m

d_p	mean pore diameter	m
D_t	turbulent diffusion coefficient	$\mathrm{m^2\,s^{-1}}$
D_α^{ij}	binary diffusion coefficient of components i and j in phase α	$\mathrm{m^2\,s^{-1}}$
$D_{\mathrm{pm},\alpha}^{ij}$	effective binary diffusion coefficient of components i and j in phase α in a porous medium	$\mathrm{m^2\,s^{-1}}$
G	Gibbs free energy	J
G_h	ground heat flux	$\mathrm{W\,m^{-2}}$
H	sensible heat flux into the atmosphere	$\mathrm{W\,m^{-2}}$
H_w^i	Henry coefficient for a component i	Pa
h_α	specific enthalpy of a phase	$\mathrm{J\,kg^{-1}}$
k	turbulent kinetic energy	$\mathrm{m^2\,s^{-2}}$
k_B	Boltzmann constant	$\mathrm{J\,K^{-1}}$
k_r	relative permeability	-
Kn	Knudsen number	-
L_eE	latent heat flux	$\mathrm{W\,m^{-2}}$
M^i	molar mass of a component i	$\mathrm{kg\,mol^{-1}}$
$M_{avg,\alpha}$	average molar mass of a phase	$\mathrm{kg\,mol^{-1}}$
m_{VG}	van-Genuchten parameter	-
N	number of components in a system	-
n	number of moles	-
n_{VG}	van-Genuchten parameter	-
p_{sat}^i	saturated vapour pressure of a component i	Pa
p_α	phase pressure	Pa
p_c	capillary pressure	Pa
R	universal gas constant	$\mathrm{J\,mol^{-1}\,K^{-1}}$
R_n	net radiation	$\mathrm{W\,m^{-2}}$
Re	Reynolds number	-
S	saturation	-
S_{eff}	effective saturation	-

$S_{\max}$	diurnal solar irradiance maximum	$\mathrm{W\,m^{-2}}$
S_{irr}	solar irradiance	$\mathrm{W\,m^{-2}}$
S_r	residual saturation	-
T	temperature	K
u_α	specific internal energy of a fluid phase	$\mathrm{J\,kg^{-1}}$
V	volume	$\mathrm{m^3}$
v_α	specific volume of a fluid phase	$\mathrm{m^3\,kg^{-1}}$
X	mass fraction	$\mathrm{kg\,kg^{-1}}$
x	mole fraction	$\mathrm{mol\,mol^{-1}}$
Pr_t	turbulent Prandtl number	-
Sc_t	turbulent Schmidt number	-

Superscripts

i	component index
j	component index

Subscripts

α	phase index, w for wetting phase, n for non-wetting phase (or g for gaseous phase) and s for solid phase
eff	effective quantity
ff	free flow domain
pm	porous medium domain

Abstract

Quantifying evaporation rates and the emission of greenhouse gases from soil plays an important role in predicting changing climate conditions worldwide. Natural and anthropogenic sources of carbon dioxide and methane in soil, e.g. landfills, lead to the migration of these gaseous components in the subsurface and into the atmosphere. The complexity of predicting emissions of these greenhouse gases from the soil into the atmosphere is high, as not only processes in the porous medium influence the transport, but also the ambient atmospheric conditions like wind velocities or solar radiation have a substantial influence on the exchange processes. Additionally, as the soil is partially saturated with water, the problem can only be described properly, when accounting for multiphase flow processes in the porous medium and assessing how drying of the soil influences the transport process.

In order to analyse the governing processes and add to the fundamental understanding of coupled porous-medium free-flow processes, this thesis uses and further develops a numerical model that is able to describe mass, momentum, and energy transfer between a porous medium and an adjacent free flow. The transport in the porous medium is described on the REV scale (*representative elementary volume* scale) with a suitable multiphase, multicomponent model. In the free flow the effects of turbulent flow are captured with Reynolds-averaged Navier-Stokes (RANS) equations and a turbulence model. Coupling conditions between the two domains impose the conservation of mass, momentum, and energy. All equations are implemented in the numerical software DuMu$^{\text{x}}$.

One major focus point of this work is analysing the effects of solar radiation on evaporation and on the transport of greenhouse gases. The effect of solar radiation is included in the coupling conditions between the porous medium and the free flow and analysed under various conditions. A comparison with experimental data shows that the model is able to capture the relevant physical processes.

The second focus point is analysing the multicomponent effects of different gaseous components, namely the main greenhouse gases carbon dioxide and methane. Both components have fluid properties different from air, which makes the choice of analysed components not only relevant in an environmental context but also aims to enhance the understanding of how the fluid properties influence the exchange processes in general. To be able to describe multicomponent effects in diffusive fluxes, the Maxwell-Stefan formulation is implemented and used in both domains. A process analysis of the major influences is conducted, followed by a benchmark study on multicomponent transport in a single-phase set-up, where numerical results are compared to results obtained with the software COMSOL Multiphysics®.

For all focus points different set-ups are compared. As the surface of natural soil often exhibits rough surface structures and uneven topology, set-ups with porous obstacles are included in each analysis. The obstacles change the flow behaviour in the free flow, which in turn influences the transport of the components from the soil into the atmosphere.

The main conclusions drawn from the analysis can be split into the following three areas:

Radiation and evaporation: Analysing evaporation rates from different soil types and under varying wind conditions shows that during both, stage-I and stage-II evaporation, a diurnal cycle of radiation governs the shape of the evaporation curve over time. However, still the soil types and wind conditions influence the onset time of stage-II evaporation. Surface temperatures follow a diurnal cycle as well, with a steep increase in surface temperatures during the transition into stage-II evaporation. The influence of surface obstacles shows that net radiation rates vary depending on obstacle height, which then subsequently influences evaporation rates. Following the process analysis, the numerical results are compared to experimental measurement data, obtained under natural conditions in lysimeters at the Forschungszentrum Jülich. This comparison shows that net radiation is captured well with the implemented model. Evaporation rates are well matched under stage-I evaporation, however under stage-II evaporation, the rates are overestimated in the model. An analysis of different influential parameters and processes shows that with changed soil parameters at the surface, which can be explained by surface treatment of the soil, evaporation rates match much closer with experimental data. This shows that the model is able to capture relevant parameter influences.

Multicomponent transport: Multicomponent transport of carbon dioxide and methane is analysed in a dry and an unsaturated setting under varying wind conditions and for different soil types. It is shown that densities and viscosities have a high influence on the momentum transfer between the free flow and the soil, which in exchange influences the transport rates across the interface. It is analysed how different soil types can control which transport process is dominating. This changes e.g. how wind conditions influence the transport. Multicomponent diffusion is found to have no dominating influence on predicting methane or carbon dioxide fluxes from the soil into the free flow. However, the estimated oxygen transport varies substantially for the model which uses the Maxwell-Stefan formulation in comparison to what a binary Fickian law predicts. The process analysis shows that porous obstacles can lead to an increased momentum transfer from the free flow into the porous medium, which can change the transport of the gaseous components significantly. In order to gain confidence in model results and to asses the capabilities of the model, additionally a benchmark study is presented. Numerical results obtained in this work are compared to results from the software COMSOL Multiphysics®. The benchmark examples cover various scenarios under advective and diffusive dominated regimes. It is shown that both codes show a very good agreement for all benchmark examples.

Multicomponent transport and radiation: The last analysis combines the previously analysed examples on radiation and evaporation with multicomponent transport, examining how a diurnal cycle of radiation influences the transport of methane and carbon dioxide. It is shown that although these components are mainly present in the gas phase, still the temperature changes associated with solar radiation can lead to different transport behaviour. This is especially pronounced for soil with a high permeability and when the water saturation is low. Then temperature changes are higher which results in a higher impact of density and viscosity differences on the flow behaviour.

Zusammenfassung

Die Verdunstungsraten und Emissionen von Treibhausgasen aus Böden zu quantifizieren, ist ein wichtiger Aspekt, um das sich weltweit verändernde Klima besser vorherzusagen. Natürliche und anthropogene Quellen von Kohlenstoffdioxid und Methan im Boden, beispielsweise Deponien, führen zur Migration dieser gasförmigen Komponenten im Untergrund und in die Atmosphäre. Die Prozessbeschreibung zur Vorhersage der Emissionen von Methan oder Kohlenstoffdioxid ist dabei sehr komplex, da nicht nur die Prozesse im Boden einen Einfluss auf den Transportprozess haben, sondern auch die Bedingungen in der umgebenden Atmosphäre. Beispiele hierfür sind die Windgeschwindigkeit oder die Sonneneinstrahlung. Zusätzlich muss berücksichtigt werden, dass der natürliche Boden meist nicht komplett trocken ist, sondern teilweise mit Wasser gesättigt, was zur Folge hat, dass Mehrphasenprozesse im porösen Medium, sowie das Trocknen des Bodens in der Prozessbeschreibung berücksichtigt werden müssen.

Zur Analyse der maßgeblichen Prozesse und zur Erweiterung des grundlegenden Verständnisses von gekoppelten Austauschprozessen zwischen einem porösen Medium und einer freien Strömung wird in dieser Arbeit ein numerisches Modell benutzt und erweitert, welches in der Lage ist, den Austausch von Masse, Impuls und Energie zwischen einem porösen Medium und einer freien Strömung zu beschreiben. Die Transportprozesse im porösen Medium werden dabei auf der REV-Skala (engl. *representative elementary volume*) mit geeigneten Mehrphasen- Mehrkomponentengleichungen modelliert. In der turbulenten freien Strömung werden RANS-Gleichungen (engl. Reynolds-averaged Navier-Stokes) und ein Turbulenzmodell verwendet. Kopplungsbedingungen zwischen den beiden Gebieten garantieren dabei den Erhalt von Masse, Impuls und Energie. Alle Gleichungen sind dabei in der numerischen Software DuMu$^{\text{x}}$ implementiert.

Ein Fokus dieser Arbeit liegt dabei auf der Analyse des Einflusses von Sonneneinstrahlung auf die Evaporation sowie auf den Transport von Treibhausgasen. Der Effekt von Strahlung ist hierzu in den Kopplungsbedingungen zwischen dem porösen Medium und der

freien Strömung implementiert. Der Einfluss der Sonnenstrahlung wird unter verschiedenen Bedingungen analysiert. Im Anschluss werden Modellergebnisse mit experimentellen Daten verglichen und es zeigt sich, dass das Modell die relevanten physikalischen Prozesse abbilden kann.

Der zweite Fokus dieser Arbeit ist die Analyse von mehrkomponenten Effekten von verschiedenen, hauptsächlich gasförmigen, Komponenten. Dabei liegt das Hauptaugenmerk auf den Komponenten Methan und Kohlenstoffdioxid. Beide Komponenten zeigen Fluideigenschaften, die sich von der Standardzusammensetzung von Luft unterscheiden, weswegen die Auswahl dieser Komponenten nicht nur von hoher Umweltrelevanz ist, sondern auch dazu dient, den Einfluss verschiedener Fluideigenschaften auf den Austauschprozess zu analysieren. Um mehrkomponenten Effekte in den diffusiven Flüssen zu beschreiben, wird der Maxwell-Stefan Ansatz in beiden Gebieten implementiert und verwendet. Es wird eine Prozessanalyse durchgeführt, sowie eine Benchmarkstudie über Mehrkomponententransport in Einphasensystemen. Hierbei werden Ergebnisse dieser Arbeit mit Ergebnissen der Software COMSOL Multiphysics® verglichen.

Für alle Fokuspunkte dieser Arbeit werden verschiedene Systeme verglichen. Da der natürliche Untergrund nur selten komplett flach ist, sondern oft eine unregelmäßige, raue Topologie zeigt, werden in jeder Analyse auch Set-ups miteinbezogen, welche poröse Hindernisse enthalten. Diese führen zu sehr großen Änderungen des Geschwindigkeitsfeldes in der freien Strömung, was wiederum den Transport im porösen Medium maßgeblich beeinflusst.

Die Erkenntnisse aus den Analysen der Prozesse können in drei Gebiete unterteilt werden:

Strahlung und Evaporation: Die Analyse der Evaporationsraten von verschiedenen Bodentypen und unter variierenden Windbedingungen zeigt, dass sowohl unter Evaporationsbedingungen, die als Verdunstungsphase-I (stage-I) oder -phase-II (stage-II) gekennzeichnet werden können, die Evaporationsraten einen tagesabhängigen Verlauf zeigen, sodass Strahlung den Verlauf der Kurve stark beeinflusst. Es kann jedoch festgestellt werden, dass das Einsetzen von Verdunstungsphase-II (stage-II) Bedingungen weiterhin auch vom Bodentyp und den Windgeschwindigkeiten abhängt. Die Oberflächentemperatur des Bodens zeigt ebenfalls einen charakteristischen Tagesverlauf, wobei die Temperaturen stark zunehmen, sobald ein Wechsel zur Phase-II Evaporation zu verzeichnen ist. Die Analyse des Einfluss der porösen Hindernisse zeigt, dass sich die Sonneneinstrahlung mit variierender Höhe des Hindernisses verändert, was wiederum einen hohen Einfluss

auf die Evaporationsraten hat. Nach der Prozessanalyse werden die numerisch gewonnen Ergebnisse mit experimentellen Daten verglichen. Diese Daten stammen aus Messungen unter natürlichen Wetterbedingungen in Lysimetern am Forschungszentrum Jülich. Der Vergleich zeigt, dass die Sonneneinstrahlung mit der gewählten Modellapproximation gut abgebildet werden kann. Evaporationsraten unter Phase-I der Evaporationsbedingungen werden ebenfalls gut reproduziert, allerdings werden im Modell Werte unter trockenen Bedingungen überschätzt. Eine Analyse der Einflussparameter und -prozesse zeigt, dass mit angepassten Bodenparametern an der Oberfläche sehr viel bessere Ergebnisse erzielt werden können. Grund für diesen Wechsel der Bodenparameter könnte eine Oberflächenbehandlung des Bodens, z.B. durch Pflügen, sein.

Mehrkomponententransport: Der Transport von Kohlenstoffdioxid und Methan in einem trockenen und einem teilgesättigten Gebiet wird für variierende Windgeschwindigkeiten und Bodenarten untersucht. Diese Analyse zeigt, dass sowohl verschiedene Dichten als auch Viskositäten einen hohen Einfluss auf den Impulsübertrag von der freien Störmung in das poröse Medium haben können. Dies wiederum beeinflusst den Austausch-prozess von Masse zwischen den Gebieten maßgeblich. Es wird gezeigt, dass unterschiedliche Bodenarten beeinflussen können, welcher Transportprozess dominant ist. Dies zeigt sich zum Beispiel beim Einfluss der Windgeschwindigkeiten auf den Transport. Der Einfluss von Mehrkomponentendiffusion auf den Transport von Methan und Kohlenstoffdioxid ist gering, allerdings zeigt sich, dass die vorhergesagten Transportraten von Sauerstoff von der Atmosphäre in den Boden erheblich abweichen können, wenn der Maxwell-Stefan Ansatz verwendet wird im Vergleich zu einer Implementierung des Fickschen Gesetzes, welches nur binäre Diffusion berücksichtigt. Es wird gezeigt, dass poröse Hindernisse einen hohen Einfluss auf den Impulsaustausch zwischen freier Strömung und porösen Medium haben können, was den Transportprozess signifikant beeinflussen kann. Um die Modellresultate abzusichern und die prediktiven Fähigkeiten des Modells abzuschätzen, wird nach der Prozessanalyse eine Benchmarkstudie präsentiert. Ergebnisse dieser Arbeit werden verglichen mit Ergebnissen, die in der Software COMSOL Multiphysics® erzielt werden. Die Benchmarkbeispiele decken dabei verschiedene Szenarien sowohl unter advektiv als auch diffusiv dominierten Systemen ab. Beide Implementierungen zeigen dabei ein sehr gutes Übereinstimmen der Resultate für alle Benchmarkbeispiele.

Mehrkomponententransport und Strahlung: Die letzte Analyse kombiniert die vorherigen Beispiele zur Sonnenstrahlung und Evaporation mit dem Transport mehrerer Komponenten. Dabei wird analysiert, wie ein Tagesverlauf der Sonneneinstrahlung den Transport von Methan und Kohlenstoffdioxid beeinflusst. Es wird gezeigt, dass diese Komponenten ebenfalls von der schwankenden Oberflächentemperatur beeinflusst werden, obwohl sie hauptsächlich in der Gasphase präsent sind. Dies ist besonders in Böden mit hoher Permeabilität und niedriger Wassersättigung zu sehen. In diesem Fall sind die Temperaturunterschiede an einem Tag besonders groß, was zur Folge hat, dass Dichte- und Viskositätsunterschiede ebenfalls einen höheren Einfluss auf das Transportgeschehen haben.

1 Introduction

1.1 Motivation

Evaporation from land surfaces plays a key role in predicting climate change and is a main factor in earth's surface energy balance [Seneviratne et al., 2006]. Increasing concentrations of greenhouse gases in the atmosphere lead to higher temperatures in the soil and the atmosphere and therefore increased evaporation rates. At the same time, soil and agricultural use of the soil are major sources of greenhouse gases themselves [IPCC, 2013, Solomon et al., 2007], leading to complex interactions between evaporation and the migration of greenhouse gases into the atmosphere.

A substantial amount of greenhouse gases emitted by the soil stems from soil respiration due to microbial activity or root respiration [Oertel et al., 2016]. In a series of experimental investigations Russell and Appleyard [1915] found that natural soil often has a higher carbon dioxide content (up to 3.5 %) than the atmosphere, leading to carbon dioxide migration from the soil into the atmosphere. Additionally, anthropogenic sources like landfills contribute to the release of greenhouse gases [IPCC, 2013]. Particularly methane and, due to its oxidation, also carbon dioxide are found in much higher concentrations in the soil in the vicinity of landfills. Gebert et al. [2011] show that for landfill covers methane concentration in soil can have peak concentrations of up to 40 % based on a volumetric ratio.

Evaporation and gas migration at the soil surface are subject to the ambient weather conditions, e.g. solar radiation, humidity, and wind velocities, that influence the transport behaviour of water, air, and greenhouse active gas components in the unsaturated zone and in the atmosphere [e.g. Davarzani et al., 2014, Ganot et al., 2014, Fetzer et al., 2016, Poulsen et al., 2017, Laemmel et al., 2017]. Moreover, soil conditions e.g., soil moisture, soil heterogeneities, and surface treatment of the soil, can have a tremendous influence on evaporation and the release of greenhouse gases [e.g. Reicosky et al., 1997, Poulsen et al.,

2001, Mosthaf et al., 2014, Deepagoda et al., 2016, Fetzer et al., 2017]. Additionally, the gas components itself can interact and influence the transport behaviour, increasing the complexity of the analysis even further [e.g. Molins et al., 2010, Bahlmann et al., 2020].

In order to evaluate the influence of these conditions, several intertwined processes influencing the gas exchange at the interface between soil and atmosphere need to be considered and analysed. An overview of these processes is given in Figure 1.1.

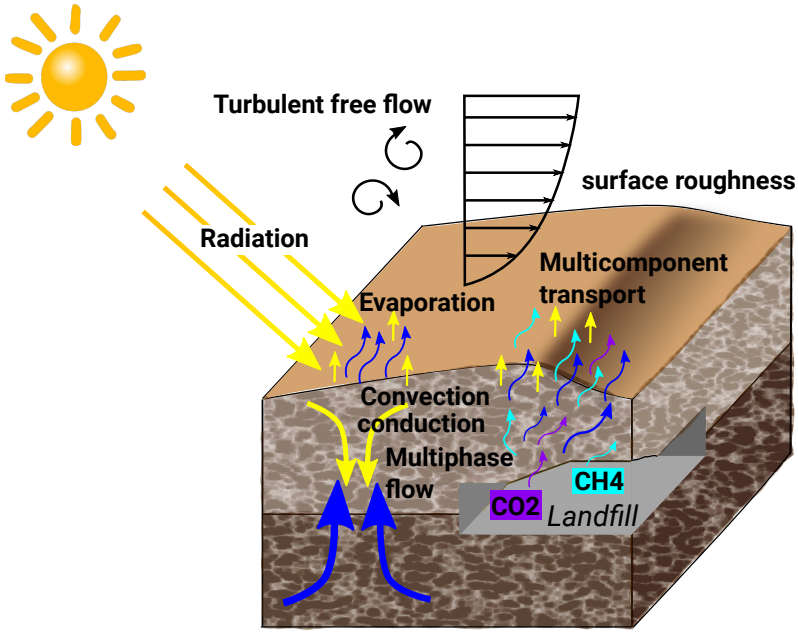

Figure 1.1: Overview of processes influencing evaporation and gas transport in natural systems. Here, a landfill is considered as a source of methane and carbon dioxide, which is then transported in the unsaturated zone and migrates into the atmosphere.

These processes are highly coupled. Therefore, it is common to describe the necessary processes in coupled models, where suitable balance equations are chosen to describe the transport behaviour. Several of these existing coupled models focus on evaporation, analysing the water vapour exchange under different focus points and levels of complexity: Mosthaf et al. [2014] and Davarzani et al. [2014] both analyse evaporation under laminar free-flow conditions, assuming a sharp interface between the porous medium and the free flow. Fetzer et al. [2017] focus on evaporation under turbulent flow conditions, analysing the influence of soil heterogeneities. Haghighi and Or [2015], Gao et al. [2018] analyse evaporation from wavy surfaces, e.g. occurring in tilled soil.

Ahmadi et al. [2020] investigate the transport of methane and carbon dioxide experimentally as well as numerically in a coupled soil-atmosphere model under dry conditions,

applying a one-domain approach using Brinkman's equation in the porous medium as well as in the free flow. Basirat et al. [2015] also apply a one-domain approach and studies a dry porous medium, evaluating carbon dioxide fluxes in sand columns. Both studies use the Maxwell-Stefan formulation to include possible multicomponent effects in the diffusive behaviour. Oldenburg and Unger [2004] investigate carbon dioxide migration in the unsaturated zone coupled to the atmosphere without incorporating evaporation and it's effects on the gas migration and assuming diluted components so that a Fickian diffusive behaviour can be assumed. Furthermore, several studies investigate transport of greenhouse gases without resolving the atmosphere explicitly and accounting for its effects with boundary conditions [e.g. Molins et al., 2008, Deepagoda et al., 2016].

Coupled porous-medium free-flow models can also be applied to other fields of research, e.g. fuel cells [e.g. Baber et al., 2016], food drying [Defraeye and Martynenko, 2018] or filter technology [e.g. Hanspal et al., 2006].

1.2 Objectives and challenges

This work analyses coupled free-flow porous-medium processes under natural conditions including the transport of multiple components and their exchange with the atmosphere (see Figure 1.1). As solar radiation has an immense influence on these processes, one focus point is put into analysing the impact of solar radiation. Solar radiation leads to a tremendous energy input into the system, changing the transport behaviour and phase change of the components immensely. Moreover, the impact of the presence of several gaseous components on the exchange process is analysed in detail. A coupled porous-medium free-flow model is used to analyse the processes, where coupling conditions ensure mass, momentum and energy conservation between the porous medium and free flow.

This work expands the existing coupled free-flow porous-medium model based on the previous work by Mosthaf et al. [2014], Fetzer et al. [2016, 2017] with a concept to include solar radiation. While the previous work focused on analysing two component systems, namely *water* and *air*, this work moreover expands that to include more components, focussing on the greenhouse gases methane and carbon dioxide. The diffusion concept is expanded to a Maxwell-Stefan formulation which is valid for multi-component diffusion. Surface heterogeneities, their influence on evaporation and radiation, and multicompon-

ent transport are analysed, as well as the impact of turbulence under different wind conditions.

1.3 Outline of thesis

In this chapter the topic of multicomponent transport across the free-flow porous-medium interface and its relevance is introduced, giving an overview about existing literature on the topic. In Chapter 2 the necessary fundamental definitions for porous medium flow, the free flow, and the interface between these compartments are presented. Additionally, the relevant processes that are investigated in the following chapters are described. In Chapter 3 an overview of the mathematical model and the necessary balance equations to describe these processes is given. In Chapter 4 the discretization and the numerical model is given, as well as details to the used software framework.

In the next three chapter the numerical analysis and discussion of evaporation and multicomponent transport under the influence of radiation are presented: In Chapter 5 evaporation and a diurnal cycle of solar radiation is analysed and a comparison to experimental data obtained in the research project TERENO SoilCan is presented, Chapter 6 analyses and discusses results for multiphase multicomponent transport and a benchmark study on single-phase multicomponent transport. Chapter 7 analyses multicomponent transport under the influence of radiation. The last chapter summarizes the presented work and gives an outlook on future work.

2 Fundamentals

In this chapter the basic definitions and fundamental relationships that are necessary for the development of the conceptual model and the interpretation of the results are introduced. First, general definitions are given in Section 2.1. Then in Section 2.2 basic definitions for multicomponent interactions are described, in Section 2.3 an overview of the quantities that occur in porous medium flow is given, and in Section 2.4 the definitions necessary to define the free flow in the atmosphere are introduced. Finally, in Section 2.5 the relevant processes, that are analysed in more detail in this work are described in more detail. More extensive definitions for porous medium flow, than given in the following, can be found e.g. in Helmig [1997] or Bear [2018].

2.1 General definitions

2.1.1 Scales

This work is based on continuum scale models, which means that average quantities like density and viscosity are considered as opposed to the molecular scale, where molecule interactions are investigated. In a porous medium, flow and transport of mass, momentum and energy can be considered on different scales. On the *pore-scale*, information about the location and shape of each pore needs to be accounted for, which makes it computationally demanding. To be able to describe larger domains, an averaging over the pore space can be applied, which results in a *representative elementary volume* (REV). On this so-called REV-scale, pore-scale information are transferred to volume-averaged properties like the porosity, which is defined later in Section 2.3.

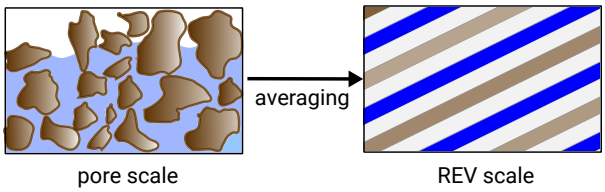

Figure 2.1: Averaging process from the pore scale to the REV scale.

2.1.2 Phases

A phase, α, can consist of several components and is characterized by a physical state. A phase can be liquid, solid or gaseous. On the continuum scale the state is defined by the temperature, pressure, and composition of each state. The different phases are separated by a sharp interface and discontinuous phase properties.

2.1.3 Components

Components, i, are chemical species, which can be present in several phases. Each phase consists of at least one component. Their presence in phases can vary due to pressure and temperature changes during processes like condensation, vaporization, or dissolution.

2.1.4 Basic thermodynamic defintions

Chemical potential

The chemical potential, η_α^i of a component, i, in a phase α is defined as

$$\eta_\alpha^i = \frac{\partial G_\alpha}{\partial \mathrm{n}_\alpha^i}\bigg|_{p,T,n^j} \tag{2.1}$$

with the Gibbs free energy of the phase, G_α and n_α^i as the number of mole of the component, i, in the phase, α.

Local thermodynamic equilibrium

A general assumption of this work is that of a local thermodynamic equilibrium. This means that the system is in local mechanical, thermal and chemical equilibrium. Thermal equilibrium implies that locally all present phases have the same temperature, which means that within one local REV the solid temperature equals the fluid temperature. Mechanical equilibrium describes the condition that pressures on either side of a phase boundary are equal. In porous media pressure jumps, stemming from capillary forces, can still arise [Helmig, 1997], see Section 2.3.3. Chemical equilibrium is given when all components have the same chemical potential and equilibrium relations can be assumed to calculate phase compositions.

2.2 Definitions for multiphase, multicomponent interactions

The following section defines the quantities that are necessary for the description of multicomponent fluid mixtures and gives an overview of the mixing laws that are used to calculate phase composition. More extensive definitions can be found e.g. in Bear [2018].

2.2.1 Mass and mole fractions

The mole fraction, x_α^i, of a component, i, in a phase, α, is the ratio of the number of moles, n_α^i, of a component in a phase, to the number of moles in the phase as a whole, denoted by n_α.

$$x_\alpha^i = \frac{n_\alpha^i}{n_\alpha} = \frac{n_\alpha^i}{\sum_i n_\alpha^i} \,. \tag{2.2}$$

The mass fraction, X_α^i, of a component in a phase can be calculated from the mole fractions with the molar mass of each component, M^i:

$$X_\alpha^i = \frac{x_\alpha^i M^i}{M_{avg,\alpha}} \,. \tag{2.3}$$

$M_{avg,\alpha} = \sum_i x_\alpha^i M^i$ describes the average molar mass of the phase. With these definitions both, mass and mole fractions, are constrained by $\sum_i x_\alpha^i = \sum_i X_\alpha^i = 1$.

2.2.2 Molar phase density and phase density

The density, ϱ_α, and molar density, $\varrho_{\mathrm{m},\alpha}$, of a phase are dependent on temperature, T, pressure, p_α, and the composition of a phase. For gases, often the ideal gas law is used as an equation of state, which relates these quantities together with the universal gas constant R,

$$\varrho_g = \frac{p_g M_{avg,g}}{RT}\,, \quad \varrho_{\mathrm{m},g} = \frac{p_g}{RT}\,. \tag{2.4}$$

Most gases under the moderate pressures and temperature ranges investigated in this work show a behaviour very close to the ideal gas law.

Figure 2.2 shows the gas density dependent on temperature and composition for a gas mixture and various pure gases as used in this work.

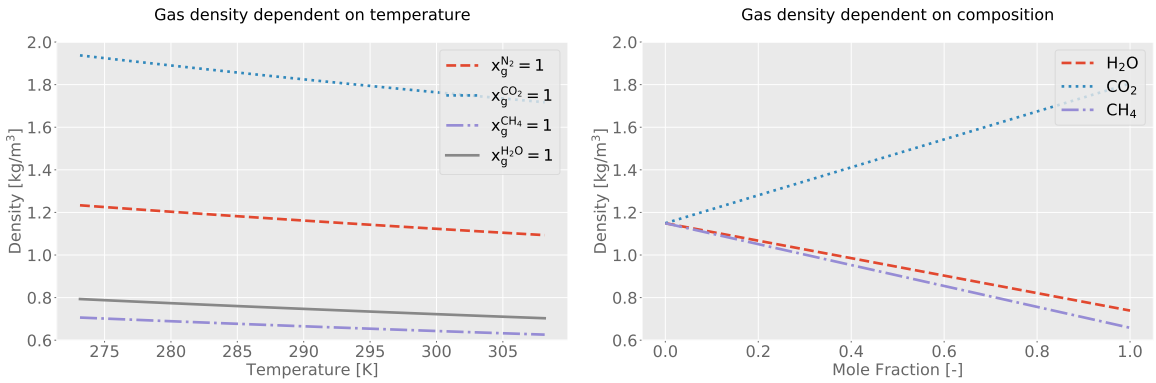

Figure 2.2: *Left:* Gas density of different gases dependent on temperature at a pressure of $1 \cdot 10^5$ Pa. *Right:* Density of a mixture of nitrogen with different gases at a temperature of 293.15 K and pressure of $1 \cdot 10^5$ Pa.

2.2.3 Viscosity

The dynamic viscosity, μ_α, is a measure of a fluid's flow resistance. In multicomponent mixtures viscosities depend on temperature, pressure and composition. While a liquid's dynamic viscosity decreases with temperature, for gases the viscosity increases with increasing temperature.

For the gas phase at low pressures, the dynamic viscosity of a gas mixture, μ_g, can be approximated as a mixture of the pure component viscosities, μ_g^N, for N components with the method of Wilke [Wilke, 1950]:

$$\mu_g = \sum_i^N \frac{x_g^i \mu_g^i}{\sum_j^N x_g^j \frac{(1+(\frac{\mu_g^i}{\mu_g^j})^{1/2}(\frac{M^j}{M^i})^{1/4})^2}{(8(1+\frac{M^i}{M^j}))^{1/2}}} . \tag{2.5}$$

Figure 2.3 shows the dependency of viscosity of various pure gases on temperature. Additionally, the dependency on composition is displayed for a gas mixture of N_2 with various different gases.

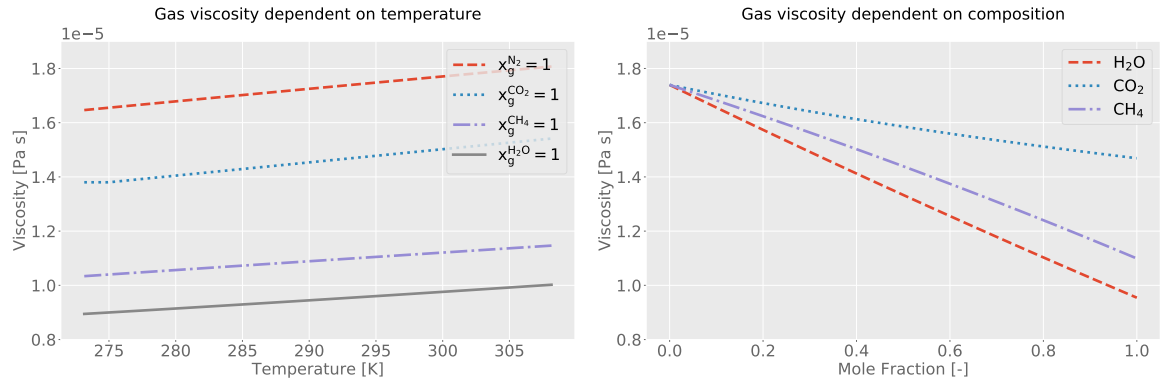

Figure 2.3: *Left:* Gas viscosity of different gases dependent on temperature at a pressure of $1 \cdot 10^5$ Pa. *Right:* Gas viscosity of a mixture of nitrogen with different gases at a temperature of 293.15 K and pressure of $1 \cdot 10^5$ Pa.

In fluid mechanics, often the kinematic viscosity, ν_α, is used. This quantity is defined with $\nu_\alpha = \mu_\alpha / \varrho_\alpha$.

2.2.4 Enthalpy, internal energy and heat capacity of a fluid

If non-isothermal processes are considered, a fluid's internal energy becomes important. The specific internal energy, u_α, of a fluid is defined as the internal energy divided by the fluid's mass and describes the total energy of a fluid phase.

In case the volume of a fluid does not change, the derivative of the internal energy with the temperature is defined as the specific heat capacity at constant volume, c_v.

In contrast, if the fluid is not incompressible, that means that the specific volume of the fluid, v, can change with pressure, additionally the energy for volume change needs to be accounted for. This yields the definition of a fluid's specific enthalpy with:

$$h_\alpha = u_\alpha + p_\alpha v_\alpha = u_\alpha + \frac{p_\alpha}{\varrho_\alpha} \,. \tag{2.6}$$

The specific enthalpy's derivative with the temperature yields the specific heat capacity of a fluid at constant pressure c_p:

$$c_p = \frac{\partial h}{\partial T} \,. \tag{2.7}$$

For an ideal gas the changes in c_p only depend on temperature, which means this relation can be used to calculate fluid's enthalpies.

2.2.5 Thermal conductivity of a fluid

Thermal conductivity, λ_α, relates the conductive energy flux to the temperature gradient in a fluid phase. It depends on temperature and pressure of the phase as well as on composition. Table 2.1 gives an overview of the relationships used to calculate this property for the components as well as for phase compositions.

2.2.6 Phase composition

In multiphase systems a component can be present in several phases, which makes it necessary to find closure relations to determine a phase's composition. When all present phases are in chemical equilibrium, equilibrium relations can be used to calculate phase compositions. These are described in the following.

Raoult's Law and Henry's Law

Raoult's law and Henry's law give a relation for the partial gas pressure of a component in contact with a liquid mixture. Raoult's law can be used for the main component of the liquid and Henry's law for the lower concentrated components. Class [2001] gives a further description for the applicability of each law.

In Raoult's law the saturated vapour pressure, p^i_{sat}, is used to calculate the mole fraction of the component. In non-porous systems, the saturated vapour pressure is solely a function of the temperature of the system. The capillary pressure in a porous medium can change that, and capillary effects need to be taken into account. This is described in 2.3.5.

Raoult's law is given with:

$$x^i_w = \frac{p^i_g}{p^i_{\text{sat}}}\,. \tag{2.8}$$

Henry's law can be used when $x^i_w << 1$. Instead of using the saturated vapour pressure, it uses the so-called Henry coefficient H^i_w, describing the tendency of the component to vaporize into the gas phase:

$$x^i_w = \frac{p^i_g}{H^i_w}\,, \quad H^i_w = H^i_w(T)\,. \tag{2.9}$$

If the liquid phase mostly consists of water, the relationship given by the International Association for the Properties of Water and Steam (IAPWS) for various solutes in liquid water can be used to calculate the Henry coefficient [Fernández-Prini et al., 2003]. Figure 2.4 shows the equilibrium mole fraction of four different components in the liquid phase dependent on temperature, calculated with that relationship.

Dalton's Law

Dalton's law can be applied to ideal mixtures and states that the partial pressure of each component in a gas mixtures sums up to the total gas pressure of the gas phase, with

$$p_g = \sum_i p^i_g\,. \tag{2.10}$$

The ratio of partial pressure to phase pressure can be used to calculate the mole fraction of each component in an ideal gas mixture,

$$x^i_g = \frac{p^i_g}{p_g}\,. \tag{2.11}$$

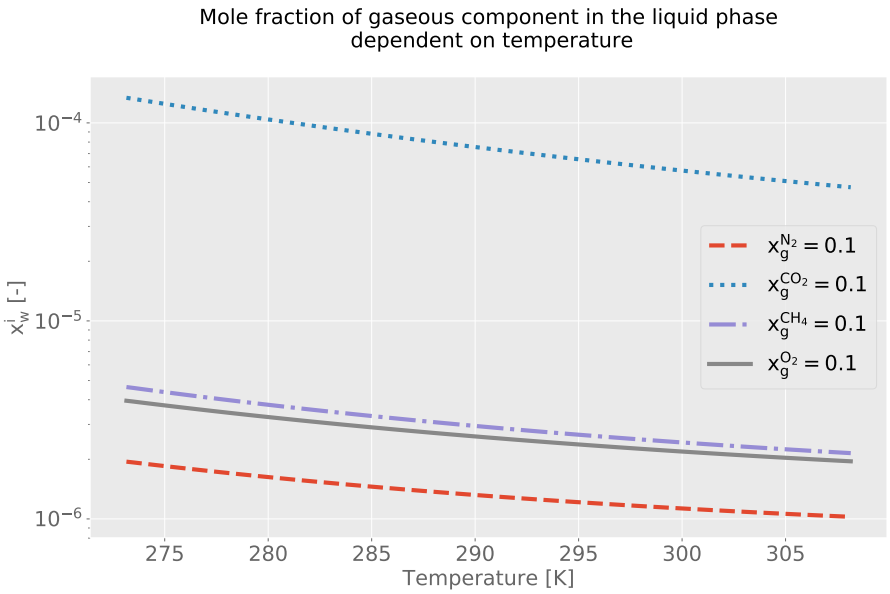

Figure 2.4: Mole fraction of different components in the liquid phase dependent on temperature, calculated with Henry's law. The gas pressure is set to $1 \cdot 10^5$ Pa and the mole fraction of the components in the gas phase to 0.1.

In case the influence of diluted components in the liquid phase can be neglected and the system is in chemical equilibrium, the partial pressure of the component equals the saturated vapour pressure. Then the equilibrium mole fraction can be calculated with:

$$x_g^{i,\mathrm{eq}} = \frac{p_{\mathrm{sat}}^i}{p_g} \,. \tag{2.12}$$

2.2.7 Overview of constitutive relations for fluid parameters

To compute all fluid parameters constitutive relations are needed to calculate their values dependent on temperature, pressure and composition. Table 2.1 gives an overview of these relationships as they are used in this work.

parameter	component/phase		reference
density	component	ϱ_g^i	ideal gas law (Eq. 2.4)
		$\varrho_g^{H_2O}$, $\varrho_w^{H_2O}$	IAPWS [1997]
	phase	ϱ_g	ideal gas law (Eq. 2.4)
		$\varrho_w = \varrho_{w,\mathrm{m}}^{H_2O} \sum M^i x_w^i$	Class et al. [2002]
dynamic viscosity	component	$\mu_g^{H_2O}, \mu_w^{H_2O}$	IAPWS [1997]
		μ_g^i	Chung et al. [1988]
		$\mu_g^{CO_2}$	Fenghour et al. [1998]
	phase	μ_g	Wilke method (Eq. 2.5)
		$\mu_w = \mu_{H_2O}^w$	
specific enthalpy	component	$h_g^{H_2O}$, $h_w^{H_2O}$	IAPWS [1997]
		$h_g^i = c_{p,g}^i T$	Eq. 2.2.4 for ideal gases
		h_g^{CO2}	Span and Wagner [1996]
	phase	$h_g = \sum h_g^i X^i$	Class [2001]
		$h_w = h_w^w$	
specific heat capacity	component	$c_{p,g}^{H_2O}$, $c_{p,w}^{H_2O}$	IAPWS [1997]
		$c_{p,g}^i$	Joback [1984]
	phase	$c_{p,g} = \sum c_{p,g}^i x^i$	
		$c_{p,w} = c_{p,w}^{H_2O}$	
specific internal energy	phase	u_g	Eq 2.6
		u_w	Eq 2.6
thermal conductivity	component	$\lambda_w^{H_2O}$, $\lambda_g^{H_2O}$	IAPWS [1997]
		$\lambda_g^i = \text{const}$	
		$\lambda_g^{N_2}$	Linstrom and Mallard
		$\lambda_g^{O_2}$	Linstrom and Mallard
	phase	$\lambda_g = \sum \lambda_g^i x^i$	
		$\lambda_w = \lambda_w^{H_2O}$	

Table 2.1: Relationships for the calculation of the fluid properties. If the component indices are denoted by i and not with their specific name, the components not specifically addressed use the law given for i.

2.3 Definitions for porous medium flow

As mentioned before, the averaging process to obtain properties of the porous medium on the REV-scale leads to volume-averaged quantities. These averaged porous medium quantities are described in the following section.

A fluid phase in contact with another phase will always form an interface between the phases. Depending on the curvature of the interface, a fluid phase in contact with a solid phase can be distinguished if it is wetting or non-wetting towards the solid. In the following, the system of interest is a porous medium with two different fluid phases present. Separated by their wetting behaviour towards the solid phase, they are denoted by the subscript w for the wetting phase or n for a non-wetting phase. In case of water transport in the unsaturated zone in natural soil, the wetting phase is normally the liquid water phase and the non-wetting phase the gas phase, which is denoted by the subscript g.

2.3.1 Porosity

The porosity, ϕ, is defined as the ratio of volume of voids (or pore volume) to volume of the REV:

$$\phi = \frac{V_{void}}{V_{REV}} \,. \tag{2.13}$$

2.3.2 Saturation

The saturation, S_α of a fluid phase characterizes the ratio of the volume of a phase to the void volume:

$$S_\alpha = \frac{V_\alpha}{V_{void}} \,. \tag{2.14}$$

Due to that definition, the sum of saturation over all present phase is one:

$$\sum_\alpha S_\alpha = 1 \,. \tag{2.15}$$

2.3.3 Capillary pressure

Capillary pressure arises in multiphase flow due to a discontinuity of pressure at the interface between two phases. On the REV-scale it is defined as:

$$p_c = p_n - p_w \,. \tag{2.16}$$

On the pore scale this difference can be calculated by the Young-Laplace equation but on the REV scale other relationships need to be found. One example of such a relationship

is the van-Genuchten relationship [van Genuchten, 1980] that relates the water saturation in a porous medium to the difference between non-wetting and wetting phase pressure on the REV scale:

$$p_c = \frac{1}{\alpha_{VG}}(S_{\text{eff}}^{-1/m_{VG}} - 1)^{1/n_{VG}} \tag{2.17}$$

with $m_{VG} = 1 - 1/n_{VG}$. The van-Genuchten parameters depend on the type of solid and geometry of the solid and are determined by fitting to experimental data. The term S_{eff} describes the effective saturation, defined as:

$$S_{\text{eff}} = \frac{S_w - S_{r,w}}{1 - S_{r,g} - S_{r,w}}\,. \tag{2.18}$$

This effective saturation accounts for the effect, that soil often does not dry completely and additionally never completely saturates with water so a residual saturation, S_r, is always present.

2.3.4 Relative permeability

In multiphase flow in a porous medium, the relative permeability, k_r, accounts for the blockage of flow paths due to the presence of another phase. Relative permeabilities can be described depending on saturations. As in the case of capillary pressure, a commonly used function is the van-Genuchten relationship [Mualem, 1976, van Genuchten, 1980], which defines the relative permeabilities of the wetting phase and the non-wetting phase with:

$$k_{r,w} = \sqrt{S_{\text{eff}}}(1 - (1 - S_{\text{eff}}^{1/m_{VG}})^{m_{VG}})^2\,, \tag{2.19}$$

$$k_{r,n} = (1 - S_{\text{eff}})^{1/2}(1 - S_{\text{eff}}^{1/m_{VG}})^{2m_{VG}}\,. \tag{2.20}$$

2.3.5 Saturated vapour pressure under high capillary pressure

As previously described under assumptions of thermodynamic equilibrium, Raoult's law can be used to compute the partial gas pressure of the main component of the liquid phase with the help of the saturated vapour pressure. Under high capillary pressures, which means high curvature of the interface between gas and liquid phase, that capillary pressure can alter the saturated vapour pressure, which is then not purely a function

of the system's temperature any longer, but capillary effects need to be included. That can be described by Kelvin's equation [Thomson, 1872], here assuming that the main component of the liquid phase is water, denoted by the index H_20.

$$p^i_{\text{sat, Kelvin}} = p^i_{\text{sat}} \exp\left(-\frac{p_c M^{H_20}}{\varrho_w \mathrm{RT}}\right) \tag{2.21}$$

2.4 Definitions for free flow

In this work the transfer of several gaseous components from the porous medium into the free flow and vice versa is investigated. Under natural conditions several flow regimes can occur depending on the flow velocity and fluid mixture. These flow regimes can be distinguished by the Reynolds number. In general the Reynolds number, Re, is defined as:

$$Re_x = \frac{\mathrm{v}_x \mathrm{d}}{\nu_\alpha} \tag{2.22}$$

dependent on a characteristic velocity, v_x, the kinematic viscosity, ν_α, and a characteristic length, d. The Reynolds number denotes a ratio between inertia and viscous forces. High Reynolds numbers mean turbulent flow behaviour that is characterized by the formation of eddies and high fluctuations. Laminar flow in contrast is regular and stream lines are parallel. More information about the different flow conditions can also be found in fluid mechanic textbooks such as White [2016], Schlichting and Gersten [2006].

Two other dimensionless numbers that can be used to characterize a flow regime are the Schmidt number, Sc, and the Prandtl number, Pr. The Schmidt number relates viscous to diffusive forces and is defined as:

$$Sc = \frac{\mu}{\varrho D^{ij}}\,. \tag{2.23}$$

The Prandtl number relates viscous to conductive forces:

$$Pr = \frac{\mu c_p}{\lambda}\,. \tag{2.24}$$

Especially important in the evaluation of transport across the porous-medium free-flow interface is the formation of a boundary layer and its thickness, which is further explained in the following.

2.4.1 Boundary layer characteristics

Boundary layers evolve when fluid flows across an interface. For flow over a flat plate the velocity boundary layer thickness is defined as 99 % of the free stream velocity. Boundary layers also can be defined for temperature and pressure but the thickness of the boundary layer does not necessarily have to be the same for temperature, concentration, and velocity.

Under turbulent flow conditions a further subdivision of the boundary layer into a viscous sublayer and a turbulent part can be made. In the viscous sublayer, viscous forces dominate and transport is mostly diffusion dominated. This makes it crucial to approximate that boundary layer thickness correctly as it is decisive for the transport behaviour from the porous medium into the free flow.

The boundary layer and viscous sublayer thickness can change with the composition and the temperatures of the fluid phases, which is why the influence of multicomponent mixtures and temperature is investigated in this work. Changes in these variables are relevant as the viscosity of the fluid phases is directly influenced by both. If the viscosity changes, the boundary layer thickness and viscous sublayer thickness will also change as the flow behaviour changes. Additionally, density changes can lead to buoyancy effects, which also influence the flow behaviour.

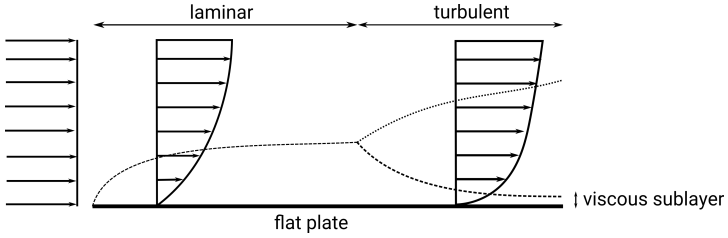

Figure 2.5: Boundary layer evolution over a flat plate from a laminar to a turbulent flow regime.

The boundary layer and viscous sublayer thickness have a tremendous effect on the mass, momentum and energy transfer between a porous medium and a free flow [e.g. Shahraeeni et al., 2012, Fetzer et al., 2016]. If non-flat surfaces are considered, this boundary layer development will be drastically changed as the sublayer can detach and eddies can develop, leading to enhanced mixing. These eddies can also separate areas from the main flow, leading to zones where transport rates are lower and the transported quantities accumulate. For evaporation this is investigated in Haghighi and Or [2015], Gao et al. [2018, 2020], Coltman et al. [2020].

2.5 Relevant processes

When describing evaporation and gas transport of various components under natural conditions, several processes have a high impact on mass transfer from the porous medium into the atmosphere, i.e. surface topology and roughness highly influence evaporation rates, which is evaluated in detail in Fetzer et al. [2016], Fetzer [2018].

This work focuses especially on investigating evaporation under the influence of diurnal cycles of solar radiation and the interaction of evaporation and transport of various gases in the subsurface and across the porous-medium free-flow interface. The dominating processes for this investigation are described in the following.

2.5.1 Transport processes

The presence of multiple components in a mixture can change the behaviour of the whole mixture by changing e.g. viscosities or densities as described above.

A non-reacting, non-absorptive component can be transported by two different mechanisms: One process is the advective transport of the bulk phase. The second process stems from molecule-molecule interactions of the different components and can be described with a suitable diffusion model.

Diffusion due to molecule-molecule interactions is a research topic which has been very intensively discussed in various scientific disciplines. Cussler [2009] give a brief overview of the history of research about that topic. The driving force for diffusion is the difference in chemical potential. However, in most cases, that general driving force is divided into driving forces due to concentration, pressure (pressure diffusion), and external forces (forced diffusion), e.g. gravity or the electric field of an ion. Additionally, it is possible that a temperature gradient induces a diffusive flux, a phenomenon known as the Soret effect [Cussler, 2009]. Not all of these driving forces always contribute substantially to the overall flux and often some contributions can be neglected. Kast and Hohenthanner [2000] give an overview of the different transport mechanisms and their influence under different conditions. In the further investigation pressure diffusion, temperature diffusion, and forced diffusion will not be considered as these effects are very small under conditions that are relevant for evaporation processes at the soil-atmosphere interface. More information

about different models describing diffusion that are investigated in this work can be found in Chapter 3.

In principle, on the micro-scale (pore-scale) and on the macro-scale (REV scale) these diffusion models are derived from the same basis. However, on the REV scale when dealing with flow in a porous medium, diffusion coefficients need to additionally account for properties of the solid, which is accounted for in the so-called effective diffusion coefficient. This is further described in Chapter 3. More information about the upscaling from the micro-scale to REV scale can be found e.g. in [e.g. Helmig, 1997].

In porous media, apart from the advective transport and the transport due to molecular diffusion, additionally a third process can be relevant: Knudsen diffusion, which describes the interactions of a molecule with the walls of the porous medium.

Knudsen diffusion is relevant when pore diameters of the porous medium are small, so that gas molecules collide with the pore walls rather than with other molecules. Studies about the influence of Knudsen diffusion show that for permeabilities lower than 10^{-13} m^2 Knudsen diffusion can start to play a role. Substantial changes in the transport due to Knudsen diffusion are mostly found in lower permeabilities though [e.g. Aronofsky, 1954, Sleep, 1998, Webb and Pruess, 2003, Reinecke and Sleep, 2002].

The Knudsen number Kn helps to distinguish between the different regimes and can help to decide whether to incorporate Knudsen diffusion or not. If the Knudsen number is lower than 0.001, Knudsen diffusion or slip diffusion does not play a role in the transport description any longer [Bear, 2018]. The Knudsen number is defined as:

$$Kn = \frac{\lambda^{kn}}{d_p} \tag{2.25}$$

where λ^{kn} describes the mean free path of the molecules and d_p the mean pore diameter. It can be calculated with

$$\lambda^{kn} = \frac{k_B T}{\sqrt{2} p_g \pi d_g^2} \tag{2.26}$$

and d_g as the kinetic diameter of the gas component and k_B as the Boltzmann constant. For the case of CO_2 ($d_g = 3.30e-10$ m) and a medium sand ($d_p = 1.38e-4$ m [Stingaciu et al., 2010]), atmospheric pressure ($1 \cdot 10^5$ Pa) and a temperature of 298.15 K this means that $K_n = 0.000617 < 0.001$.

Knudsen diffusion will not be considered in this work as it is not a relevant transport process in the unsaturated zone in natural soil.

2.5.2 Evaporation

Evaporation from soil is the process of phase change from liquid water into water vapour and the subsequent transport of that vapour across the porous-medium free-flow interface into the atmosphere. Along with that mass transport, energy is transported. Especially important in that regard is evaporative cooling, which occurs due to the phase change of water from liquid to vapour.

In general, evaporation from bare soil can be characterized in two distinct drying stages [e.g. Lehmann et al., 2008, Yiotis et al., 2007]. The first stage with a nearly constant evaporation rate, often referred to as stage-I evaporation rate or constant-rate period. In this stage, evaporation is mostly governed by the boundary layer thickness and vapour content of the atmosphere, as liquid water is still present at the interface and no limiting factor. Only evaporative cooling and with that a change in the equilibrium vapour content in the porous medium, can lead to a small decrease of evaporation rates. This changes when the drying front moves into lower layers of the soil, and no liquid water is present at the interface any more. Then evaporation is diffusion-limited, that means the diffusive flux across the unsaturated zone limits evaporation rates. This second stage is often called stage-II evaporation or falling-rate period. Figure 2.6 visualizes these stages and the evaporation curve.

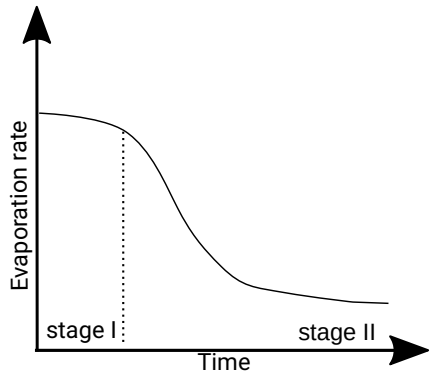

Figure 2.6: Conceptual sketch of the stages of evaporation.

2.5.3 Radiation

Solar radiation has a major effect on evaporation under natural conditions. The energy that is supplied by radiation plays a major role in the phase change of liquid water to water vapour and needs to be accounted for in a surface energy balance under natural conditions. Additionally, a surface energy balance of bare soil needs to account for the energy that is transported into deeper soil layers by conduction and the part of the energy that is transferred back to the atmosphere by conduction or convection. This balance can be written as [e.g. Monteith, 1981, Penman and Keen, 1948, Brutsaert, 1982]

$$R_n = L_e E + H + G_h \,. \tag{2.27}$$

Net radiation, R_n, denotes the balance of incoming and outgoing energy at the earth's surface and therefore balances short- and long-wave radiation at the soil surface. When reaching the earth's surface, the incoming net radiation is split up into latent heat, $L_e E$, that part of the energy that does not lead to temperature change but to a phase change of a substance, a ground heat flux, G_h, that heats up deeper soil layers, and a sensible heat flux into the atmosphere, H, that leads to change in temperature in the atmosphere.

The sun emits short-wave radiation that is already partly reflected in the atmosphere and does not reach the soil surface. Additionally, a part of the incoming radiation is reflected by the soil surface and transferred back into the atmosphere, while the remaining part is adsorbed by the soil. This partitioning depends on the surface's albedo value, which describes the ratio between incoming and reflected radiation. Surface albedo is influenced by various parameters, e.g. soil type, soil moisture, soil structure or soil treatment [e.g. Bowers and Hanks, 1965, Matthias et al., 2000, Davin et al., 2014, Post et al., 2000]. A parametrization depending on soil moisture is described in Section 3.4.3. Additionally, a part of the incoming solar radiation is transferred back into the atmosphere as long-wave radiation. Therefore, net radiation can be described as the sum of long- and short-wave radiation at the soil surface [e.g. Brutsaert, 1982, Novak, 2010]:

$$R_n = S_{\mathrm{irr}}(1 - \alpha_{\mathrm{pm}}) + \sigma_B \epsilon_{\mathrm{pm}}(\epsilon_{\mathrm{ff}} T_{\mathrm{ff}}^4 - T_{\mathrm{pm}}^4) \,, \tag{2.28}$$

where the first term characterizes short-wave radiation with S_{irr} as the solar irradiance and α_{pm} as the soil surface albedo. The second term describes the balance of incoming long wave radiation from the atmosphere and outgoing long-wave radiation from the soil with σ_B as the Stefan-Boltzmann constant, ϵ_{pm} as the soil surface emissivity, ϵ_{ff} as the

atmospheric emissivity, T_{ff} as the atmospheric temperature and T_{pm} as the soil surface temperature. More information about the parametrization used to calculate this balance can be found in Section 3.4.3.

Not only evaporation is influenced by the energy supplied by solar radiation. Under natural conditions thermal gradients can have a high influence on the transport of other gaseous components as well [Rose and Guo, 1995, Nachshon et al., 2008]. Ganot et al. [2014] also show that thermal gradients in the high permeability soil, due to radiation and cooling during the night, can lead to unstable gas density profiles, that enhance the release of carbon dioxide during the night tremendously.

2.5.4 Influence of wind conditions on the transport across the porous-medium free-flow interface

As previously described, it is shown in several numerical and experimental studies that wind flow close to a porous medium can have a high influence on the exchange of gaseous components between the soil and the atmosphere. It is understood that the boundary layer thickness, which depends on wind speed, strongly influences the transport of components [Haghighi et al., 2013, Fetzer et al., 2016]. In the boundary layer (or in the turbulent case the viscous sublayer) transport is governed by diffusion. When the boundary layer is thinner due to higher wind speeds, the diffusive transport across that layer is enhanced due to the higher gradient.

Additionally, several studies show that not only diffusion through the porous medium and the boundary layer influences the transport of gaseous components, but also momentum transfer across the porous-medium free-flow interface can have a significant influence: Poulsen et al. [2003], Nastev et al. [2001] and Massmann and Farrier [1992] demonstrate that changes in atmospheric pressure can influence the exchange of greenhouse gases between a landfill and the atmosphere significantly.

Often, changes in air pressure are associated with so-called turbulence-induced pressure pumping [Maier et al., 2010, Mohr et al., 2016, Laemmel et al., 2017], which enhances the transfer between the soil and the atmosphere at high wind speeds. These high wind speeds lead to pressure fluctuations in the upper soil layer, enhancing the mixing and transport. This is mostly relevant in high permeable soils like gravel or very coarse sand

and is approximated in the models as an additional dispersive mixing [Pourbakhtiar et al., 2017, Poulsen, 2019].

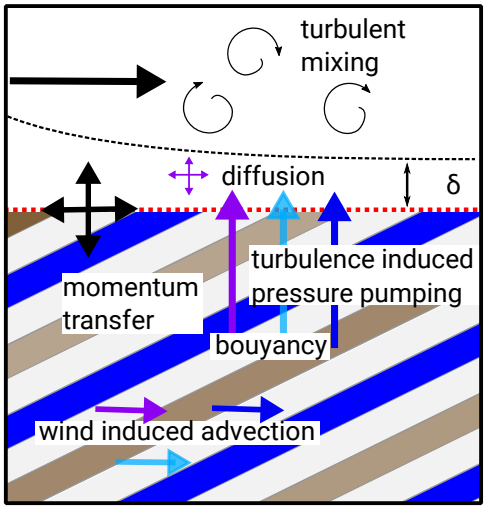

Figure 2.7: Processes influencing the transport across the porous-medium free-flow interface.

Not only turbulence induced fluctuations might influence the transport, but wind can also lead to more stable transfer of momentum into the porous medium, leading to wind induced horizontal advective fluxes [Poulsen, 2019, Bahlmann et al., 2020]. This can lead to additional transport of the gaseous components and result in non-uniform patterns in the concentration distribution. These differences can then influence the diffusive flux across the porous-medium free-flow interface when concentrations are enhanced or decreased by additional advective fluxes.

In multiphase scenarios also indirect effects of wind conditions can play a role. As higher wind velocities lead to higher evaporation rates under stage-I evaporation [e.g. Fetzer et al., 2016], this decreases the temperatures at the interface due to evaporative cooling. This influences diffusion coefficients, but also densities and viscosities and can therefore also influence the advective transport of the components.

Figure 2.7 gives an overview over these processes that can be influenced by wind conditions when investigating gas transport across the porous-medium free-flow interface in a multiphase set-up.

3 Conceptual model for the subdomains and coupling conditions

This chapter describes the mathematical model that is employed to describe the processes relevant for quantifying multicomponent transport across the free-flow porous-medium interface on a continuum scale.

In general there are two approaches possible to describe these coupled processes. One possibility is to use one set of equations that is employed in the whole domain (single domain approach), the other is to describe two domains with their own set of equations and use suitable coupling conditions for the transfer of mass, momentum and energy from one domain into the other (two domain approach). In this work the latter is used to model the necessary processes.

Before the equations for mass, momentum, and energy transport in each domain are presented, two different diffusion concepts are described. First, the commonly used Fick's law, that is valid for binary and dilute multicomponent mixtures and second the Maxwell-Stefan formulation, that is valid for multicomponent diffusion as well as binary diffusion. Both of these models can be used to describe diffusive transport in the subsurface and in the free flow.

Afterwards, this chapter describes the equations for the submodels porous medium and free flow and the coupling conditions for mass, momentum, and energy transfer across the interface of the subdomains. Along with these coupling conditions the parametrization used to describe diurnal variations in solar radiation is presented.

In Section 3.4.2 a short description of the single domain approach is given, as results of the coupled model are compared against the single domain approach in Section 6.2.

3.1 Diffusion models

The following sections describes the two most commonly used diffusion models for multicomponent transport in the subsurface. As described before, their derivation is valid under micro-scale considerations and on the REV scale. On the latter scale, diffusion coefficients in the porous medium need to be adapted to account for effects of the solid phase. This is further described in Section 3.2. The following derivations hold for single- and multiphase flow. For multiphase flow, diffusion is described in each phase. As diffusion in liquid or gaseous phases only differ in their diffusion coefficients, in the following section the indices for the different phases α are omitted.

3.1.1 Fick's law

For binary mixtures and dilute concentrations Fick's first law can be employed [Fick, 1855]. Fick's law describes the motion of species relative to a reference velocity of the mixture. Depending on the reference system, several formulations of Fick's law are available. Which one to employ, depends on the chosen reference system. In a mass reference system the diffusive mass flux $\mathbf{j}^i_{\text{diff}}$ [$\mathrm{kg\,s^{-1}}$] of a component i is described by

$$\mathbf{j}^i_{\text{diff}} = \varrho^i(\mathbf{v}^i - \mathbf{v}) \tag{3.1}$$

with the mass reference velocity $\mathbf{v}$ defined by:

$$\mathbf{v} = \sum_{i=1}^{n} X^i \mathbf{v}^i \tag{3.2}$$

with $\mathbf{v}^i$ as the species velocities.

More information about the reference systems, it's benefits and transformation from one reference system into another can be found e.g. in Taylor and Krishna [1993].

For a mass reference system Fick's law is given by [e.g. Bird et al., 2006]:

$$\mathbf{j}^i_{\text{diff}} = -D^{ij}\varrho\nabla X^i\,. \tag{3.3}$$

This form of Fick's law is valid for binary mixtures with the index j indicating the second species. It relates the mass fraction gradient to the diffusive mass flux by employing a

binary diffusion coefficient. Extended version of Fick's law for multicomponent mixtures are also available, which use diffusion coefficients dependent on the composition of the mixture, yet in this work Fick's law is only employed in its binary version, implying that when more than two components are present, they are diluted enough to only interact with the main component.

To transfer the diffusive mass flux $\mathbf{j}_{\text{diff}}$ [$\text{kg}\,\text{s}^{-1}$] into the molar diffusive flux to be used in the mole balance given above, the mass flux has to be divided by the molar mass of the component M^i:

$$\mathbf{J}^i_{\text{diff}} = \mathbf{j}^i_{\text{diff}} \frac{1}{M^i} \tag{3.4}$$

Other forms of Fick's law employ the mole fraction gradient as the driving force, a form which is valid when diffusion is regarded relative to a molar average velocity.

3.1.2 Maxwell-Stefan formulation

For more than two components and in mixtures, where the assumption that concentration are low enough so that the diluted components only interact with the main component does not hold, the Maxwell-Stefan formulation can be necessary. In such mixtures it is possible to observe diffusion opposite to the gradient of mole fractions or when no concentration gradient is present. These diffusion phenomena result from coupling effects between the different molecules in a gas-mixture [Krishna and Wesselingh, 1997]. They were found in an experiment with a ternary gas mixture by Duncan and Toor [1962]. Krishna and Wesselingh [1997] showed that the Maxwell-Stefan formulation is able to capture these phenomena adequately. The Maxwell-Stefan formulation has a thorough basis in nonequilibrium thermodynamics and can be derived from entropy production (see e.g. Kjelstrup et al. [2010] for a derivation). For N components it is commonly given as:

$$\frac{x^i \nabla_T \eta^i}{RT} = -\sum_{j=1, j\neq i}^{N} \frac{x^i x^j}{D^{ij}} \left(\mathbf{v}^i - \mathbf{v}^j\right) \tag{3.5}$$

with $\mathbf{v}^i$ and $\mathbf{v}^j$ as the velocity of the species i and j and η^i as the chemical potential of the species.

In terms of diffusive mass fluxes $\mathbf{j}^i_{\text{diff}}$ (with $\varrho^i = X^i\varrho$) it can be formulated as:

$$\frac{x^i\nabla_T\eta^i}{RT} = -\sum_{j=1,j\neq i}^{N}\frac{x^ix^j}{D^{ij}}\left(\frac{\mathbf{j}^i_{\text{diff}}}{\varrho^i}-\frac{\mathbf{j}^j_{\text{diff}}}{\varrho^j}\right) = -\sum_{j=1,j\neq i}^{N}\frac{x^ix^j}{D^{ij}\varrho}\left(\frac{\mathbf{j}^i_{\text{diff}}}{X^i}-\frac{\mathbf{j}^j_{\text{diff}}}{X^j}\right) \tag{3.6}$$

The diffusion coefficients are symmetric $D^{ij} = D^{ji}$ due to the Onsager symmetry, which simplifies the system [Kjelstrup et al., 2010].

Additionally, the fact that not all diffusive fluxes are independent can be used. For the molar diffusive fluxes a derivation can be found in Krishna and Wesselingh [1997]. Here, we employ mass fluxes and mass averaged velocities, $\mathbf{v}$, so that $\sum_i^N \mathbf{j}^i_{\text{diff}} = 0$ according to equation 3.2. This means that the N-th flux can be expressed as $\mathbf{j}^N_{\text{diff}} = -\sum_j^{N-1}\mathbf{j}^j_{\text{diff}}$. Inserting this and rearranging leads to:

$$\frac{x^i\nabla_T\eta^i}{RT}\varrho = -\left(\sum_{j=1,j\neq i}^{N}\frac{x^ix^j}{D^{ij}X^i}\right)\mathbf{j}^i_{\text{diff}} + \sum_{j=1,j\neq i}^{N-1}\left(\frac{x^ix^j}{D^{ij}X^j}\mathbf{j}^j_{\text{diff}}\right) - \frac{x^ix^N}{D^{iN}X^N}\mathbf{j}^i_{\text{diff}} - \sum_{j=1,j\neq i}^{N-1}\left(\frac{x^ix^N}{D^{iN}X^N}\mathbf{j}^j_{\text{diff}}\right). \tag{3.7}$$

Sorting this for the component fluxes $\mathbf{j}^i$ and $\mathbf{j}^j$ and introducing the coefficients B^{ii} and B^{ij} this can be written as:

$$\frac{x^i\nabla_T\eta^i}{RT}\varrho = -B^{ii}\mathbf{j}^i_{\text{diff}} - \sum_{j=1,j\neq i}^{N-1}B^{ij}\mathbf{j}^j_{\text{diff}}\,. \tag{3.8}$$

with

$$B^{\text{ii}} = \frac{x^ix^N}{D^{iN}X^N} + \sum_{j=1,j\neq i}^{N}\frac{x^jx^i}{D^{ij}X^i} = \frac{x^iM_{avg}}{D^{iN}M^n} + \sum_{j=1,j\neq i}^{N}\frac{x^jM_{avg}}{D^{ij}M^i}\,, \tag{3.9}$$

and

$$B^{\text{ij}} = -x^i\left(\frac{x^j}{D^{ij}X^j}-\frac{x^N}{D^{iN}X^N}\right) = -x^i\left(\frac{M_{avg}}{D^{ij}M^j}-\frac{M_{avg}}{D^{iN}M^N}\right). \tag{3.10}$$

Note that this is a slightly different version of the entries as defined in Taylor and Krishna [1993] as here the matrix is derived for the mass reference systems not the molar reference system.

As the influence of pressure and temperature on diffusion is neglected in this work, the

driving force of diffusion can be further simplified to [Taylor and Krishna, 1993]:

$$\frac{x^i \nabla_T \eta^i}{RT} \varrho = \sum_{j=1}^{N-1} \Gamma^{ij} \nabla x^j \,. \tag{3.11}$$

where Γ^{ij} deals with the non-idealities of the fluid [Taylor and Krishna, 1993, Krishna and Wesselingh, 1997] and is defined as:

$$\Gamma^{ij} = \delta_{ij} + x^i \frac{\partial \ln \gamma^i}{\partial x^j} \,. \tag{3.12}$$

δ_{ij} is the Kronecker delta which is 1 for $i = j$ and 0 for $i \neq j$. γ is the activity coefficient of a component in a mixture.

With that definition Equation 3.8 can be written into a convenient matrix form of the Maxwell-Stefan formulation

$$\mathbf{j}_{\text{diff}} = -\varrho \mathbf{B}^{-1} \mathbf{\Gamma} \nabla \mathbf{x} \,, \tag{3.13}$$

where $\mathbf{j}_{\text{diff}}$ (for $i = 1, ..., N-1$) denotes a vector of all but one diffusive fluxes and the matrix $\mathbf{B}$ has the dimension $(N-1) \times (N-1)$. In this formulation $\mathbf{\Gamma}$ is called matrix of thermodynamic factors. For ideal mixtures $\mathbf{\Gamma} = \mathbf{I}$, the identity matrix.

It can be shown that for two components denoted by superscripts a and b the Maxwell-Stefan formulation reduces to Fick's law as the matrices become scalars and

$$B^{aa} = \frac{x^a x^b}{D^{ab} X^b} + \frac{x^b x^a}{D^{ab} X^a} = \frac{x^a x^b X^a + x^a x^b X^b}{D^{ab} X^a X^b} \tag{3.14}$$

with the definition of $X^a = x^a \frac{M^a}{M_{avg}}$ and assuming $\Gamma^{ab} = 1$ and set into the above equation this leads to:

$$\mathbf{j}^a_{\text{diff}} = -\varrho D^{ab} \frac{M^a M^b}{M^2_{avg}} (\nabla \mathrm{x}^a) \tag{3.15}$$

with $\nabla X^a = \frac{M^a M^b}{M^2_{avg}} (\nabla \mathrm{x}^a)$ this leads then to the form of Fick's law for a mass reference velocity given above. A more detailed derivation can be found in appendix A or similarly in Whitaker [2009].

As previously mentioned, there is also the possibility to formulate Fick's law for multicomponent diffusion. Here, also the Maxwell-Stefan relationship can be used to calculate the multicomponent diffusion coefficients. In an ideal system, where the thermodynamic factor is unity, the Maxwell-Stefan diffusion coefficients and the Fick's law

coefficients are related by the relationship: $\mathbf{D} = \mathbf{B}^{-1}$, where $\mathbf{D}$ denotes the matrix of Fick's multicomponent diffusion coefficients. This matrix of Fickian diffusion coefficients is not a diagonal matrix only, which is an extension of the most common form of the Fickian approach.

In order to evaluate if multicomponent diffusion has a relevant influence on the transport for a given mixture, the computation of multicomponent diffusion coefficients can be helpful, as demonstrated in the following example. When all binary diffusion coefficients are very similar, multicomponent effects often can be neglected, which can be explained when calculating the multicomponent diffusion coefficients for Fick's law. Assuming a three component mixture with the mole fractions $\mathrm{x}^a = 0.1$, $\mathrm{x}^b = 0.4$ and $\mathrm{x}^c = 0.5$ and the Maxwell-Stefan diffusion coefficients $D^{ab} = 2.1 \cdot 10^{-5}\ \mathrm{m^2\,s^{-1}}$, $D^{ac} = 2.0 \cdot 10^{-5}\ \mathrm{m^2\,s^{-1}}$, and $D^{bc} = 1.9 \cdot 10^{-5}\ \mathrm{m^2\,s^{-1}}$, the calculation of the Fick's diffusivities then results in:

$$\mathbf{B}^{-1} = \begin{pmatrix} 49047 & 238 \\ 2005 & 52130 \end{pmatrix}^{-1} \mathrm{m^2\,s^{-1}} = \mathbf{D} = \begin{pmatrix} 2,03 \cdot 10^{-5} & -7.8 \cdot 10^{-7} \\ -9.3 \cdot 10^{-8} & 1.92 \cdot 10^{-5} \end{pmatrix} \mathrm{m^2\,s^{-1}} \tag{3.16}$$

Here, for simplicity, it is assumed that the molar masses for all components are the same, so that the molar masses vanish from the computation of the entries of $\mathbf{B}$. The diffusive fluxes can then be calculated with $\mathbf{j}_{\mathrm{diff}} = \varrho \mathbf{D} \nabla \mathbf{X}$. It can be seen, that the off-diagonal entries are two magnitudes smaller than the diagonal entries, which results in a diffusive flux that is dominated by the diagonal entries and the own concentration gradient of each component, resulting in diffusive fluxes that are very similar to what is predicted when using the common form of the Fickian diffusion, where only diagonal entries of the diffusion coefficient matrix are considered. This example also shows that when the concentration gradient of one of the components is very small compared to the gradients of the other components, it is possible that then the off-diagonal elements have a greater impact on the diffusive flux of that component. More examples on how to calculate multicomponent diffusion coefficients can be found in Taylor and Krishna [1993].

However, this example also demonstrates the drawback of employing a multicomponent version of Fick's law as it requires a calculation of the multicomponent diffusion coefficients for each mixture depending on concentrations. This leads to nonlinear functions of the diffusion coefficients depending on concentration, temperature, and pressure.

Therefore, using the Maxwell-Stefan relationship directly to calculate diffusive fluxes in multicomponent mixtures avoids that complication.

3.1.3 Binary diffusion coefficients

In this work, Fick's law and the Maxwell-Stefan formulation are analysed. Both diffusion formulations require binary diffusion coefficients even for the computation of multicomponent diffusive fluxes. Therefore, these coefficients need to be properly defined for each binary pair.

Binary diffusion coefficients can be derived from molecular simulations [e.g. Liu et al., 2012, Krishna and van Baten, 2005], they can be estimated from experiments or a mixture of both. In general, Fick's diffusivities and Maxwell-Stefan diffusivities are not the same but differ by the thermodynamic factor [Taylor and Krishna, 1993, Krishna and Wesselingh, 1997] so that $D^{ij}_{\text{Fick's law}} = \Gamma^{ij} D^{ij}_{\text{MS}}$. For gaseous solutions under moderate pressures or for ideal mixtures the thermodynamic factor is one ($\Gamma^{ij} = 1$). Then the binary diffusion coefficients for both diffusion formulations are the same. For non-ideal liquid mixtures, the thermodynamic factor depends strongly on the mixture and therefore the Fick's diffusivities show a strong dependence on composition as well [Taylor and Krishna, 1993, Krishna and Wesselingh, 1997].

Table 3.1 gives an overview of the relationships used to calculate the different binary diffusion coefficients in this work. For gases the dependency on pressure and temperature of the binary diffusion coefficients is accounted for with the used method. This method gives good results for binary diffusion coefficients of gases under low pressure [Poling, 2000] which is the intended pressure range for this work. Under these pressure conditions, the binary diffusion coefficients do not depend on composition, so these methods predict the coefficients only dependent on pressure and temperature [Poling, 2000]. In liquids the diffusion coefficients are calculated with the assumption of infinite dilution. In the scope of this work mostly gases that are not highly soluble in water, at least under moderate pressure and temperature conditions, are investigated, justifying that assumption. Table 3.2 shows the values of the gaseous diffusion coefficients as they are calculated with the above mentioned relationship for a given pressure of $1 \cdot 10^5$ Pa and 283.15 K.

parameter		reference
gaseous diffusion coefficient	$D_g^{i,j}$	Fuller et al. [1966]
liquid diffusion coefficient	$D_w^{H_2O,N_2}$	Ferrell and Himmelblau [1967]
	$D_w^{H_2O,O_2}$	Ferrell and Himmelblau [1967]
	$D_w^{H_2O,CH_4}$	Witherspoon and Saraf [1965]
	$D_w^{H_2O,CO_2}$	Vivian and King [1964], Poling [2000]
	$D_w^{i,j} = \text{const}$	

Table 3.1: Relationships for the calculation of the binary diffusion coefficients. If the component indices are denoted by i or j and not with their specific name, all components use the same law.

parameter	value $[\mathrm{m^2\,s^{-1}}]$
$D_g^{N_2,H_2O}$	$2.38534 \cdot 10^{-5}$
$D_g^{N_2,O_2}$	$1.91971 \cdot 10^{-5}$
$D_g^{N_2,CO_2}$	$1.51164 \cdot 10^{-5}$
$D_g^{N_2,CH_4}$	$2.00535 \cdot 10^{-5}$
$D_g^{O_2,H_2O}$	$2.43156 \cdot 10^{-5}$
$D_g^{O_2,CO_2}$	$1.50046 \cdot 10^{-5}$
$D_g^{O_2,CH_4}$	$2.02429 \cdot 10^{-5}$
$D_g^{CO_2,H_2O}$	$1.92866 \cdot 10^{-5}$
$D_g^{CO_2,CH_4}$	$1.64144 \cdot 10^{-5}$
$D_g^{CH_4,H_2O}$	$2.42723 \cdot 10^{-5}$

Table 3.2: Binary diffusion coefficients for the gas phase as used in the following evaluation at $1 \cdot 10^5$ Pa and 283.15 K.

3.2 Porous medium

In this section all relevant processes, balance equations, and constitutive relationships for non-isothermal compositional transport in the porous medium are described. They are based on the assumption that there is a local thermodynamic equilibrium, that the solid phase does not move or deform, that flow conditions are creeping and inertia forces are negligible [Helmig, 1997].

3.2.1 Mass and momentum balance

A general mass balance for multiphase flow in porous media is given by:

$$\frac{\partial}{\partial t}\left[\sum_{\alpha}\phi S_{\alpha}\varrho_{\alpha}\right]+\nabla\cdot\left[\sum_{\alpha}\varrho_{\alpha}\mathbf{v}_{\alpha}\right]=\sum_{\alpha}q_{\alpha}\,. \tag{3.17}$$

The flow velocity of each phase is denoted by $\mathbf{v}_{\alpha}$.

When considering flow of a component in a porous medium, this equation needs to be expanded to also include diffusion (denoted by the diffusive flux of a component i in each phase $J^{i}_{\mathrm{diff},\alpha}$ [$\mathrm{mol\,s^{-1}}$]) and the presence of that component in all phases. Therefore, a balance equation for a component i in several phases α in a porous matrix is given by:

$$\frac{\partial}{\partial t}\left[\sum_{\alpha}\phi S_{\alpha}\varrho_{\alpha}X^{i}_{\alpha}\right]+\nabla\cdot\left[\sum_{\alpha}\varrho_{\alpha}X^{i}_{\alpha}\mathbf{v}_{\alpha}+\mathbf{j}^{i}_{\mathrm{diff},\alpha}\right]=\sum_{\alpha}q^{i}_{\alpha}\,. \tag{3.18}$$

Here, the balance equation is given as a mass balance, with the mass fraction X^{i}_{α} of a component i in a phase α. This mass balance can easily be changed to a mole balance by dividing with the species molar mass M^{i}. As the molar mass of a component does not change, the formulations of a mass or a mole balance are equivalent. As stated before, the saturations in such a system add up to one as well as the mole fractions of the components in each phase. For a two-phase system that leads to the constraints $\mathrm{S}_{w}+\mathrm{S}_{n}=1$, $\sum_{i}^{N}\mathrm{X}^{i}_{w}=1$ and $\sum_{i}^{N}\mathrm{X}^{i}_{n}=1$.

Dalton's Law and Raoult's Law are used to calculate phase compositions under chemical equilibrium assumptions. Additionally, a relationship for saturation and capillary pressure needs to be used, see Chapter 2 for that.

Darcy's Law

Darcy's Law, formulated based on experiments by Henry Darcy in 1856 [Darcy, 1856], relates the fluid's pressure gradient to the flow velocity in a porous medium. For multiphase flow in porous media it is necessary to use an extended version of that law, given as: (see e.g. Helmig [1997])

$$\mathbf{v}_{\alpha}=-\frac{k_{r,\alpha}\mathbf{K}}{\mu_{\alpha}}(\nabla p_{\alpha}-\varrho_{\alpha}\mathbf{g})\,. \tag{3.19}$$

This extended version of Darcy's Law includes an intrinsic permeability $\mathbf{K}$, that is a property of the soil, independent of the fluids in the porous medium. In isotropic soil, this permeability is a scalar value. The relative permeability, $k_{r,\alpha}$, is a scaling factor accounting for the presence of multiple phases, which depends on saturation. For single-phase flow it equals one. The parametrization used to as closure relations is described in Section 2.3.4.

Effective diffusive fluxes

As previously mentioned, on the REV-scale in a porous medium the diffusive fluxes need to be adapted to account for the presence of the solid phase as well as the presence of other fluid phases. Therefore, an effective diffusion coefficient has to be formulated.

$D^{ij}_{\mathrm{pm},\alpha}$ is the effective binary diffusion coefficient of the two components i and j in the phase α with i as a diluted species and j as the main species of the phase α.

In this work, the relationship by Millington and Quirk [1961] is used:

$$D^{ij}_{\mathrm{pm},\alpha} = D^{ij}_{\alpha} \tau \phi S_{\alpha} \,, \tag{3.20}$$

which includes the porosity, ϕ, the saturation, S_α, the tortuosity, τ, of the porous medium, and the binary diffusion coefficient, D^{ij}_{α}. The tortuosity in this approach is calculated with:

$$\tau = \phi^{\frac{1}{3}} S_{\alpha}^{\frac{7}{3}} \,. \tag{3.21}$$

The tortuous pathway that a component has to take in a porous medium is shown in Figure 3.1.

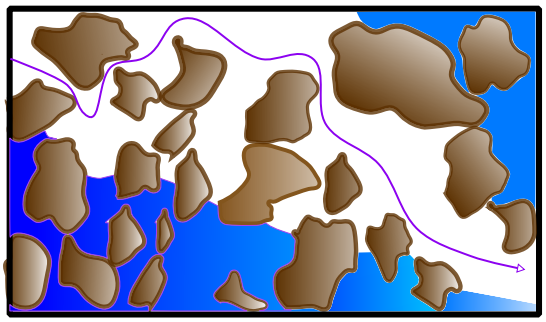

Figure 3.1: Pathway of a component in a porous medium, where the presence of another phase and the solid phase hinder the component to diffuse freely.

The effective diffusion coefficient is then a macro-scale quantity and dependent on the fluid and solid phase. This empirical relationship leads to lower diffusive fluxes in the porous medium as compared to diffusion in the free flow.

3.2.2 Energy balance

Under the assumption of local thermal equilibrium all phases within one local REV have the same temperature. Therefore, only one energy balance is needed, which includes contribution from the fluid phases as well as the solid phase.

$$\frac{\partial}{\partial t}\left[\sum_{\alpha}(\phi\varrho_{\alpha}u_{\alpha}S_{\alpha}) + (1-\phi)\,\varrho_{\mathrm{s}}c_{\mathrm{s}}T_{pm}\right] + \nabla\cdot\left[\sum_{\alpha}(\varrho_{\alpha}h_{\alpha}\mathbf{v}_{\alpha}) - \lambda_{\mathrm{eff}}\nabla T_{pm}\right] = q^{h}\,. \quad (3.22)$$

In the storage term, the specific internal energy of the fluids u [$\mathrm{J\,kg^{-1}}$] is evaluated. Due to the compressibility of the fluids, in the flux terms additionally the volume change of the phases needs to be accounted for. This can be done with the enthalpy $h = u + p/\varrho$. The contribution of the solid phase to energy storage is included with the heat capacity of the solid phase, c_s and the solid density, ϱ_s.

The thermal conductivity λ_{eff} is again an effective property, for which closure relations need to be found. In this work the relationship by Somerton et al. [1974] is used:

$$\lambda_{\mathrm{eff}} = \lambda_s^{1-\phi}\lambda_n^{\phi} + \sqrt{S_w}(\lambda_s^{1-\phi}\lambda_w^{\phi} - \lambda_s^{1-\phi}\lambda_n^{\phi})\,. \quad (3.23)$$

3.3 Free flow

To model the behaviour of wind flowing over a porous medium the Navier-Stokes equations are used, with the assumption to model single-phase flow. Therefore, all equations refer to gas flow, denoted by the index g.

3.3.1 Mass balance

A general mass balance of any fluid is given by the continuity equation:

$$\frac{\partial \varrho_g}{\partial t} + \nabla \cdot (\varrho_g \mathbf{v}_g) = 0 \tag{3.24}$$

For the transport of components in the gas phase this can be expanded to:

$$\frac{\partial (\varrho_g X_g^i)}{\partial t} + \nabla \cdot (\varrho_g X_g^i \mathbf{v}_g) + \nabla \cdot \mathbf{j}_{\text{diff},g}^i = 0 \tag{3.25}$$

Diffusive fluxes can again either be described by Fick's Law or the Maxwell-Stefan formulation.

3.3.2 Momentum balance

To balance the momentum the sum of the forces acting on the fluid volume are set equal to the change in momentum across each face of the control volume, together with the change in momentum within the control volume. The forces acting on the fluid volume are the forces acting on the surface and the gravitational force. This leads to:

$$\frac{\partial \varrho_g \mathbf{v}_g}{\partial t} + \nabla \cdot (\varrho_g \mathbf{v}_g \mathbf{v}_g^T) - \nabla \cdot (\boldsymbol{\tau}_g) + \nabla \cdot (p_g \mathbf{I}) - \varrho_g \mathbf{g} = 0\,. \tag{3.26}$$

For a Newtonian fluid with the assumption of the validity of Stokes' hypothesis the shear stress tensor $\boldsymbol{\tau}_g$ can be denoted by: $\boldsymbol{\tau}_g = \mu_g(\nabla \mathbf{v}_g + \nabla \mathbf{v}_g^T) - (\frac{2}{3}\mu_g \nabla \cdot \mathbf{v}_g)\mathbf{I}$. Under the assumption that the flow is nearly incompressible, the second term in the shear stress tensor is very small which simplifies the term to $\boldsymbol{\tau}_g = \mu_g(\nabla \mathbf{v}_g + \nabla \mathbf{v}_g^T)$.

For low Reynolds numbers the inertia terms can be neglected. When gravity effects do not play a role the equation then reduces to the Stokes equation:

$$\frac{\partial \varrho_g \mathbf{v}_g}{\partial t} - \nabla \cdot (\mu_g(\nabla \mathbf{v}_g + \nabla \mathbf{v}_g^T)) + \nabla \cdot (p_g \mathbf{I}) = 0\,. \tag{3.27}$$

3.3.3 Energy balance

The energy balance in the free flow only needs to account for heat transfer in the gas phase, which leads to:

$$\frac{\partial(\varrho_g u_g)}{\partial t} + \nabla\cdot(\varrho_g h_g \mathbf{v}_g) + \sum_\kappa \nabla\cdot(h_g^\kappa \mathbf{j}_{\mathrm{diff},g}^\kappa) - \nabla\cdot(\lambda_g \nabla T_g) = 0\,. \tag{3.28}$$

3.3.4 Reynolds-averaged Navier-Stokes

In order to properly capture turbulent free-flow behaviour it would be necessary to resolve the free-flow domain in very high spatial and temporal resolution, as turbulent behaviour leads to pressure and velocity fluctuations. To overcome that problem, which would be computationally challenging, it is possible to apply the so-called Reynolds averaging, which decomposes the fluctuating terms into a time averaged value (e.g. velocity $\bar{\mathbf{v}}_g$) and a fluctuating term (e.g. $\mathbf{v}_g'$). Due to that averaging, the fluctuating terms average to zero, however, the product of fluctuating terms does not. This introduces an additional term in the momentum balance. Under the assumption of stationary turbulence, this then leads to the following Reynolds-averaged Navier-Stokes (RANS) equations. Due to better readability, the bar, indicating mean values of the averaged quantities (e.g. $\bar{\mathbf{v}_g}, \bar{x_g^i}, \bar{T}, \bar{p_g}$) will be omitted in the following equations.

$$\frac{\partial \varrho_g \mathbf{v}_g}{\partial t} + \nabla\cdot(\varrho_g \mathbf{v}_g \mathbf{v}_g^T) + \nabla\cdot(\varrho_g \mathbf{v}_g' \mathbf{v}_g'^T) - \nabla\cdot(\boldsymbol{\tau}_g) + \nabla\cdot(p_g \mathbf{I}) - \varrho_g \mathbf{g} = 0\,. \tag{3.29}$$

It can be seen that the averaging introduces a new term $\varrho \mathbf{v}_g' \mathbf{v}_g'^T$, which is also called the Reynolds stress tensor. Although it stems from averaging the inertia term, a simplification by Boussinesq [1877] relates the Reynolds stress to viscous stresses. Then the RANS equations can be expressed as:

$$\frac{\partial \varrho_g \mathbf{v}_g}{\partial t} + \varrho_g \nabla\cdot(\mathbf{v}_g \mathbf{v}_g^T) - \nabla\cdot(\boldsymbol{\tau}_g + \boldsymbol{\tau}_{g,t}) + \nabla\cdot(p_g \mathbf{I}) - \varrho_g \mathbf{g} = 0\,, \tag{3.30}$$

where the Reynolds stress is now denoted by $\boldsymbol{\tau}_{g,t} = \mu_{g,t}(\nabla \mathbf{v}_g + \nabla \mathbf{v}_g^T) - (\frac{2}{3}\varrho_g k \mathbf{I})$.

Another common form is to express the shear stresses with the help of the strain rate tensor, $\mathbf{S}$, which is defined as $\mathbf{S} = \frac{1}{2}(\nabla \mathbf{v}_g + \nabla \mathbf{v}_g^T)$.

Now, the turbulent behaviour can be expressed by the eddy viscosity, μ_t, and the turbulent kinetic energy, k under the assumption of isotropic turbulent flow behaviour. For that, closure relations need to be employed, described in the next section.

A detailed derivation of the RANS equations can be found in fluidmechanic textbooks such as Wilcox [2006], White [2016], Versteeg and Malalasekera [2007]. As compressibility effects on turbulence are not important for shock-free and non-hypersonic turbulent flow, an averaging of the densities is not necessary.

The balance equation for the transport of a component i after Reynold's averaging is denoted by:

$$\frac{\partial \left(\varrho_g X_g^i\right)}{\partial t} + \nabla \cdot \left(\varrho_g \mathbf{v}_g X_g^i - \mathbf{j}_{\mathrm{diff},t}^i\right) - q^i = 0\,. \tag{3.31}$$

Here, the diffusion term, $\mathbf{j}_{\mathrm{diff},t}^i$, additionally accounts for the diffusive flux due to turbulent fluctuations by using an effective diffusion coefficient defined as $D_{\mathrm{eff},t}^{ij} = D_g^{ij} + D_t$. This introduces the eddy diffusivity D_t which is related to eddy viscosity by the turbulent Schmidt number, Sc_t, with:

$$D_\mathrm{t} = \frac{\mu_\mathrm{t}}{Sc_\mathrm{t}\varrho_g}\,. \tag{3.32}$$

The turbulent Schmidt number can be chosen as a model parameter.

Additionally, the energy balance is adapted to:

$$\frac{\partial(\varrho_g u_g)}{\partial t} + \nabla\cdot(\varrho_g h_g \mathbf{v}_g) + \sum_i \nabla\cdot(h_g^i \mathbf{j}_{\mathrm{diff},t}^i) - \nabla\cdot((\lambda_g + \lambda_t))\nabla T) = 0\,. \tag{3.33}$$

The eddy thermal conductivity can be derived from the eddy viscosity with the turbulent Prandtl number, Pr_t, and the specific heat capacity, $c_{p,g}$:

$$\lambda_t = \frac{\mu_\mathrm{t} c_{p,g}}{Pr_\mathrm{t}}\,. \tag{3.34}$$

Turbulence model

There are many models available to close the system of unknowns: zero-equation models, that do not require to solve another partial differential equation (PDE), one-equation models that require another PDE, and two-equation models that additionally add two

more equations as constraints to solve. In Wilcox [2006] a thorough overview over different turbulence models is given.

In the following work, the so-called $k-\omega$ model is employed, which can be used for both the region near a wall (or a porous medium) and the turbulent flow [Wilcox, 2008]. This model adds to additional PDEs to the system of equations, a balance for turbulent kinetic energy and one for the turbulent frequency. The region near the wall is described by grid specific boundary conditions which incorporate the near-wall effects. Drawbacks of the model can be found in setting the right boundary conditions for a free stream. As in this work the region close to the interface is of the most interest, this does not affect the model results.

The balance equation for the turbulent kinetic energy k can be written as:

$$\frac{\partial(k\varrho_g)}{\partial t} + \nabla\cdot(\mathbf{v}_g\varrho_g k) - \nabla\cdot\left(\left(\mu_g + \sigma_k\varrho_g\frac{k}{\omega}\right)\nabla k\right) - 2\mu_\mathrm{t}\mathbf{S}\cdot\mathbf{S} + \beta_k\varrho_g k\omega = 0\,. \tag{3.35}$$

The strain rate tensor $\mathbf{S}$ is defined as $\mathbf{S} = \frac{1}{2}(\nabla\mathbf{v}_g + \nabla\mathbf{v}_g^T)$. The turbulence frequency ω can be calculated with:

$$\frac{\partial(\omega\varrho_g)}{\partial t}+\nabla\cdot(\mathbf{v}_g\varrho_g\omega)-\nabla\cdot\left(\left(\mu_g+\sigma_\omega\varrho_g\frac{k}{\omega}\right)\nabla\omega\right)-\alpha_\omega\frac{\omega}{k}2\mu_\mathrm{t}\mathbf{S}\cdot\mathbf{S}+\beta_\omega\varrho_g\omega^2-\frac{\sigma_d\varrho_g}{\omega}\nabla k\cdot\nabla\omega = 0\,. \tag{3.36}$$

The eddy viscosity is then calculated with:

$$\mu_\mathrm{t} = \frac{k}{\tilde{\omega}}\varrho_g \tag{3.37}$$

The following closure coefficients and relations taken from Wilcox [2008] are used:

$$\begin{aligned}
&\alpha_\omega = 0.52 \\
&\sigma_k = 0.6 \\
&\sigma_\omega = 0.5 \\
&\beta_k = 0.09 \\
&\beta_\omega = 0.0708
\end{aligned}
\qquad
\begin{aligned}
&\tilde{\omega} = \max\{\omega, 0.875\sqrt{\tfrac{2\mathbf{S}\cdot\mathbf{S}}{\beta_k}}\} \\
&\sigma_d = \begin{cases} 0, & \text{if } \nabla k\cdot\nabla\omega \le 0 \\ 0.125, & \text{if } \nabla k\cdot\nabla\omega > 0 \end{cases}
\end{aligned}$$

Table 3.3: Closure relations for the $k-\omega$ turbulence model

3.4 Interface

The following section describes first the conditions for coupling mass, momentum, and energy between a porous medium and a free flow as they are applied in this thesis. Then, as an alternative to that, the single-domain approach is shorty introduced. In the end the closure relations for the radiation concept that is applied in this thesis is presented in more detail.

3.4.1 Coupling conditions

In the two domain approach applied in this work, two separate sets of equations describe the transport of mass, momentum and energy in the free flow and in the porous medium. Suitable coupling conditions are needed to ensure the transfer of these quantities from one domain into the other. These interface conditions are based on the assumption of local thermodynamic equilibrium as described in Mosthaf et al. [2011] and Fetzer et al. [2016]. More details about the derivation are given in these publications.

As we assume a sharp interface between the two domains that does not store mass, momentum, or energy, all mass leaving one domain has to instantaneously appear in the other. Continuity of fluxes can be written as:

$$[(\varrho_g \mathbf{v}_g) \cdot \mathbf{n}]^{\mathrm{ff}} = -[(\varrho_g \mathbf{v}_g + \varrho_w \mathbf{v}_w) \cdot \mathbf{n}]^{\mathrm{pm}} \tag{3.38}$$

with $\mathbf{n}$ as the interface normal vector (always pointing out of the respective domain).

For the tangential momentum the coupling condition is set according to the Beavers-Joseph-Saffman condition [Beavers and Joseph, 1967, Saffman, 1971, Jones, 1973] with α_{BJ} as the Beavers-Joseph coefficient and $\mathbf{t}_i$ as a tangential vector:

$$\left[\left(-\mathbf{v}_g - \frac{\sqrt{(\mathbf{K}\mathbf{t}_i)\cdot\mathbf{t}_i}}{\alpha_{BJ}}(\nabla\mathbf{v}_g + \nabla\mathbf{v}_g^T)\mathbf{n}\right)\cdot\mathbf{t}_i\right]^{\mathrm{ff}} = 0\,, \quad i \in \{1, .., d-1\}\,. \tag{3.39}$$

This condition leads to a non-zero slip velocity at the interface between porous medium and free flow. The influence of the Beavers-Joseph condition on evaporation rates has been numerically investigated by Fetzer et al. [2016] and experimentally in Terzis et al. [e.g. 2019]. Although the validity of this condition is questionable for flow not parallel

to the interface [e.g. Eggenweiler and Rybak, 2020], this condition will still be applied throughout this work, due to a lack of suitable conditions for multiphase flow. Additionally, the investigated flow is mostly parallel to the interface and non-parallel flow should only occur under low Reynolds numbers in the viscous sublayer, therefore justifying this choice of boundary condition.

For the normal part of the momentum balance a continuity of normal stresses is applied and the coupling conditions is:

$$[((\varrho_g \mathbf{v}_g \mathbf{v}_g^T - (\boldsymbol{\tau}_g + \boldsymbol{\tau}_{g,t}) + p_g \mathbf{I})\mathbf{n})]^{\mathrm{ff}} = [(p_g \mathbf{I})\mathbf{n}]^{\mathrm{pm}} . \tag{3.40}$$

This coupling conditions might lead to a jump in gas pressure at the interface, which then might lead to minor differences in the mole fractions at the interface as well [Mosthaf et al., 2011].

For a component, i, continuity of fluxes can be written as:

$$[(\varrho_g X_g^i \mathbf{v}_g + \mathbf{j}_{\mathrm{diff},t}) \cdot \mathbf{n}]^{\mathrm{ff}} = -\left[\left(\sum_\alpha (\varrho_\alpha X_\alpha^i \mathbf{v}_\alpha + \mathbf{j}_{\mathrm{diff},\alpha}^i)\right) \cdot \mathbf{n}\right]^{\mathrm{pm}} . \tag{3.41}$$

For the energy coupling the flux condition is:

$$\left[\left(\varrho_g h_g \mathbf{v}_g + \sum_i h_g^i \mathbf{j}_{\mathrm{diff},g}^i + \lambda_g \nabla T\right) \cdot \mathbf{n}\right]^{\mathrm{ff}} = R_n - \left[\left(\sum_\alpha (\varrho_\alpha h_\alpha \mathbf{v}_\alpha + \sum_i h_\alpha^i \mathbf{j}_{\mathrm{diff},\alpha}^i) - \lambda_{\mathrm{pm}} \nabla T\right) \cdot \mathbf{n}\right]^{\mathrm{pm}} . \tag{3.42}$$

R_n denotes the net radiation. The balance equation for radiation can be found in Section 2.5.3 and constitutive relationships to compute net radiation can be found in Section 3.4.3.

3.4.2 Single domain approach

An alternative approach to the previously described two domain approach is the single domain approach. Opposed to using two sets of equations in both domains and suitable

coupling conditions, in the one domain approach one equation that is valid in both regions is used throughout the whole domain.

For porous-medium free-flow systems the one domain approach uses the so-called Brinkman equation [Brinkman, 1949], essentially a superposition of Darcy's law and the Stokes equation for single-phase flow:

$$\frac{1}{\phi}\frac{\partial(\varrho\mathbf{v})}{\partial t} + \frac{1}{\phi^2}\nabla\cdot(\varrho\mathbf{v}\mathbf{v}^T) = -\nabla p + \nabla\cdot(\mu_{\text{eff}}\nabla\mathbf{v}) - \frac{\mu_g}{K}\mathbf{v} + \varrho\mathbf{g} \tag{3.43}$$

The soil properties like porosity and permeability are discontinuous throughout the domain, being set to one in the free-flow region and to a value lower than 1 in the porous-medium region. Mass conservation is automatically satisfied at the interface between porous medium and free flow and no coupling conditions need to be defined.

The equation employs a so-called effective viscosity μ_{eff}, which accounts for the momentum exchange in the transition zone between porous medium and free flow. Which formulation of that viscosity to choose, is not straightforward [e.g. Martys et al., 1994, Rosenzweig and Shavit, 2007]. In the benchmark comparison in Section 6.2, the approach by Ochoa-Tapia and Whitaker [1997] is used, which defines the effective viscosity as $\mu_{\text{eff}} = \frac{\mu}{\phi}$.

The Brinkman equation is applied to investigating single-phase flow in coupled porous-medium free-flow systems, e.g. by Ahmadi et al. [2020], Basirat et al. [2015], Shavit et al. [2004]. Drawbacks of the method are an extension to two-phase flow and especially the inclusion of additional terms in the coupling conditions such as radiation, which can be easily incorporated in the two domain approach as described before.

3.4.3 Constitutive relations for the radiation model

To describe a daily cycle of solar radiation closure relations need to be used that characterize e.g. solar irradiance, surface emissivity, and albedo values. In Section 2.5.3 a relationship for long- and short-wave radiation at the soil surface is shown (Equation 2.5.3). This relationship can be used in the coupling conditions of the energy equations to account for radiation at the interface. Short-wave radiation follows a daily cycle, depending on the location on earth and also on local surface structures. A diurnal cycle

for solar radiation can be described by [Yamanaka et al., 1998]

$$S = S_{\max} \cos\left(2\pi \frac{t+12}{24}\right) \tag{3.44}$$

for $6 < t < 18$ h and $S = 0$ during $18 > t < 6$. This variation matches a solar irradiance variation for areas where it is 12 hours night and 12 hours day. It is valid for flat surfaces where the sun is at a 90° angle at midday. To also account for non-flat surfaces, this equation is adapted to include the angle of the surface, γ, to:

$$S = S_{\max} \cos\left(2\pi \frac{t+12}{24} + \gamma\right) . \tag{3.45}$$

For an angle of 0° this function reaches its maximum at midday and for an upwards angle of 45° at 9 in the morning. The maximum value of radiation $S_{\max}$ [W m^{-2}] can be taken from measurement data, depending on the location and cloud cover of the evaluated data set.

Additionally, when considering non-flat surfaces, shadows need to be accounted for. In 2-d settings this can be easily included by calculating the shadow length with geometric considerations. Figure 3.2 shows the calculation of the shadow length, sl: $\text{sl} = \tan(90° - \alpha) \cdot h$.

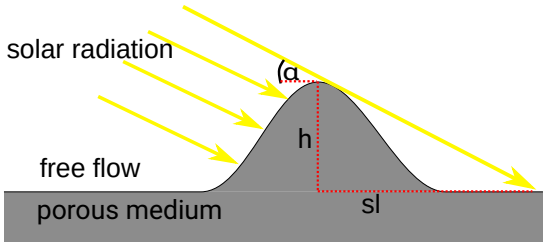

Figure 3.2: Calculation of shadow length in a 2-d set-up.

Long-wave radiation at the earth's surface consists of two different terms, the outgoing long-wave radiation by the soil surface and the incoming long-wave radiation by the atmosphere. Both terms can be evaluated by the Stefan-Botzmann Law, with the emissivity ϵ as a proportionality factor which is lower than 1 for all materials that cannot be seen as black bodies. The atmospheric emissivity is highly influenced by the presence of water vapour and other greenhouse gases like CO_2 in the atmosphere. Water vapour plays a crucial role as it is adsorbing long-wave radiation over a broad band of wavelengths and

is abundant in the atmosphere. Several parametrizations are available to calculate the atmospheric emissivity. Broadly used is the method by Brutsaert [1982], which expresses atmospheric emissivity as a function of the atmospheric temperature T_α and the vapour pressure p_g^w (in hPa) near the surface with

$$\epsilon_{\mathrm{ff}} = 1.24 \left(\frac{p_g^w}{T_{\mathrm{ff}}} \right)^{\frac{1}{7}} . \tag{3.46}$$

This relationship is based on clear sky conditions (no cloud cover) and derived by integrating the atmospheric profile with the assumption of an exponential profile of atmospheric temperature and humidity. It was found to be a suitable approximation in various studies [e.g. Silva et al., 2019, Herrero and Polo, 2012]. Including the vapour pressure has the benefit that increasing vapour content in the air changes the long-wave radiation directly. Higher emissivities lead to higher incoming long-wave radiation and therefore increased net radiation.

Soil surface emissivity and soil surface albedo are both quantities that depend very much on soil type and saturations. Parametrized relationships can be derived from measurements.

In Novak [2010] parameters for the surface emissivity as well as surface albedo are given depending on the soil moisture content. Soil moisture content is defined as:

$$\theta = S_w \phi \tag{3.47}$$

These relationships are also used in Mosthaf [2014], where radiation is included as a source term in the upper soil layer. Soil surface emissivity depending on soil moisture is then [Novak, 2010, Jassal et al., 2003]:

$$\begin{aligned} \epsilon_{\mathrm{pm}} &= 0.93 + 0.1333\theta, \text{ for } \theta < 0.3 \\ \epsilon_{\mathrm{pm}} &= 0.97, \text{ for } \theta \geq 0.3 \end{aligned} \tag{3.48}$$

And the soil albedo is given with [Novak, 2010, 1981]:

$$\begin{aligned} \alpha_{\mathrm{pm}} &= 0.17, \text{ for } \theta < 0.04 \\ \alpha_{\mathrm{pm}} &= 0.1846 - 0.3654\theta, \text{ for } 0.04 \leq \theta \leq 0.3 \\ \alpha_{\mathrm{pm}} &= 0.075, \text{ for } \theta > 0.3 \end{aligned} \tag{3.49}$$

Figure 3.3 shows these parameters dependent on soil moisture. While surface albedo decreases with water saturation, which reduces net radiation, the surface emissivity increases. Higher surface emissivity leads to an increase of long-wave radiation.

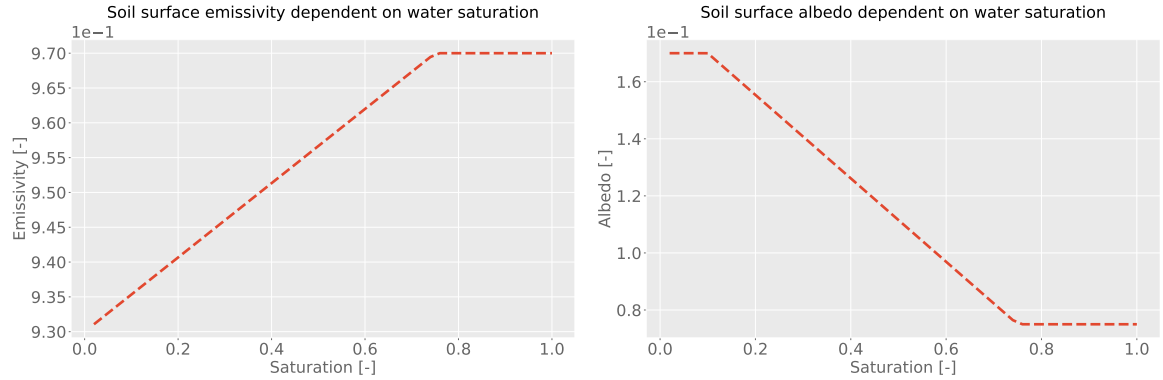

Figure 3.3: Soil surface emissivity (*left*) and soil surface albedo (*right*) dependent on water saturation.

When dealing with non-flat surfaces another aspect in the radiation balance is radiation transferred from surface to surface, when one surface intercepts the radiation of another. This can be accounted for by calculating view factors for each surface [e.g. Modest, 2013, Saneinejad et al., 2012]. This plays e.g. a prominent role in calculating city climate in narrow streets. As the soil undulations investigated in this work are rather small and more widespread, most of the radiation transfer is between soil and atmosphere. Therefore, the influence of radiation from surface to surface will be neglected in the following evaluation.

4 Numerical model

4.1 Numerical discretization in space

4.1.1 Porous medium and free flow

The subdomains (porous medium and free flow) use different spatial discretization schemes with varying locations of the primary variables. The two different schemes will be briefly described in the following.

In the porous medium a finite volume cell-centered two point flux approximation scheme is used, which means that the primary variables are located at the cell centre.

In the free-flow domain a finite volume staggered grid scheme (also known as marker-and-cell scheme [Harlow and Welch, 1965]) is employed. More information about that can be found e.g. in Versteeg and Malalasekera [2007]. For that discretization, the scalar quantities are located at the cell centres and control volumes are built around that. The velocities and their control volumes are shifted by a half cell so that they are located at the faces of the control volumes of the scalar quantities. This avoids unphysical pressure oscillations [Versteeg and Malalasekera, 2007]. A sketch of the mentioned positions and control volumes can be seen in Figure 4.1.

Discretizing the non-linear inertia term in the Navier-Stokes equation poses the question of how to approximate the transported velocity. For flat surfaces the first order upwind method is chosen. When non-flat surfaces are regarded, a total variation diminishing (TVD) method is used, that allows second order accuracy. In the following results, the formulation by Hou et al. [2011] is employed. More information about this discretization scheme and the upwind methods can be found in Versteeg and Malalasekera [2007], Vescovini [2018], Coltman et al. [2020].

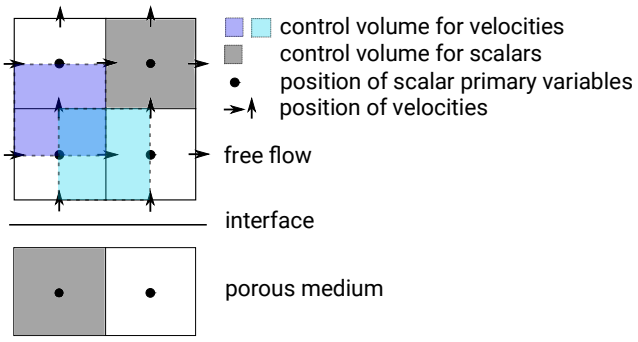

Figure 4.1: Locations of the primary variables in the porous medium and the free flow with respective control volumes.

4.1.2 Coupling at the interface

As can be seen in Figure 4.1 there is no degree of freedom for the primary variables at the interface except for the normal component of the free-flow velocity. Imposing the coupling conditions therefore is not straightforward. One possibility to implement this coupling conditions would be an interface solver where additional degrees of freedom at the interface are introduced. However, this method also has drawbacks in the numerical stability, which is why in this work a simpler coupling method is implemented. Instead of introducing an additional local system of equations at the interface, it is assumed that the gradients in mass fraction and temperature, which are needed for the continuity of mass and energy, can be built across the interface, which implies that the gradient on each side of the interface has the same slope. In order to obtain accurate results, a fine discretization of the grid at the interface is necessary for this method. More information about advantages and drawbacks of these methods and a comparison of the different coupling schemes can be found in Fetzer [2018].

4.2 Numerical discretization in time

For the temporal discretization a fully implicit Euler scheme is used. The system is solved monolithically by Newtons method and with the direct linear solver UMFPACK [Davis, 2004]. Time step sizes are variable and based on the convergence of the previous time step.

4.3 Implementation

All presented equations are modelled in the open-source simulator DuMu^{x} [Flemisch et al., 2011, Koch et al., 2020] which is based on the numerical toolbox Dune [Bastian et al., 2008a,b]. For all set-ups involving non-planar surfaces dune-subgrid [Gräser and Sander, 2009] is used to partition the set-up into two conforming domains.

5 Results and discussion I - Evaporation under the influence of solar radiation [1]

In this chapter, numerical results of the influence of radiation on evaporation rates are analysed and compared to experimental results. First, a process analysis evaluates the influence of a diurnal cycle of solar radiation on different soil types under various wind conditions. Afterwards, it is analysed how much the temperature dependency of the fluid parameters density, viscosity and diffusion coefficients influences evaporation rates. Then the influence of non-planar surfaces, e.g. occurring in tilled soils, on evaporation and radiation is discussed. In the end, a comparison with measurement data, obtained from outdoor lysimeters in the research project TERENO SoilCan, is presented and shows that the model is able to capture the relevant influences.

5.1 Process analysis

The first section presents a process analysis of the influence of a diurnal cycle of radiation on evaporation rates.

Figure 5.1 shows the set-up for the following examples. It consists of a flat porous medium with a wind tunnel above where wind flows from left to right and supplies fresh air. The temperature in the free flow is adapted to follow a diurnal cycle of atmospheric temperature. The sun rises at 6 in the morning on the left side of the domain and sets on the right in the evening. The set-up including surface undulations presented in Section

[1] The following section is also presented in parts in: Heck, K., Coltman, E., Schneider, J., & Helmig, R. (2020). Influence of radiation on evaporation rates: A numerical analysis. Water Resources Research, 56, e2020WR027332. https://doi.org/10.1029/2020WR027332 [Heck et al., 2020] .

5.1.3 uses the same initial and boundary conditions as presented for the flat set-up in Figure 5.1 and includes 5 hills across the interface. Dimensions and information about the discretization for that set-up can be found in the appendix in Figure B.1.

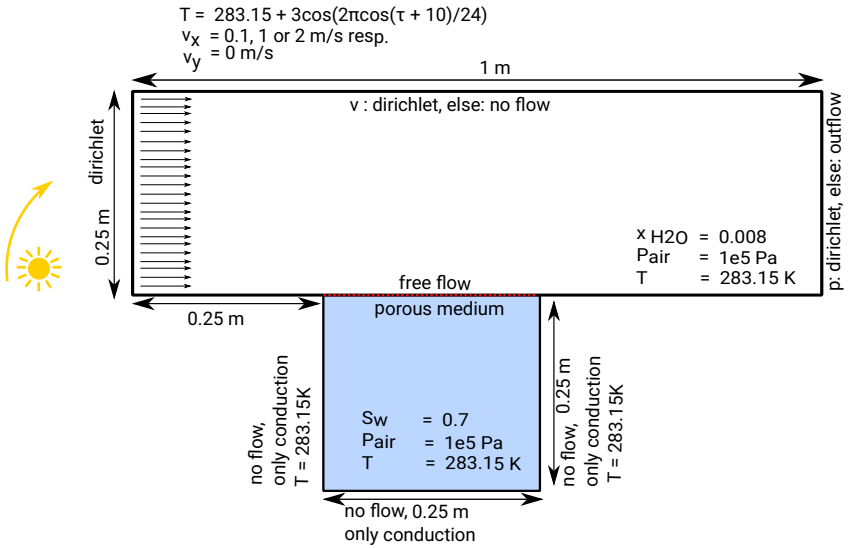

Figure 5.1: Initial and boundary conditions for analysing the influence of radiation on evaporation rates, with τ as the time in hours. The problem is discretized with 100 cells in the horizontal and 60 cells in the vertical direction with a refinement towards the interface.

5.1.1 Influence of wind velocities and soil type

Figure 5.2 shows the evaporation rates for two soil types under three different wind conditions. The compared soil types are a silty soil, which has a rather low permeability and a quartz sand, that drains more quickly with a higher permeability and porosity. The comparison of these soil types make it possible to analyse the influence of radiation on evaporation rates under different conditions and stages of drying.

The necessary parameters to characterize the soil types are given in Table 5.1.

Comparing the two soil types and different wind velocities in Figure 5.2, it can be observed that, although the shape of the evaporation flux is governed by the diurnal cycle of the sun, the amount of evaporation is governed by the availability of water.

For the sandy soil type during the first three days, peak evaporation rates for each wind velocity nearly reach the same daily maximum, as the capillary flow is high enough to satisfy the evaporative demand and evaporation rates are in stage-I evaporation, governed

parameter	sandy soil	silty soil	
n	8	1.32	[-]
α	6.37e-4	4.28e-5	[1/Pa]
Snr	0.01	0.029	[-]
Swr	0.005	0.057	[-]
ϕ	0.41	0.35	[-]
K	2.65e-10	1.08e-12	[m^2]
c_s	790	790	[J/(kg K)]
λ_s	2.8	2.8	[W/(m K)]
ϱ_s	2600	2600	[kg/m^3]

Table 5.1: Material properties of two soil types

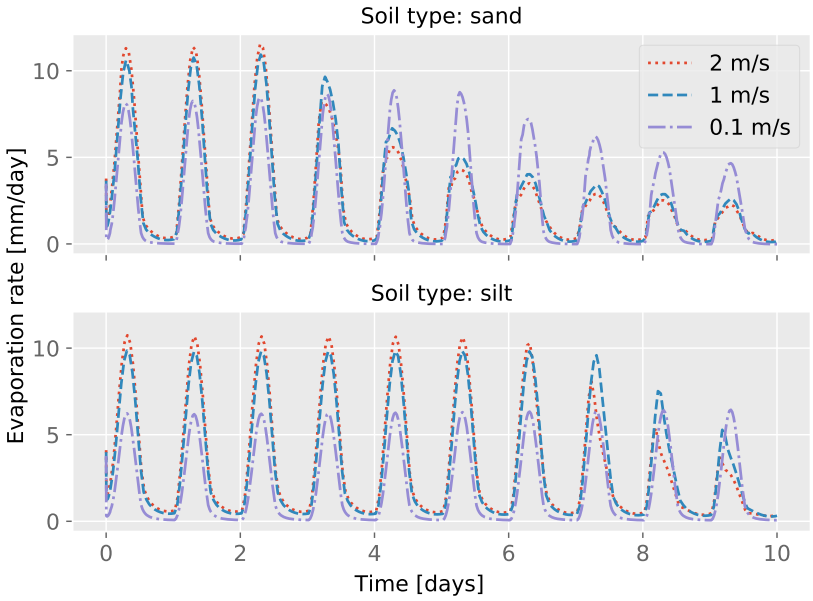

Figure 5.2: Evaporation rates under the influence of solar radiation over 10 days for two different soil types and three different wind conditions. The lowest wind velocity is in the laminar flow regime and the two higher wind velocities in the turbulent regime.

by the ambient conditions. Afterwards, during the transition to stage-II evaporation, the evaporation rates of the two higher wind speeds drop significantly. Water saturation at the interface decreases towards the residual water saturation and evaporation rates are diffusion limited. Daily peaks in evaporation rates can still be seen due to solar radiation. For the lowest wind speed, the transition into stage-II evaporation is slower.

Investigating the silt-type soil, it can be observed that evaporation rates remain in stage-I evaporation much longer compared to the sandy soil; the transition into stage-II evaporation begins for the two higher free-flow velocities only after eight days of simulated time.

The laminar case remains in stage-I evaporation and the daily maximum of evaporation rates does not change substantially. Noteworthy is the lower peak evaporation rates of the silt compared to the sandy soil for the test case with the lowest velocity of 0.1 $\mathrm{m\,s^{-1}}$. This can be explained by considering the different water saturations of the two soil types which lead to different effective thermal conductivities of the soil. For the higher wind velocities, this effect is not visible. Here, the higher flow velocities dominate the fluxes compared to the difference in temperatures between the two soil types.

Comparing the influence of wind velocities shows that during stage-I evaporation, higher wind speeds lead to higher evaporation rates. However, the shape of the curve is still clearly dominated by radiation. The transition into stage-II evaporation happens faster for higher flow velocities as water saturations at the interface decrease more rapidly. During stage-II evaporation (sandy soil, day 7-10), it can be seen that evaporation rates are nearly the same for the two higher velocities. They are not governed by wind velocities any longer but by the properties of the porous medium.

The transition into stage-II evaporation can also be seen in the surface temperatures in Figure 5.3. After the drop in evaporation rates the surface temperatures of the porous medium begin to rise, as the evaporative cooling reduces as well. This can be observed for both soil types, although at different times due to the slower drying of the silt-type soil.

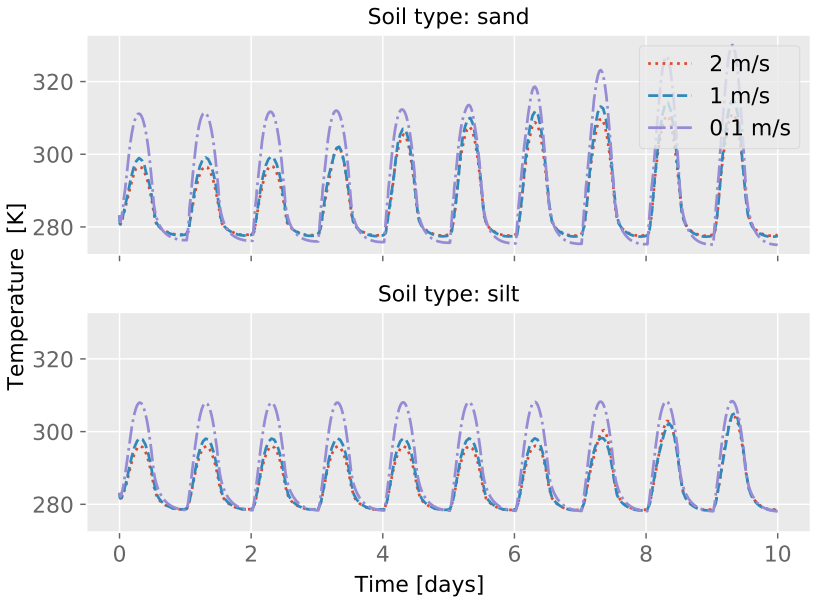

Figure 5.3: Surface temperatures under the influence of solar radiation over 10 days for two soil types and three different wind velocities.

Surface temperatures are not only governed by evaporative cooling but also by ground heat flux and conductive heat exchange with the atmosphere: On the forth day, the simulation result for sandy soil show that for wind velocities of 2 $\mathrm{m\,s^{-1}}$ evaporation rates are lower than for 1 $\mathrm{m\,s^{-1}}$. Still, the surface temperatures show no significant difference, which indicates that higher ground heat flux or conductive heat exchange with the atmosphere mitigate the effect of less evaporative cooling in the case of higher wind velocities.

The laminar test case continuously shows higher surface temperatures than the other two test cases. This can be attributed to the lower evaporation rates and therefore lower evaporative cooling, but also to the reduced conductive heat exchange with the atmosphere, as atmospheric temperatures close to the interface are higher due to less turbulent mixing of the air with the cooler atmosphere above. For the same reason, lower wind speeds can lead to less long wave radiation, which can also enhance peak temperatures.

Comparing the different soil types, it can be seen that the silty soil continuously has lower peak temperatures. This can be explained by the higher evaporation rates; when the sandy soil is already in stage-II evaporation, the silty soil still is in stage-I evaporation, which leads to more evaporative cooling. At the same time the higher water saturations at the interface lead to higher effective thermal conductivity and more ground heat flux, which can additionally lower temperatures at the interface. Net radiation does not vary substantially over the simulated time, but a small decline in net radiation over the ten days can be observed for the silty soil (see Figure 5.4). This decline can be explained by the higher surface temperatures over time, which lead to more long wave radiation and a change in surface albedo with saturation. As shown previously, surface albedo increases when the soil is drying. This leads to more reflection of the short wave radiation, which reduces net radiation. The laminar test case continuously has higher peaks in net radiation than the turbulent cases, which can most likely be explained by to less long wave radiation, as atmospheric temperatures are higher with less mixing in the atmosphere.

Radiation is highest at midday while evaporation rates and surface temperatures have their daily highest peak at 2 p.m.

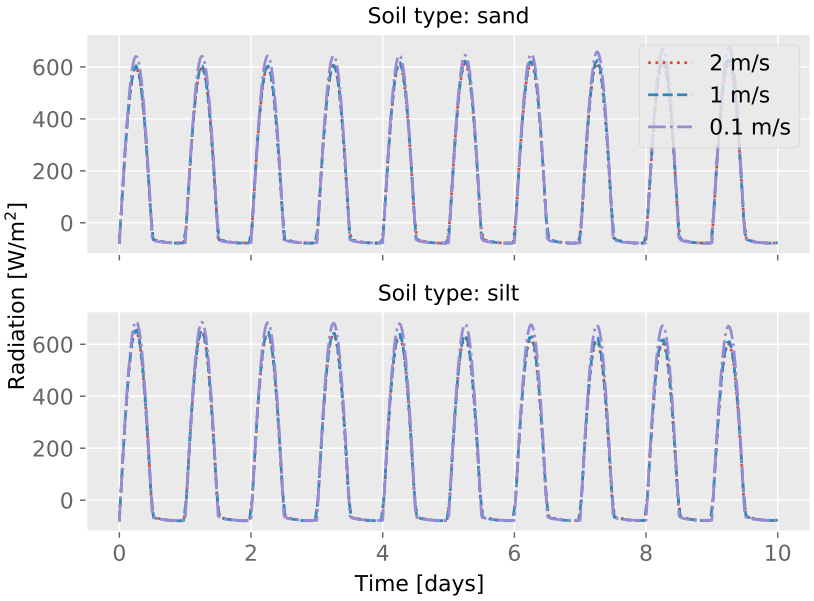

Figure 5.4: Net radiation over 10 days for two soil types and three wind velocities.

5.1.2 Indirect influence of radiation on fluid parameters

Solar radiation provides a substantial amount of energy to the soil surface and in consequence also to the atmosphere above the soil. Some of that energy is consumed by the phase change of liquid water to water vapour, but another part of the incoming energy leads to substantial diurnal interface temperature changes. Due to the dependency of various fluid parameters on temperature, this temperature change is also reflected in changes of those parameters. These temperature variations and their effect on evaporation rates are the focus of this test case, as they can influence the transfer across the interface substantially. A coupled porous-medium free-flow model is ideal for analysing that influence and assessing which process is most influential.

Evaporation across the porous-medium free-flow interface is mostly diffusion dominated, which is why changes in the diffusion coefficients influence evaporation rates. Additionally, changes in the gradient of vapour concentration at the interface between the soil and the atmosphere have an immense effect on evaporation. That is why changes in the boundary layer thickness also affect evaporation. Fluid viscosities and densities are highly temperature dependent and changing their value changes the boundary layer thickness. Additionally, density changes can influence the transfer across the interface due to buoyancy effects as the gas density decreases with higher temperatures. This

can lead to a different vapour concentration in the atmosphere and therefore a different gradient. Additionally, under stage-II evaporation these parameters can have a high influence on evaporation rates by influencing the transport of water vapour in the soil.

To test the influence of radiation on fluid properties and therefore on evaporation rates, a set-up, similar to that of the previous section, using different assumptions about the fluid parameters, is developed. This analysis is conducted for the sandy soil as the silty soil stays in stage-I evaporation and therefore does not offer the possibility to analyse different stages of drying. The set-up varies the influence of temperature on fluid parameters in four different test cases, by assuming a constant temperature in the calculation of these fluid parameter. The four test cases are described as follows:

- Parameters temperature dependent: this case allows an influence of temperature on all fluid parameters.
- Diffusion coefficient temperature independent: sets the temperature constant (283.15 K) for the calculation of the diffusion coefficient.
- Density temperature independent: assumes temperature-independent densities.
- Viscosity temperature independent: this case uses a constant temperature (283.15 K) for the calculation of dynamic viscosities.

Figure 5.5 shows the results for the above described set-up for 10 days of drying.

Most obvious is the effect of the viscosity on the transition into stage-II evaporation. When the influence of temperature on viscosity is neglected, evaporation rates fall faster into stage-II evaporation. This can be explained by considering, that higher temperatures decrease the liquid viscosity of water. When temperatures rise, the lower viscosity leads to a higher mobility of the liquid phase, which facilitates transport of water from deeper soil layers to the drying surface. Therefore, a complete drying of the surface is delayed.

A more detailed analysis can be made, when looking at the influence of fluid parameters on the first and last day of the simulation. On the first day, conditions are clearly in stage-I evaporation and the influence of atmospheric properties dominate. On the last day, under stage-II evaporation the hydraulic parameters in the soil are dominating. Figure 5.6 shows evaporation rates for these days. Here, it can be seen that under conditions that are purely in stage-I evaporation, viscosity and density changes due to temperature do not influence the evaporation rates substantially. A small influence can

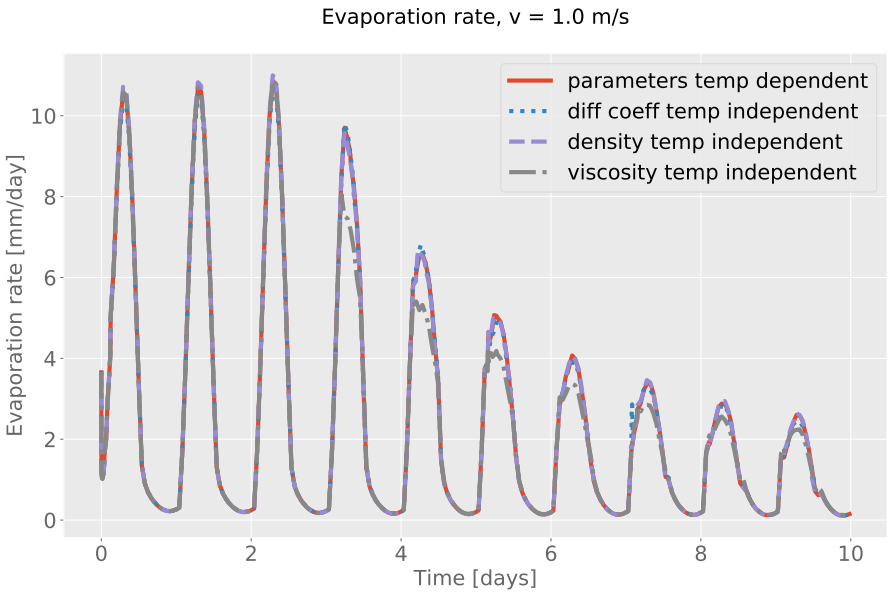

Figure 5.5: Evaporation rates for the four different set-ups, where the influence of temperature on fluid parameters is selectively neglected.

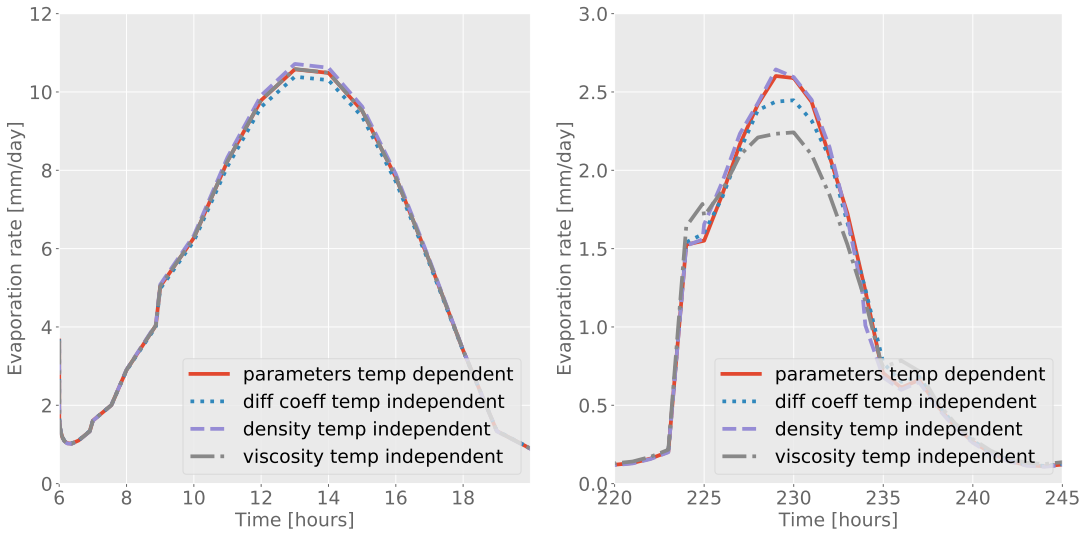

Figure 5.6: Evaporation rates for the four different set-ups for the first and last day (day 10) of the simulation. The drop in evaporation rates in the morning of the tenth day is due to local drying processes.

be detected for diffusion coefficients. When diffusion coefficients are higher due to higher temperatures, this increases evaporation rates. Under stage-II evaporation, the influence of the temperature dependency of the fluid parameters is higher. As described before, viscosity has a high influence but also the influence of diffusion coefficients increases, as evaporation is limited by the diffusive flux in the soil. In conclusion, under stage-I

evaporation the main influence of radiation on evaporation rates can be attributed to the higher phase change from liquid water to water vapour and not to changes in transport parameters. Under stage-II evaporation, the influence of temperature on the transport parameters becomes higher and the changes in fluid parameters due to temperature enhance the transport of water vapour into the atmosphere.

5.1.3 Influence of surface undulations

Natural soil is seldom completely flat, e.g. tilled soil often exhibits very irregular surface forms, which is why the analysis of surface undulation is important to asses evaporation rates under natural conditions. Surface undulations can affect the evaporation rates in various ways: (I) They increase the surface area, leading to a higher exchange area for evaporation. (II) They can reduce the overall wind flow velocities in the valleys, leading to less mixing and increased water vapour content in the valleys, reducing evaporation rates. (III) At the same time, an increased turbulent mixing can also enhance evaporation rates. This depends highly on the spacing and amplitude of the surface obstacles [Coltman et al., 2020]. (IV) Additionally, higher surface undulations might reduce the water availability in the hills as capillary forces can be too weak to overcome gravity.

An interesting aspect in that regard is the different flow behaviour on the sides of the hills turned towards and away from the wind. As evaporation rates in the viscous sublayer are diffusion limited, the thickness of this layer is an important factor in determining evaporation rates. Obstacles can influence that layer tremendously. Around the obstacle, boundary layers will detach and reattach downstream, depending on the geometry of the surface and the wind velocity. In the valleys, eddies can occur, that can either increase of decrease evaporation rates locally depending on their connection to the main flow [Coltman et al., 2020].

Including radiation in a model with an irregular surface structure poses a few additional challenges: (I) The shadow length has to be accounted for, which reduces solar radiation in the valleys depending on the angle of the sun. (II) The angle of the surface towards the sun needs to be accounted for in the calculation of solar irradiance when solar radiation varies in a diurnal cycle.

To assess the influence of non-flat surfaces, in the following different set-ups are compared:

- 5 cm hills: The set-up with the same boundary and initial conditions as in Figure 5.1 is analysed with five hills with 5 cm height.
- 2 cm hills: The same set-up for 2 cm high hills and the differences between the different heights are compared.
- Reversed flow direction: A case where the wind flow direction in relation to the diurnal cycle of the sun is reversed (sun rises on the right and sets on the left) is analysed in comparison to the previously described case.

The set-up and its boundary conditions are very similar to the previously described flat set-up. A detailed description can be found in the appendix in Figure B.1. The spatial parameters of the soil are taken from the sandy soil, as analysed in the flat set-up as well.

The influence of radiation on evaporation rates can clearly be seen in Figure 5.7. Here, the velocity distribution in the atmosphere and the saturation in the porous medium at 4 p.m. and at night at 10 p.m. are presented for a set-up with five hills. Isolines, representing a water saturation of 0.025, show the local drying pattern, influenced by solar radiation.

It can be observed that flow velocities are higher at the top of the hills on the side facing the wind. In the night, without radiation, this location at the top of the hills is the region where saturations are lowest. Higher flow velocities lead to more mixing and enhanced evaporation. During the afternoon, the sun shines directly on the sides turned away from the wind, heating up the soil and leading to higher evaporation rates on those sides. Water saturation is then lower at these locations, which shows that here radiation dominates the drying behaviour in contrast to wind conditions that govern the process during the night.

Figure 5.8 shows a comparison of evaporation rates, average net radiation, and the average surface temperature for two different heights of obstacles. Here, it can be observed that at first, when the sun rises in the morning, net radiation is higher for smaller undulations. This is because shadow lengths are shorter when obstacles are smaller, limiting the area that is in the shade. This is also reflected in higher evaporation and higher temperatures for lower hills, especially visible at 7 a.m.

Later in the day, when shadow lengths decrease, that effect is dominated by the higher surface area of higher undulations. More surface area is directly exposed to the sun,

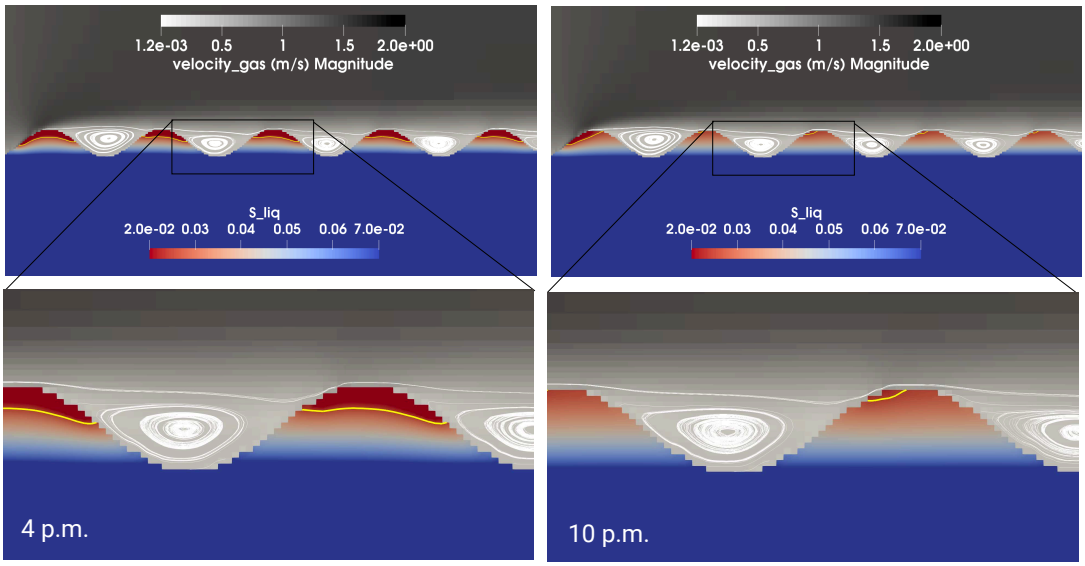

Figure 5.7: Velocity distribution in the atmosphere and saturation distribution in the porous medium. The yellow lineshows the value Sw = 0.025. Above that line saturations are lower than that value. *Left* at 4 p.m. and *right* at 10 p.m.

which increases surface temperatures and evaporation rates of the higher undulations. Around 9 a.m. the 5 cm high hills start to dry locally, when capillary forces are not high enough to continuously supply water, which leads to the sharper change in evaporation rates at that time.

At 12 p.m. higher obstacles lead to a smaller peak in net radiation, as the surfaces are more inclined. Therefore, at midday the sun is not perpendicular to the whole surface and net radiation is smaller. This can also be seen in the evaporation rates. Locally, the evaporation rates [mm/day] are lower for higher obstacles, which is influenced by the lower net radiation. However, integrated over the whole surface area, higher obstacles lead to more surface area, which increases the energy input into the system and also mass loss of water.

The changes in surface temperature due to the difference in height of the hills reflects the above described effects which have a contrary influence on temperatures: higher energy input due to more surface area increases the temperature, but at the same time, the higher mass loss of water leads to a cooling of the surface. Here, it can be seen that surface temperatures are lower for higher obstacles, as more water evaporates.

Although the average surface temperature is higher for lower hills, the atmospheric temperatures not necessarily reflect that. For higher undulations atmospheric temperatures

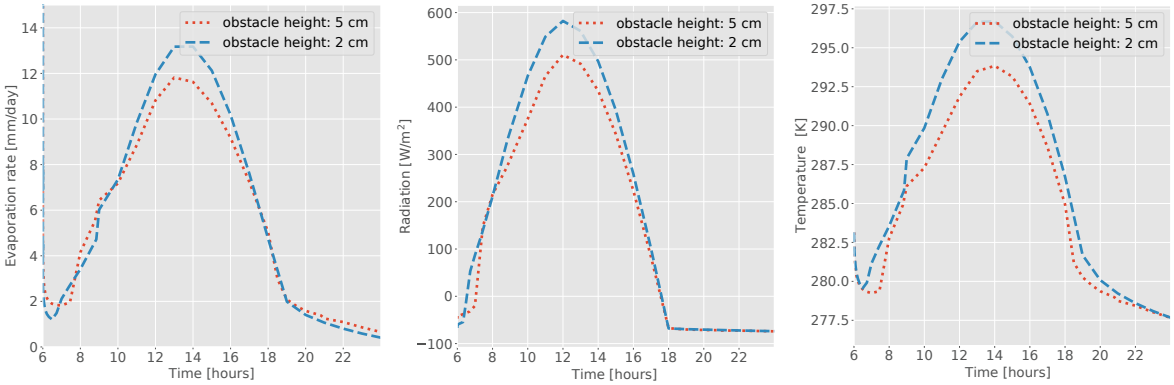

Figure 5.8: Evaporation rates (*left*), net radiation (*middle*), and average temperature at the interface (*right*) for different heights of surface undulations.

in the valleys between the obstacles can still be higher due to less mixing, which can be seen in Figure 5.9. Here, the valleys between the 5 cm hills are clearly influenced by the eddy, forming in the valley. Temperatures are the highest on the left side of the valley, because the warmer air is rotated in that direction. For the 2 cm high hills, that effect is not that visible, but the temperatures are also higher directly in the valley due to the higher surface temperature but decrease faster in the free flow, due to more mixing with the turbulent atmosphere.

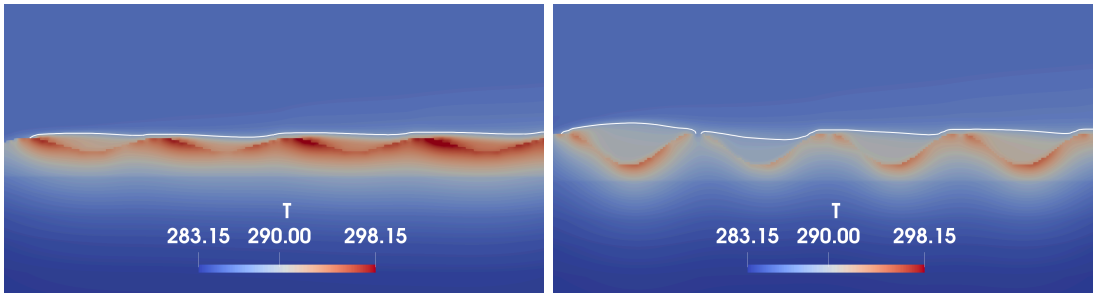

Figure 5.9: Temperature in the atmosphere and in the soil at 12 p.m. The white line shows a temperature of T = 288.15 K. Below that line, values are higher. *Left* for 2 cm high hills, *right* for 5 cm hills.

The previous example showed a set-up where the sun rises on the left side of the domain and sets on the right, which is also the direction of wind flow. To test if changing the flow direction in comparison to the sun changes evaporation rates substantially, another test case is implemented where the sun direction is reversed.

The case where the sun rises on the left and sets on the right is in the following referred to as case 1 and the reversed case (sun rises on the right side and wind flows from left

to right) as case 2. To get a better distinction between the effects of wind velocity and radiation, the wind velocity is increased to 2 $\mathrm{m\,s^{-1}}$.

Comparing these two cases in Figure 5.10, there is only a small variation in overall evaporation rates for the tested parameter set. Evaporation rates in the morning are higher for case 2 but lower in the afternoon. That can be explained by considering that both radiation and wind velocities raise evaporation rates. For case 1, in the morning the sun shines on the left sides of the small hills, the same side exposed to the most wind. Locally, that side dries considerably faster: there are spots where the capillary forces cannot supply enough water and there is a transition into stage-II evaporation, which lowers the overall evaporation rates. The reversed case splits the evaporative driving forces for evaporation radiation and wind velocity in the morning to different surface sides of the hill. This leads overall to higher evaporation rates as fewer spots dry out completely. This is supported by analysing the water saturation on the right side in Figure 5.10, where it can be seen that at 10 in the morning water saturation are lowered on both sides of the hill for case 2, while for case 1 only at the side facing the wind water saturation are considerably lower.

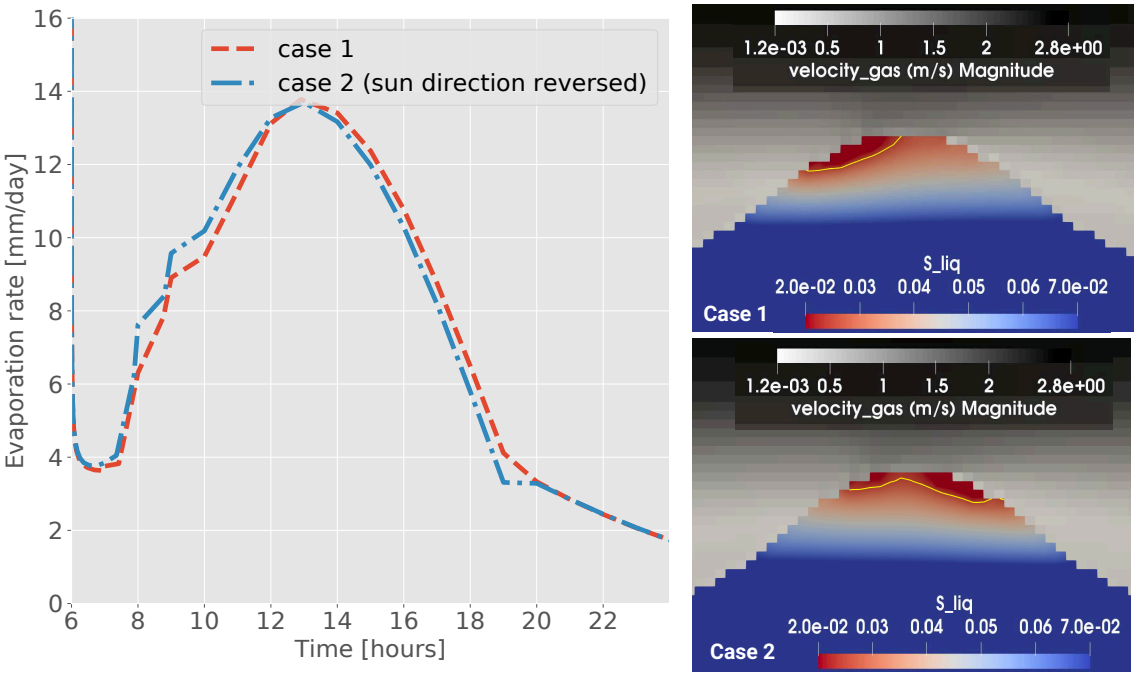

Figure 5.10: *Left:* Evaporation rates for two scenarios over the course of one day. Case 1: the sun rises on the left and sets on the right, and case 2: the reversed case. *Right:* Water saturation at 10 a.m. for both cases. The yellow line shows a saturation of Sw = 0.025. Above the line, saturations are lower.

In the afternoon, evaporation rates for the reversed case are lower, as the sun then shines directly on the left sides of the hills, which are already dryer due to the exposure to wind. Overall, it can be seen that these effects for the tested case are not dominant and the cumulative mass loss over the whole day is comparable for both cases. This result is of course very dependent on initial saturations and soil properties, when saturations are higher and the soil does not dry out at all, evaporation rates will not be that much influenced by the location of radiation compared to wind velocities.

5.1.4 Summary

The process analysis shows the high influence of radiation on evaporation rates. A diurnal cycle governs evaporation under stage-I and stage-II evaporation. Peak temperatures are controlled by evaporative cooling and rise substantially after a transition into stage-II evaporation. The analysed silty soil stays longer in stage-I evaporation compared to the sandy soil due to higher capillary forces. Comparing wind velocities shows that under laminar conditions, evaporation rates are lower in stage-I evaporation but stage-I conditions prevail longer. Due to the lower evaporation rates and less conductive heat exchange with the cooler atmosphere, surface temperatures are higher under laminar conditions. Net radiation does not vary substantially with wind velocities but small changes are visible which can be attributed to changing albedo values with saturation and changes in surface temperatures, which influences the amount of long wave radiation.

Under stage-II evaporation changes in fluid parameters due to temperature have a high influence on evaporation rates. Higher temperatures of the soil lead to higher diffusion coefficients, lower density and lower liquid viscosity. This raises evaporation rates. If these influences are neglected, predicted peak evaporation rates are considerably lower.

The influence of porous surface obstacles is analysed by comparing five hills with varying height. It can be seen that radiation leads to a distinct drying pattern that governs evaporation rates. During the night, the highest evaporation rates can be observed at the sides facing the wind as is expected when no radiation plays a role, as the viscous sublayer thickness is lowest at these locations. During the day, the highest evaporation rates can be observed at the location where the sun shines perpendicular to them. Here, the temperature increase and therefore higher vapour pressure has the dominating effect on evaporation rates. Higher obstacles lead to lower peak radiation rates and consequently to lower peak evaporation rates. Changing the wind direction in relation to the cycle of

the sun does not have a high impact on evaporation rates integrated over a whole day. During the diurnal cycle evaporative fluxes are slightly higher in the morning, when the sun shines on the hills facing away from the wind, but lower in the afternoon, where the sun shines on the already drier sides of the obstacles turned towards the wind. This leads to small differences in the drying pattern on the hills and small differences in overall evaporation rates.

5.2 Comparison with experimental lysimeter data

Assessing the capabilities of the model by comparing results with experimental data is important to evaluate if the relevant processes are captured adequately.

Here, a comparison is conducted with data measured from soil lysimeters in the TERENO SoilCan Selhausen test site at the Forschungszentrum Jülich, Germany (50° 52' 8.6" N, 06° 27' 57.2" E). This test site is part of the TERENO Rur observatory [Zacharias et al., 2011]. Measurement data from two different years are selected. One period from the year 2016 (September, 06th - September, 08th), where conditions are very dry and one period from the year 2017 (August, 26th - August, 28th), where measured evaporation rates are higher. The days are chosen so that no precipitation occurred in that time to only analyse evaporation. The spatial parameters that are used for the analysis belong to the soil Sauerbach (ID: Sb-10) and are summarized in the appendix in Table B.1.

Additionally, wind velocity measurements, air temperatures, and relative humidity data measured in 2 m height are used as input data for the boundary conditions of the free flow. Figure 5.11 shows a sketch of the experimental set-up with the location of measurement and the boundary conditions for the simulation set-up.

Only the first two horizons of the soil are modelled and a dirichlet condition is set at the bottom of the porous medium domain to mimic recharge of water from lower soil layers. During the measurement time, measured values of the water saturation lower than the first 50 cm do not show substantial changes, which justifies that choice of boundary conditions. The initial conditions can be found in the appendix in Table B.2 and in Figure 5.12 the input data for the two years for the free-flow can be found. Atmospheric conditions show a very clear diurnal cycle with high temperatures and wind velocities during the day and higher relative humidity during the night.

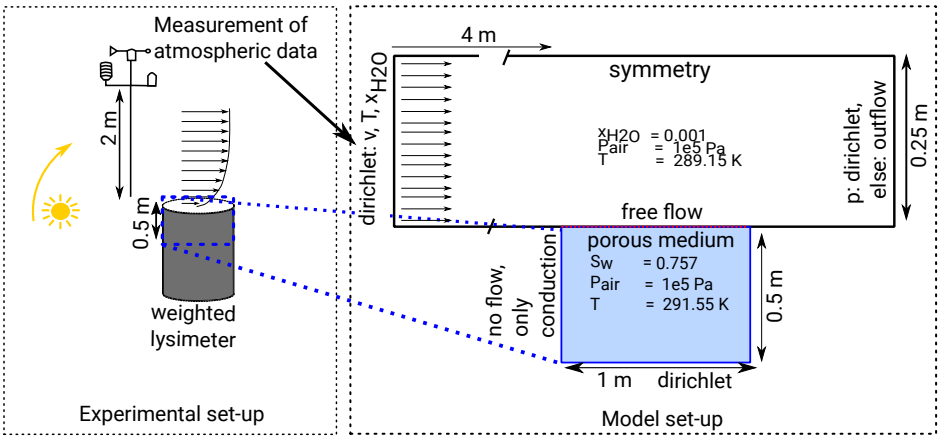

Figure 5.11: Experimental set-up of the lysimeter with measurement of the atmospheric parameters in 2 m height and initial and boundary conditions for the model set-up. The problem is discretized with 75 cells in the horizontal direction and 80 in vertical direction with a refinement towards the interface. The free flow domain is extended at the front to provide a better flow profile.

An initial comparison of measured radiation data showed, that in 2016 the maximum value for net radiation was considerably lower than for 2017. To be able to compare simulated data with measured values, for 2016 the maximum value of solar irradiation was lowered to 600 W/m^2. The lower value might be explained by more cloud cover in these days.

Figure 5.13 shows a comparison of the radiation data obtained by the measurements and the simulated data. It can be observed that in 2016 the measured and simulated values for net radiation show a very good match. In 2017 on the first day, net radiation is overestimated. This can most likely be explained by more cloud cover on that day, which lowered the maximum solar irradiance. As in the model the same daily maximum value for solar irradiance is assumed, this variation cannot be captured by the model.

Figure 5.14 shows evaporation rates for both years. Here, it can be observed that in the year 2016 evaporation rates are overestimated drastically, while in 2017 evaporation rates at least for the last two days match well.

As radiation matches well with measured values in 2016, the difference cannot be explained by differences in solar radiation. In 2017 the difference of evaporation rates between measurement and simulation on the first day is most likely explained by the overestimated net radiation. On the second and third day, when the match for net radiation is better, also evaporation rates are better approximated. A possible reason for

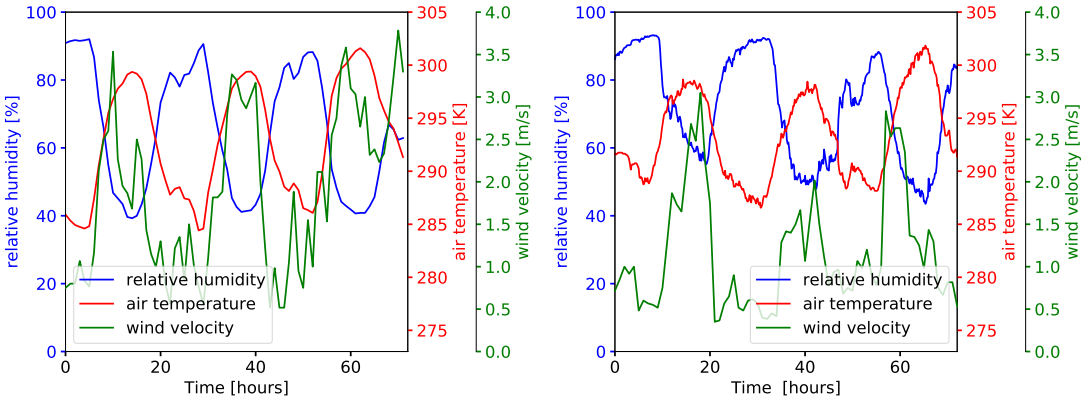

Figure 5.12: Atmospheric measurement data for the year 2016 (*left*) and 2017 (*right*) used as input parameters for the free flow.

the small discrepancy can be most likely found in wind velocities. As a model input averaged wind velocities are used as can be seen in Figure 5.12. Rapid fluctuations in wind velocity cannot be captured which might explain the differences.

In order to assess why evaporation rates are not well matched for the year 2016 several model and parameter uncertainties are evaluated in four different model set-ups:

a) Unchanged set-up: Spatial parameters taken from the measurement are used as well as the initial and boundary conditions as described before.

b) Extended porous medium: One uncertainty of the set-up as described before is the relative humidity in the boundary layer. In the measurements this value is obtained in 2 m height. However, it does not contain any information about the values close to the interface. As the wind flows over an open field before reaching the measurement site, it is possible that the relative humidity in the boundary layer is higher than the value obtained in the measurements. To asses that influence, the porous medium domain as well as the free flow are prolonged by 10 meters upstream of the measurement site. This means the air close to the interface is more enriched with water vapour once it reaches the measurement site. This artificial prolongation does not replicate reality: the soil type next to the lysimeters is different or there might be vegetation disturbing the flow field. Regardless, this set-up makes it possible to evaluate the effect the relative humidity has on the exchange between the soil and the atmosphere.

c) Initial saturation and temperature at the interface: Another uncertainty of the model is choosing the initial saturation and temperature. These values are not

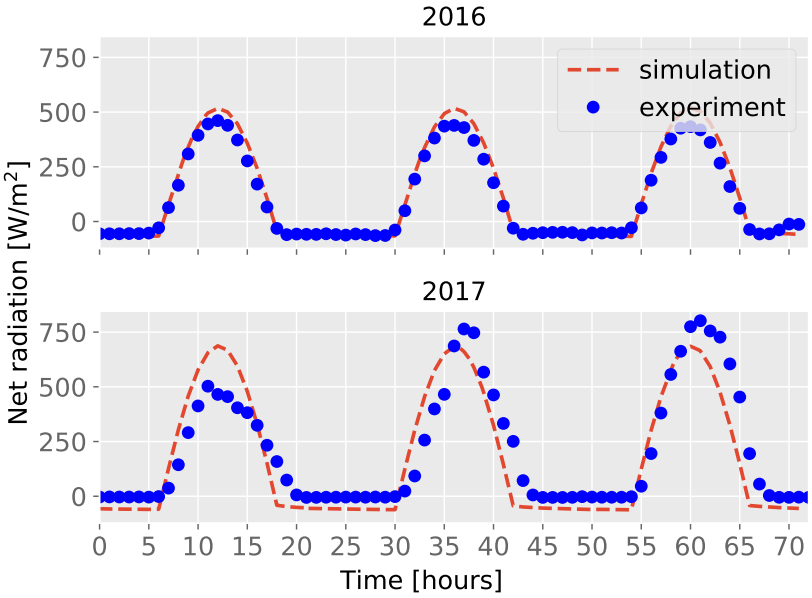

Figure 5.13: Comparison of measured radiation data with simulated data for the years 2016 and 2017.

measured right at the interface but in the soil in 10 cm depth (water saturation) and in 30 cm depth (temperature). As the water saturation and temperature close to the interface have a great impact on evaporation rates a test case is set up, varying these parameters in the first centimetre. The initial temperature is reduced by 4 °C and the initial water saturation is lowered to 0.7.

d) Spatial parameters at the interface: Various studies (e.g. [Dimitrov et al., 2015]) show that soil parameters are very sensitive to the treatment of the soil. The Sb-10 soil was tilled and smoothed again by raking, which is why it is possible that hydraulic parameters of the soil at the interface are different from the initially measured values. To test that hypothesis, the van-Genuchten parameters for the upper 3 cm are changed for one test case to Snr = 0.2, α = 7.54e-4 [1/Pa] and n = 1.6.

The result for these four cases can be found in Figure 5.15.

As (case a) describes the results also shown in Figure 5.14 the same deviation between measurement and experiment can be seen. Additionally, it can be observed that the initial surface temperature and initial water saturation (case c) do not influence evaporation rates. Only in the very beginning evaporation rates are lower than for (case a) lower. Afterwards no difference between (case a) and (case c) can be observed. The

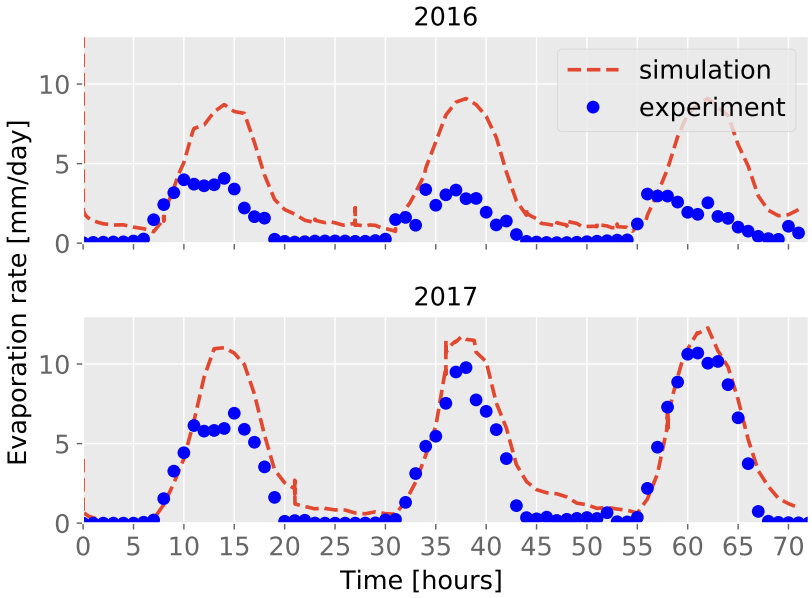

Figure 5.14: Comparison of measured evaporation rates with simulated data for the years 2016 and 2017.

given capillary pressure saturation relationship for Sb 10 allows capillary rise of water during the whole time and the soil does not dry out during the whole simulated time, meaning evaporation conditions are continuously in stage-I evaporation and governed by atmospheric conditions rather than soil conditions.

The extension of the porous medium by 10 m (case b) leads to a drastic reduction in evaporation rates, especially on the first day. This shows that measurements of the relative humidity closer to the interface between soil and atmosphere would be necessary to assess if the model then represents the experimental measurements more closely.

Changing the spatial parameters of the first 3 cm (case d) changes the overall result considerably, as with the chosen spatial parameters the capillary pressure is not high enough to supply water to the first layer and evaporation becomes diffusion limited. With this change in parameters, the measured and simulated evaporation rate are within the same order of magnitude. This indicates that indeed the treatment of the soil changed the parameters of the first layer, as with the previously set parameters (case c) a drying of the soil to a diffusion limited evaporation range was not possible.

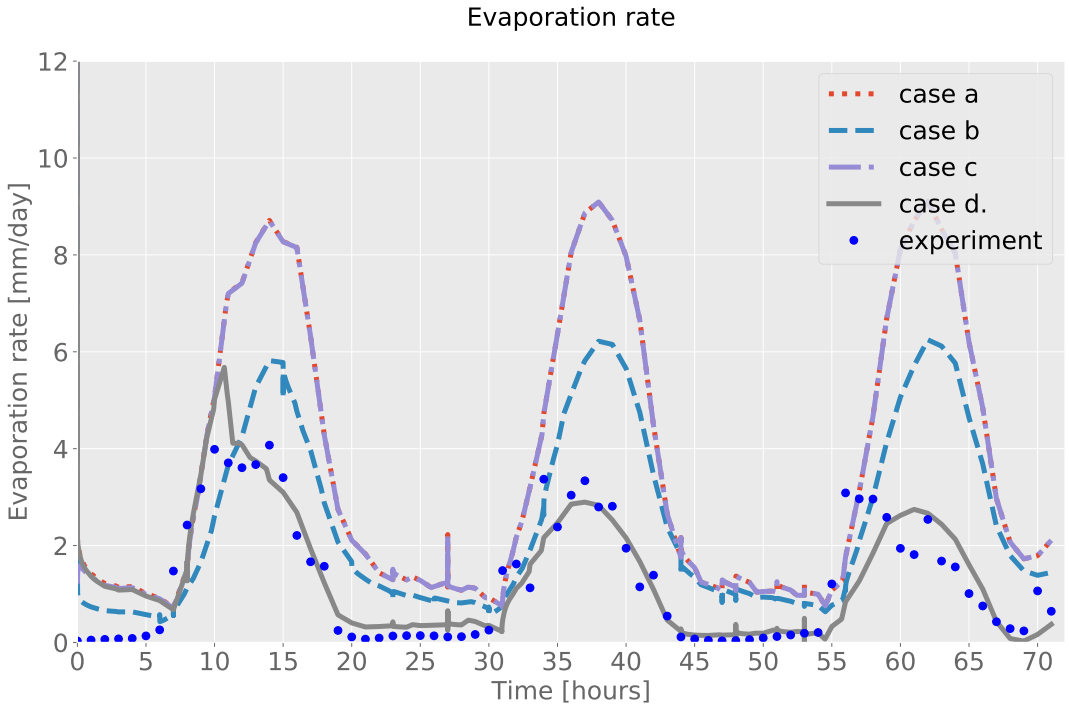

Figure 5.15: Comparison of evaporation rates with measured values for the four different tested cases.

5.2.1 Summary

Evaporation rates and net radiation measured in a lysimeter at the Selhausen test site of the TERENO SoilCan project are compared for two different time in the years 2016 and 2017. Initial conditions for the soil and the atmosphere are taken from the measurements. The atmospheric data used as a boundary condition for the free flow consists of relative humidities, wind velocities and air temperature. These values are taken in 2 m height and set as input values on the boundary.

The compared simulated values for the selected days in 2017 show a good match with experimental values. Evaporation rates are in stage-I evaporation and the predicted and measured values show a comparable match. On the first day net radiation is lower in the measurements than in the model results which also then leads to lower evaporation rates. In the simulation, the daily peak in solar irradiation is constant, which is why the changes observed in the experiments are not reproduced well. For the two following days net radiation values match better and evaporation rates are well approximated.

However, in the selected test days in the year 2016 the evaporation rates are highly

overestimated, although net radiation rates matches well. As parameters close to the interface have a high influence on evaporation rates, several uncertain model parameters are varied to test their influence. It is found that with the given van-Genuchten parameter the predicted evaporation rates are continuously in stage-I evaporation and higher than the measured values. A reduction can be reached when prolonging the porous medium by 10 metres upwind of the measurement site. With that the water vapour content in the viscous sublayer is higher when reaching the measurement site, which reduces evaporation rates. However, they are still higher than the measured evaporation rates.

A better match can be found when varying the spatial parameters for the first three centimetres of the soil. This variation for the first soil layer can be explained by soil treatment. Before the start of the measurement, the upper layer of the soil is tilled and then smoothed again, which likely disturbed the layer and can lead to different capillary pressure- saturation relationships [Dimitrov et al., 2015]. With different van-Genuchten parameters, a complete drying of the upper soil layer is possible and evaporation rates are in stage-II evaporation. These values then show a better match with the measured values, indicating that indeed the upper soil layer is completely dry in the measurements. As saturations are only measured in 10 cm depth, this cannot be verified by the measurement though.

6 Results and discussion II - Investigation of multicomponent transport

This chapter aims to analyse multicomponent flow and transport for various flow dynamics and set-ups. The first two sections present a process analysis for single- and multiphase porous-medium systems coupled to a free flow. The following components are analysed: nitrogen and oxygen, the main components of air, methane and carbon dioxide, the main greenhouse gases, and water, the main component of the liquid phase. Methane and carbon dioxide are not only interesting as greenhouse gases, additionally their fluid properties are different from air, with methane as a lighter component and carbon dioxide as a heavier component. Therefore, selecting them as the components of interest enables the analysis of different fluid properties as well.

The last section of this chapter presents a benchmark study for multicomponent transport, where results for a single-phase porous medium system coupled to a free-flow obtained in DuMu^{x} are compared to results from the simulation software COMSOL Multiphysics®.

6.1 Process analysis

In order to evaluate the different processes relevant for mass, momentum, and energy transfer between a porous medium and the atmosphere, a numerical model can help to analyse these different processes by varying soil parameters and fluid properties.

To that end, first a relatively simple flat set-up is used to investigate the transport behaviour of multiple components with varying properties in a single-phase and a two-

phase setting. Then, the analysis moves on to a more complex set-up where also surface undulations are incorporated and their influence on the transport of the components is shown.

6.1.1 Single-phase analysis

As previously discussed, the presence of components can change the whole mixture behaviour, and as a result change the transport of the whole phase. To reduce complexity and separate processes, this analysis starts with a two component system so that multicomponent diffusion processes do not influence the system.

In such a system the influence of different diffusion coefficients of the components is straight forward to analyse, as higher or lower values linearly increase or decrease the diffusive flux. Therefore, in the following example, the same diffusion coefficient for all components is assumed, so that only the mixture behaviour and it's influence on the transport process is relevant. The set-up is used to describe the transport of three different components: nitrogen, as a component with the same density and viscosity as the bulk phase, as well as methane and carbon dioxide, both with lower viscosities than nitrogen. The densities of these components are higher (carbon dioxide) and lower (methane) than nitrogen. The mixture behaviour is computed according to the relationships described in Table 2.1, but all binary diffusion coefficients are set to $D_g^{ij} = 1 \cdot 10^{-5} \mathrm{m}^2\,\mathrm{s}^{-1}$.

A single-phase set-up has the advantage that isothermal processes can be assumed. In a multiphase set-up with evaporation, the additional drying and evaporative cooling influence viscosities and densities as well, which makes it more difficult to analyse the processes separately.

As this set-up focuses on the mixture behaviour, only one soil type is investigated. The spatial parameters for the set-up are chosen for a sandy soil and specified in the previous chapter in Table 5.1. Details can be seen in Figure 6.1. It consists of a flat porous medium and a free-flow above. The dirichlet boundary at the bottom is fixed ($x = 1$) for the component (nitrogen, methane or carbon dioxide) so that after a while steady state transport is established.

In the following, two different free-flow conditions are compared. One turbulent test case, with a maximum velocity of 1 $\mathrm{m\,s^{-1}}$, and a laminar case, with a flow velocity of 0.1 $\mathrm{m\,s^{-1}}$.

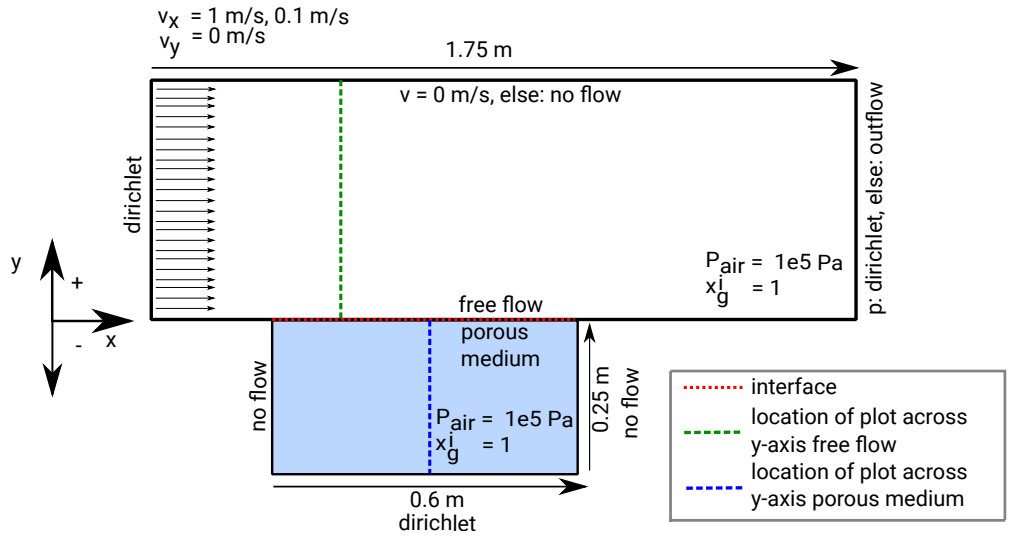

Figure 6.1: Set-up for the process analysis of multicomponent transport in a dry porous medium coupled to a free flow. The gas pressure in both domains is set with 1 bar pressure at the interface and a hydrostatic distribution in the free flow and the porous medium, depending on gas density. The example is discretized with 70 cells in the horizontal direction and 80 cells in vertical direction. The blue and green line indicate the locations where model results are evaluated across the y-direction in the free flow and the porous medium.

Turbulent conditions

Figure 6.2 shows the transport rate across the interface over time for the three different components. Additionally, the velocity in x-direction is plotted over the y-axis in the free flow, to evaluate if the transport of a component with a different viscosity and density than air changes the flow behaviour and with that the momentum boundary layer in the free flow.

Figure 6.2 additionally shows the influence of viscosities, displaying transport rates for the components when the viscosity is set to that of nitrogen. In that case, only different densities influence the transport.

Transport rates for the three components are clearly different, although the diffusion coefficients are uniform. This cannot be attributed to variations in the free flow. The flow profile in the free flow does not seem to be influenced by the presence of components, as the velocity profile for all three cases is nearly identical. Wind velocities are most likely predominant for the development of the viscous sublayer and changes in viscosities or densities are too low to impact that substantially. In the soil though, the different

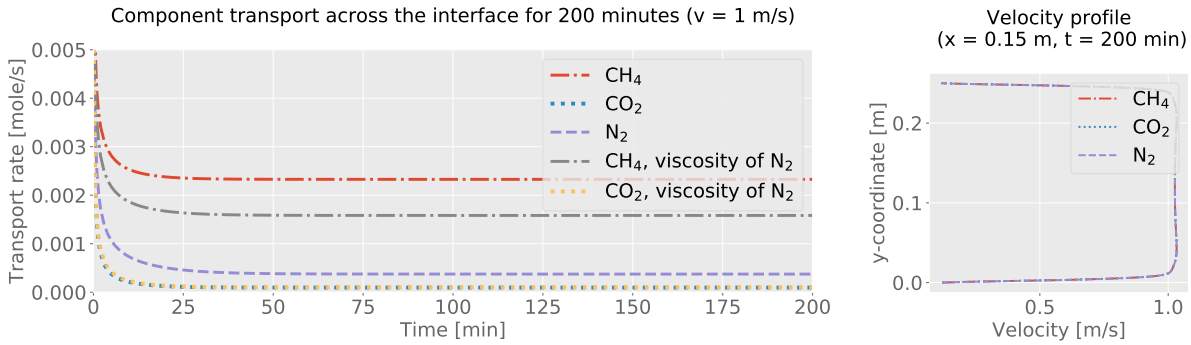

Figure 6.2: Transport across the interface for three different components over time (*left*) and velocity in x-direction plotted across the y-axis (green line in Figure 6.1) in the free flow after 200 minutes (*right*).

densities of the gases lead to buoyancy effects, which change the gradient of concentrations and therefore also the transport into the atmosphere, which explains the different transport rates for the three components.

The analysis for different viscosities shows that not only densities influence the transport: This can be seen for two simulation runs in Figure 6.2 where the changes in viscosity due to the presence of methane and carbon dioxide are neglected and it is assumed that the viscosity of the mixture is that of nitrogen. Here, the most dominant change can be seen in the behaviour of methane: Methane transport is continuously lower when the viscosities are not changing with the presence of the component. Methane has a lower viscosity compared to nitrogen. This viscosity difference can affect the flow resistance and therefore facilitate the buoyancy effect under the given boundary conditions where the pressure and the mole fraction at the bottom are fixed.

Bahlmann et al. [2020] show that the presence of components with different densities can change the momentum transfer into the porous medium substantially. It is shown that gases with a lower density are more affected by momentum transfer from the porous medium into the free flow than heavier gases. This is also visible in Figure 6.3, where mole fraction across the y-axis in the porous medium are displayed along with the velocity in x-direction.

One can see that in the porous medium the methane concentration is clearly influenced more by the momentum transfer than the other components. The comparison with the results for a fixed viscosity additionally shows that also mixture viscosities can influence the momentum transfer between the porous medium and the free flow. When the mixture viscosity is calculated as a mixture of the viscosities of methane and nitrogen, the velocity

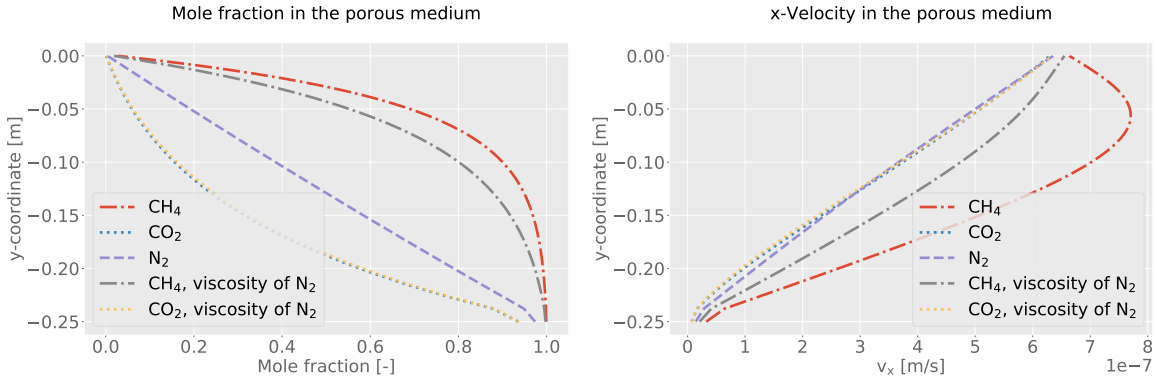

Figure 6.3: Mole fractions and x-velocity in the porous medium after 200 minutes for three different components plotted across the y-axis (blue line in Figure 6.1). Additionally, two test cases analyse the influence of viscosity by not changing viscosities with composition.

in x-direction clearly increases. When the mixture viscosity is calculated as that of nitrogen, velocities in x-direction in the porous medium are lower and methane transport towards the right boundary of the porous medium decreases, which results in a flatter, more linear increase of methane from the lower boundary towards the top (Figure 6.3 on the left). Lower viscosities lead to a slower dissipation of the momentum which is transferred from the atmosphere into the subsurface, which enhances the influence of momentum transfer. As methane has a lower density and a lower viscosity than air, this component is therefore very likely to be influenced by wind induced transport in the subsurface.

Laminar conditions

The same set-up as before but with a maximum velocity of 0.1 $\mathrm{m\,s^{-1}}$ is used to analyse the transport under laminar conditions. Figure 6.4 shows the results for the transport of the three components over time as well as the velocity profile in the free flow after one minute and after 200 minutes. The presence of components in the free flow clearly also changes the flow dynamic near the interface as can be seen on the middle and right part of Figure 6.4.

This can further be analysed in Figure 6.5: The change in the pressure gradient due to the release of gas with a lower or higher density from the porous medium into the free flow leads to a detachment of the boundary layer. For laminar flow this is possible even for small pressure differences, as then the pressure and viscous force dominate over the

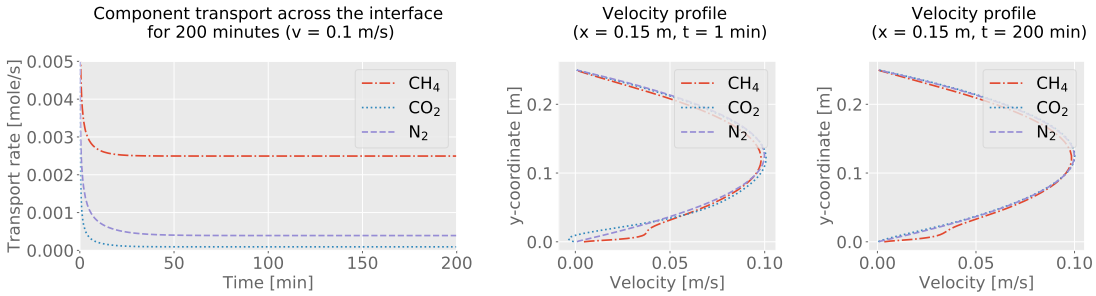

Figure 6.4: Transport across the interface for three different components over time (*left*) for the laminar test case and velocity in x-direction plotted over the y-axis in the free flow after 1 minute and 200 minutes.

inertia force. In front of adverse pressure gradients, the boundary layer can then detach and reattach downstream [Schlichting and Gersten, 2006]. For the simulation where CO_2 is present, this detachment happens at the beginning of the porous medium due to the increase in pressure when heavier carbon dioxide migrates into the free flow. When CH_4 is present the boundary layer detaches downstream of the porous medium, as due to the presence of the lighter methane in the boundary layer above the porous medium, the pressure increases downstream, where methane concentrations are lower. In general,

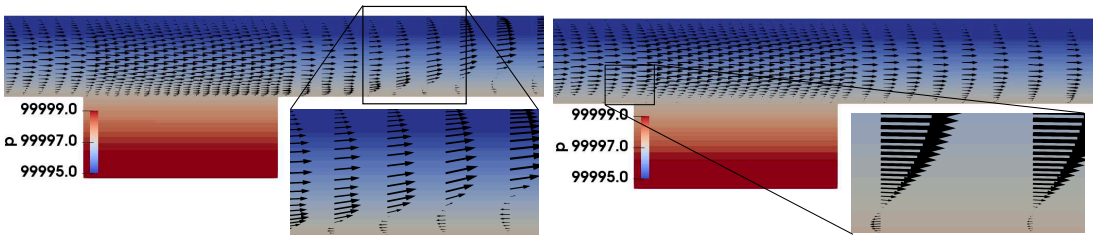

Figure 6.5: Pressure distribution after 1 minute for CH_4 (*left*) and CO_2 (*right*) for the laminar test case. The arrows indicate flow direction and magnitude of the free-flow velocity.

the flow is still limited by the transport through the porous medium, though and not governed by the free-flow process as the transport rates are very comparable to that of the turbulent case.

6.1.2 Multi-phase analysis

The following example analyses the effect of various different parameters on the mass, momentum and energy transport across the free-flow porous-medium interface when the soil is partially saturated with water. The first set-up consists of a flat porous

medium and a adjacent free flow, where fresh air is flowing from left to right. In contrast to the previous example, here the real mixture behaviour is considered, that means diffusion coefficients are computed depending on temperature and pressure and the phase compositions are calculated as described in Chapter 2. Later a set-up with a small obstacle is analysed to include more complex flow dynamics in the free flow and analyse how they influence the transport of the components.

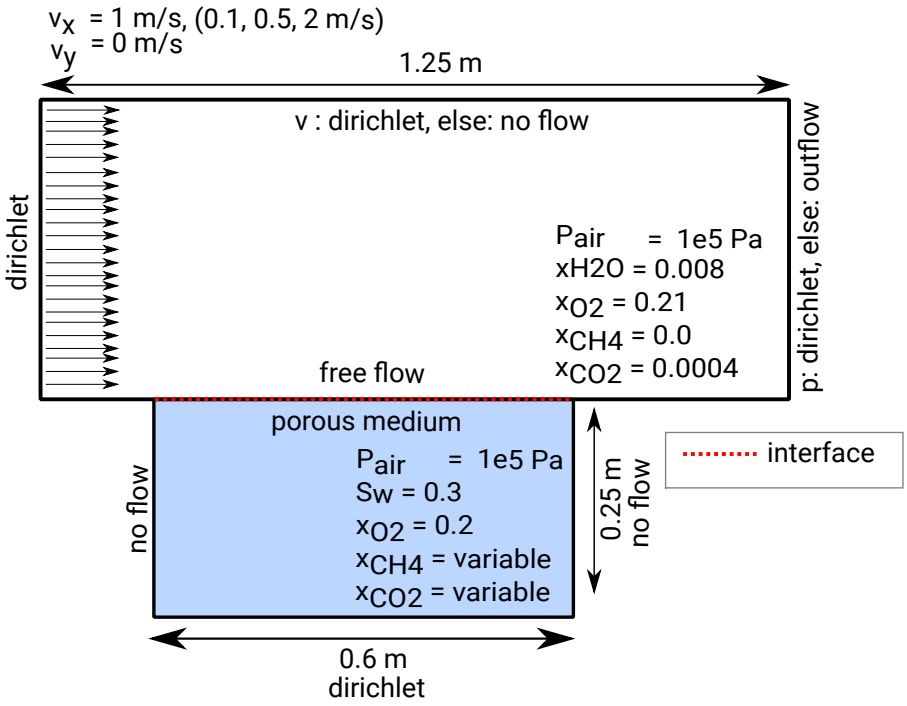

Figure 6.6: Set-up for analysing multicomponent behaviour for a flat surface when the porous medium is partially saturated with water. The gas pressure in both domains is set with 1 bar pressure at the interface and a hydrostatic distribution in the free flow and the porous medium, depending on gas density. The set-up is discretized with 80 cells in horizontal and 70 cells in vertical direction with a refinement towards the interface.

The soil properties for these set-ups are taken for the same silty soil and the quartz sand as in the previous chapter, where the influence of radiation on evaporation rates is analysed. The values of these properties can be found in the previous chapter in Table 5.1. As sand has a relatively high permeability, momentum transfer controlled by the atmosphere can dominate the flow behaviour in the porous medium, depending on wind velocity. Therefore, a comparison to the silt-type soil can be used to gain valuable information about the transport behaviour when that influence is minor.

Influence of components on evaporation rates

Evaporation rates can be influenced by the presence of components due to changes of the properties of the mixture. Figure 6.7 shows the evaporation rates for two different flow velocities for the sandy soil. One in the turbulent regime and one laminar set-up, with varying initial and boundary concentrations of methane and carbon dioxide.

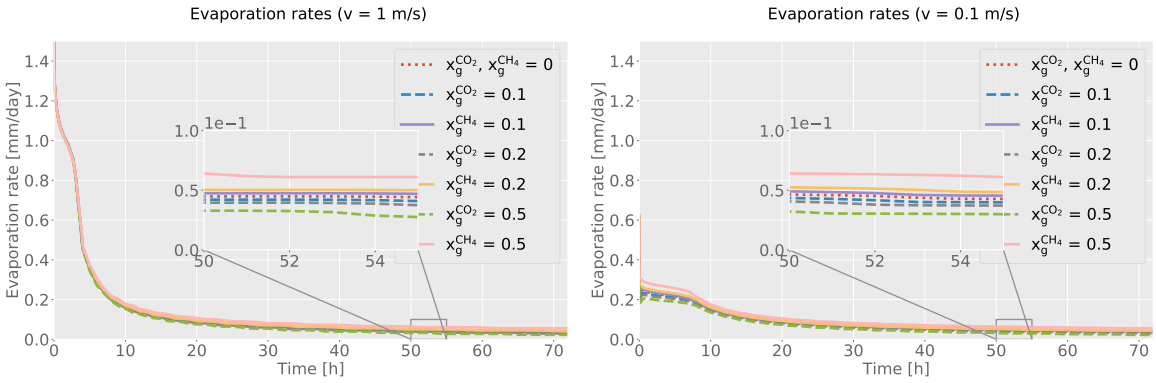

Figure 6.7: Evaporation rates for different free-flow conditions (*left:* turbulent, *right:* laminar) under the presence of different components.

On the left side of Figure 6.7, it can be seen that for a wind velocity of 1 $\mathrm{m\,s^{-1}}$ the evaporation rates drop very fast into stage-II evaporation as capillary forces in the sandy soil are not high enough to supply enough water to satisfy the evaporative demand. The presence of the components does not visibly influence that transition into stage-II evaporation. During stage-I evaporation the transport of water vapour is governed by the free flow. As analysed in the previous section the viscous sublayer thickness does not seem to change substantially with the presence of methane and carbon dioxide, at least with the comparably low concentrations present at the interface. Due to the simultaneous evaporation, temperatures decrease at the interface and water vapour is present in the boundary layer. As evaporation is high, this influence is most likely controlling the boundary layer thickness more than the additional presence of components.

Under stage-II evaporation the results indicate that buoyancy effects in the porous medium affect the evaporation rates. The presence of lighter components leads to enhanced buoyancy, which increases evaporation rates.

Under laminar conditions, which are shown on the right in Figure 6.7, it is visible that the presence of components can also influence the transition to stage-II evaporation. That fits well with the previously conducted single-phase analysis, where it is shown,

that the flow profile in the free-flow can be influenced by the presence of components. Lighter components lead to more evaporation. This can be explained by more mixing in the boundary layer due to lower densities and a thinner boundary layer thickness. The gradient at the interface is greater and this then leads to more transport from the porous medium into the free flow.

The same analysis for silty soil can be found in the appendix in Figure B.2. Conditions of the silty soil are continuously in stage-I evaporation. Therefore, the influence of components is less pronounced for both flow velocities. Still, the same trend is visible: lighter gases lead to higher evaporation rates, which is especially visible for the laminar test case.

Influence of wind velocities on the transport of components during drying

As described before, several studies show that component transport can be heavily influenced by varying wind conditions. The following example analyses the transport of methane and carbon dioxide into the atmosphere combined with evaporation and as a consequence of that drying of the porous medium. Two cases are analysed: (case I) methane is present with a initial mole fraction of 0.1 and (case II) where carbon dioxide is present with the same mole fraction. A dirichlet condition at the bottom of the porous medium leads to a continuous supply of methane (case I), respectively carbon dioxide (case II) as it holds the value for the components at its initial value. For both cases the two different soil types sandy soil and silty soil are analysed.

It is feasible to look at the transport process for two conditions: 1. The transient process where the initially high concentration of methane (case I), respectively carbon dioxide (case II) is transported into the free flow (here, displayed as the transport within the first 10 minutes) and 2. The slower transport when the component is transported from the bottom of the porous medium into the free-flow through the porous medium.

The transport rates displayed in Figure 6.8 show the results for (case I) for silty soil, when methane is the component of interest.

For the first 10 minutes, transport across the interface decreases rapidly, which can be explained with the high concentration gradient in the beginning, due to the initially uniform molar concentration of 10 % methane in the porous medium. Higher flow velocities lead to higher fluxes, which can be explained by the thinner viscous sublayer thickness

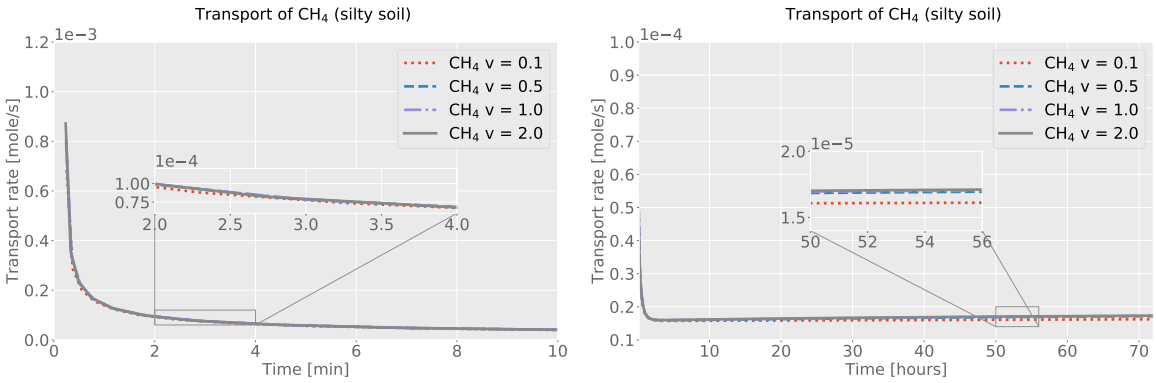

Figure 6.8: Transport of methane across the boundary for silty soil for the first 10 minutes (*left*) and for 70 hours (*right*).

in the free flow, which enhances the gradient and with that also the diffusive flux across the interface. The effect is rather small though, as mostly the diffusion through the porous medium is limiting the transport of methane and not diffusion though the viscous sublayer.

However, the influence of the free flow on methane transport can be seen indirectly, as lower flow velocities lead to a slower drying of the porous medium. The consequence of that slower drying can be observed by analysing the transport of methane for a longer period. After the initial rapid decrease in transport rates, which can be explained by the initial conditions, it can clearly be seen that the transport rates begin to rise. That continuous increase in methane transport over time can be explained by the drying of the porous medium. Decreasing water saturation leads to increasing effective gas diffusion coefficients, which increases the diffusive transport in the porous medium. The slower drying due to lower wind velocities leads to an increasing split in the curves between the different wind conditions.

Carbon dioxide rates (case II) for the silty soil show similar behaviour and are displayed Figure 6.9.

It can be seen that the initial drop in carbon dioxide transport across the interface is comparable to the methane transport and higher wind velocities lead to a faster transport. However, analysing the transport across the interface for a longer time, it is obvious that the curves for all velocities decrease less than for methane. This can be explained by considering that carbon dioxide is more soluble in water than methane. Initially when the gaseous concentration for both components is the same, due to the assumption of

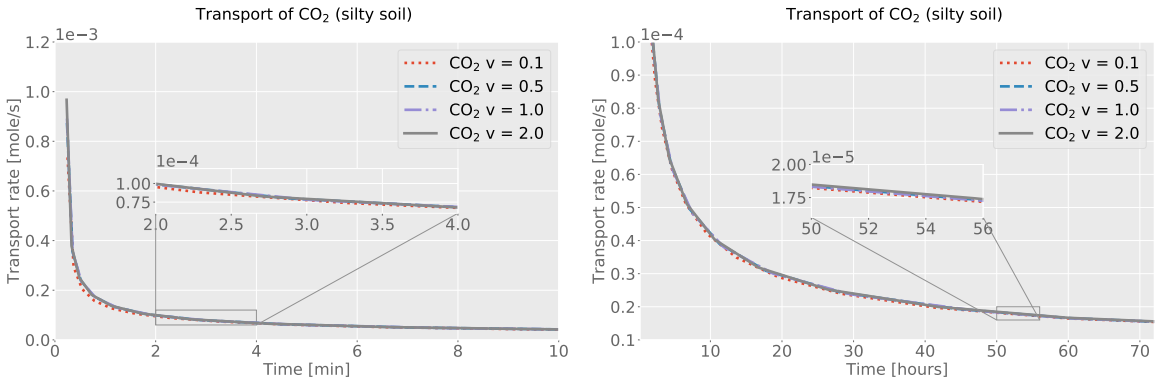

Figure 6.9: Transport of carbon dioxide across the boundary for silty soil.

chemical equilibrium, more carbon dioxide will be present in the water phase and will be released into the gas phase and transported into the atmosphere during drying.

A different result for the different wind velocities can be observed for the sandy soil in Figure 6.10.

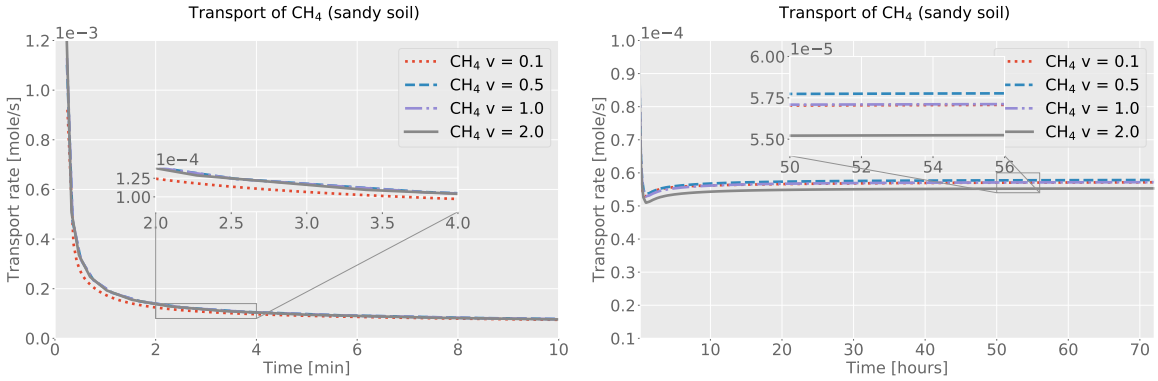

Figure 6.10: Transport of methane across the boundary for sandy soil for the first 10 minutes (*left*) and for 70 hours (*right*).

Initially, for the first 10 minutes on the left in Figure 6.10, the transport rates for sandy soil are similar to these of the silty soil. Higher velocities lead to higher transport rates across the interface, which is most likely due to the different boundary layer thickness. Sandy soil in general has higher transport rates compared to silty soil, which can be explained by considering the effective diffusion coefficients, which are higher, when porosity is higher and water saturation lower. This leads to higher diffusive fluxes in the sandy soil, which also increases the transport across the interface.

After the initial decrease in methane transport in the first 10 minutes, it can be observed on the right of Figure 6.10, that for a longer observation period higher flow velocities

lead to lower transport rates. This cannot be explained by the differences in viscous sublayer thickness influencing the diffusive flux across the interface, which would lead to the opposite result. To analyse this result more closely, in Figure 6.11 the fluxes across the porous medium-free flow interface are displayed for two flow velocities and both soil types for each location at the interface after 72 days of simulated time.

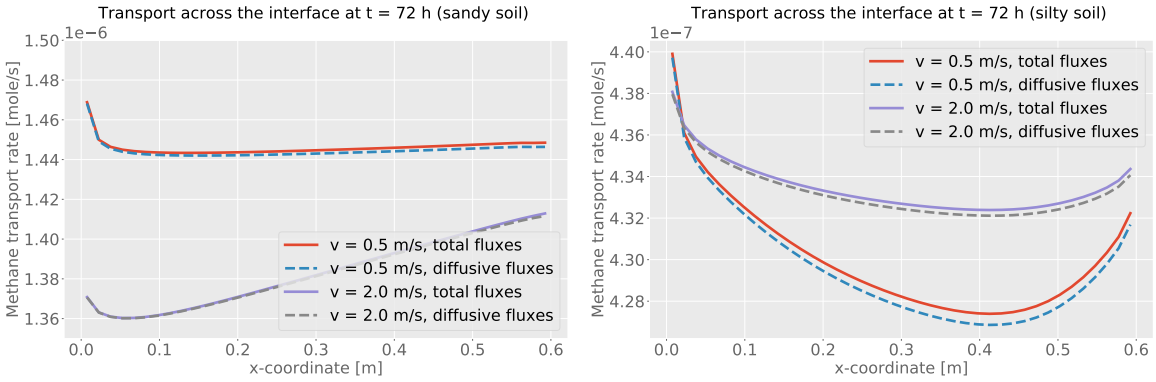

Figure 6.11: Total and diffusive fluxes of methane across the interface after three days for two different flow velocities and two soil types. *Left* for sandy soil and *right* for the silty soil. The x-axis denotes the location at the interface.

Here, it can be observed, that higher velocities, decrease the fluxes for the sandy soil. The forces induced by the higher flow rate at the top act against buoyancy forces in the porous medium, which leads to less transport of methane in the porous medium towards the interface. In this setting higher flow velocities lead to a higher pressure at the interface. The pressure at the bottom of the porous medium is fixed, therefore this change in pressure due to the different flow velocity changes the advective flow in the porous medium as a whole. As the transport rates in general are relatively low, this small changes already have an effect on the whole transport rate.

An additional effect that can decrease methane transport especially in the beginning, is as described in Chapter 2 that higher flow velocities lead to higher evaporation rates under stage-I evaporation, which reduces the temperature at the interface which leads to higher densities. This can also lead to lower methane fluxes. After transition into stage-II evaporation, this effect should not have a high impact on the transport any longer as then evaporation rates are more similar for all velocities.

In Figure 6.11 it can also be observed that on the left side of the domain the transport is high for both velocities, as the concentration of methane in the free flow is lowest. Afterwards, transport rates decrease. For the highest velocity of 2 $\mathrm{m\,s^{-1}}$ it can be

observed that after that initial drop, transport rates increase further downstream, even surpassing the values on the left side. This can be explained by wind induced lateral flux, which is found for a similar sand type also in Bahlmann et al. [2020] and leads to considerable non-uniform fluxes across the interface. However, in Bahlmann et al. [2020] a closed box is investigated, while the current set-up investigates a constant reservoir of methane at the bottom.

For silty soil it can be seen that the influence of momentum transfer is very low. The highest transport rates can be observed on the left side of the domain due to the highest gradient as here methane concentrations in the free flow are lowest. Additionally, it can be seen, that transport rates are higher for faster wind velocities, which can be explained by the reduced boundary layer thickness. The increase in transport at the right side can most likely be attributed to higher temperatures at the right boundary of the domain. Evaporative cooling leads to lower temperatures at the interface. At the left and right side of the domain conduction from the left and right boundary condition mitigates that effect. This also offers an explanation why on the left side of the domain the transport rate is higher for the velocity of 0.5 $\mathrm{m\,s^{-1}}$ than for the velocity of 2 $\mathrm{m\,s^{-1}}$. For a higher flow velocity, more evaporation leads to more evaporative cooling which decreases methane transport due to the decreased diffusion coefficient, which is lower with lower temperatures.

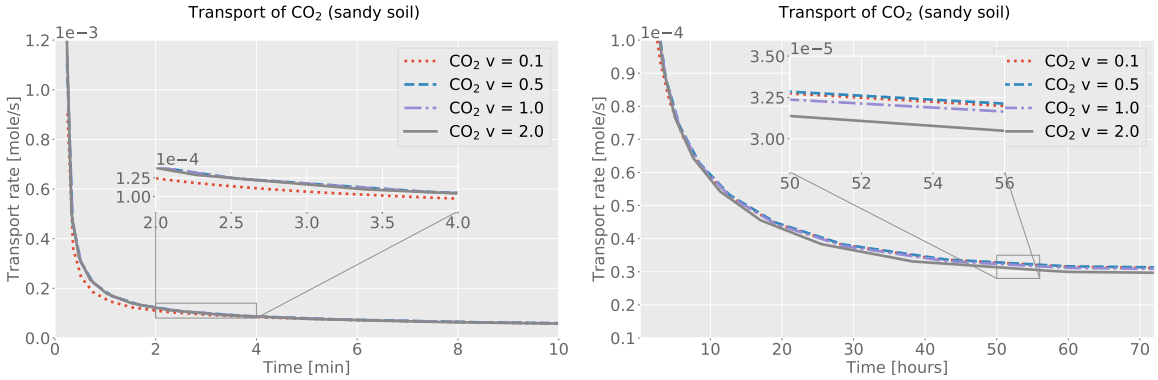

Figure 6.12: Transport of carbon dioxide across the boundary for the first 10 minutes (*left*) and for 70 hours (*right*).

Comparing the transport of carbon dioxide in Figure 6.12 for the sandy soil, the same trends as for methane can be observed, but not as pronounced. Carbon dioxide is heavier, and as shown in Bahlmann et al. [2020] less influenced by the momentum transport. Additionally, carbon dioxide is more soluble in water, therefore the effect of momentum

transport in the gas phase is mitigated as carbon dioxide can also be transported in the water phase.

Discussion of the different diffusion concepts

In this section the differences between Fick's law and the Maxwell-Stefan formulation is evaluated. The same set-up as before is used, with a wind velocity of 1 $\mathrm{m\,s^{-1}}$ and both methane and carbon dioxide initially present in the porous medium ($x_g^{CH_4} = 0.05$, $x_g^{CO_2} = 0.05$)

This comparison aims to analyse how much influence in the fluxes can be attributed to multicomponent diffusion. Fick's law in the implemented version with binary diffusion coefficients predicts the diffusive fluxes if the components only interact with the main component of the phase.

Figure 6.13 shows the fluxes of methane and oxygen over a simulation period of 70 hours for both diffusion formulations for sandy soil as well as for silty soil. It can be observed, that for both soil types, there is no significant difference between the fluxes of methane predicted with the help of both diffusion formulations. Oxygen rates show a higher discrepancy though, which will be further analysed in the following.

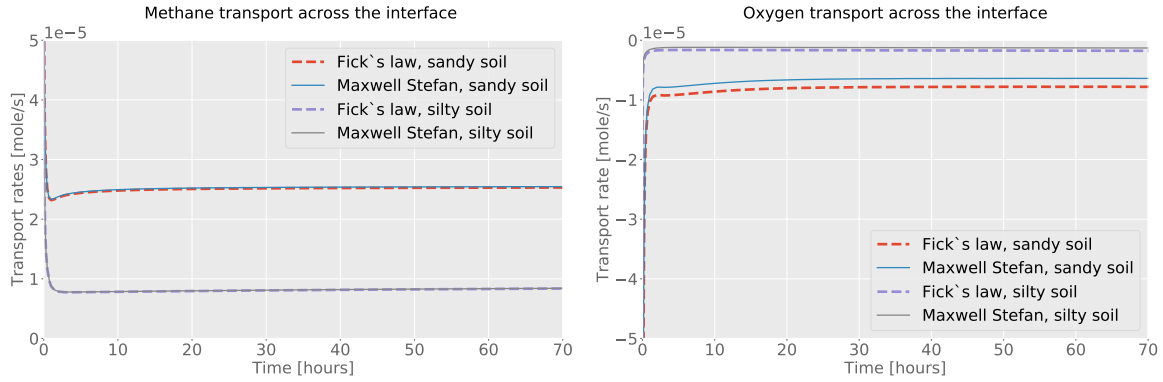

Figure 6.13: Methane and oxygen transport compared for the two approaches to describe diffusive fluxes.

The ratio of fluxes of both diffusion formulations is shown in Figure 6.14. It can be seen that oxygen rates are overestimated with Fick' law while the transport of the other components is slightly underestimated.

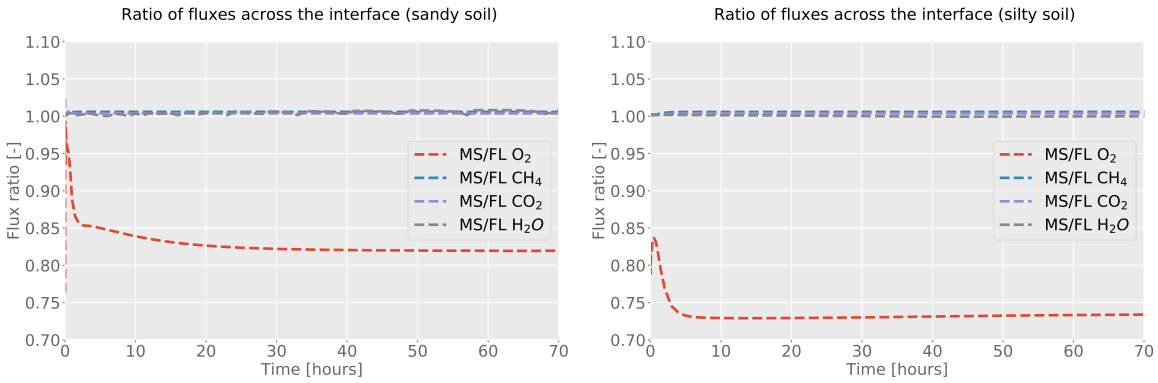

Figure 6.14: The ratio of oxygen, water vapour, methane and carbon dioxide transport for the two different fluxes calculated with Fick's law versus the Maxwell-Stefan formulation.

As previously shown, when the binary diffusion coefficients for all components are not varying greatly it is expected that Fick's law for binary diffusion gives adequate results [Taylor and Krishna, 1993]. For methane, carbon dioxide and water this approximation shows a good agreement with the Maxwell-Stefan formulation. However, in this set-up, oxygen transport rates are very different. In the current setting the concentration gradient of oxygen between the free flow and the porous medium is small, therefore it is not the only dominating driving force. The other components and their gradients can therefore influence the transport of that component more. In the Maxwell-Stefan formulation, the fluxes of all components are considered to calculate the diffusive flux as shown in Chapter 3. Therefore, the high diffusive fluxes of water vapour, methane and carbon dioxide across the interface influence the diffusive flux of oxygen as well. As that influence is not considered in the employed version of Fick's law, that explains the discrepancy between the two formulations.

The difference of predicted oxygen rates for sandy soil is less pronounced than for silty soil, as here the transport is not purely diffusive but also advective transport plays a role, which mitigates the difference between the diffusion formulations.

For sandy soil the evaporation ratio between the two diffusion formulation shows various changes. This can be explained by the drying process in the porous medium. The evaporation rates are already very low and small differences lead to a complete drying in one time step or not, which leads to these bumps. As silt does not dry that fast, this cannot be observed in silt.

In order to evaluate that difference of predicted oxygen rates and put it more in context,

the same set-up is simulated with a closed bottom at the lower boundary of the porous medium assuming a no-flow condition. This means that all sides of the porous medium are closed except for the interface with the free-flow. In this setting the differences in oxygen rates transported from the atmosphere to the porous medium can be evaluated easily as it can be observed how long it takes until the oxygen concentration is equilibrated. This evaluation can be observed in Figure 6.15 where the cumulative oxygen transport across the interface is displayed compared for the two diffusion formulations.

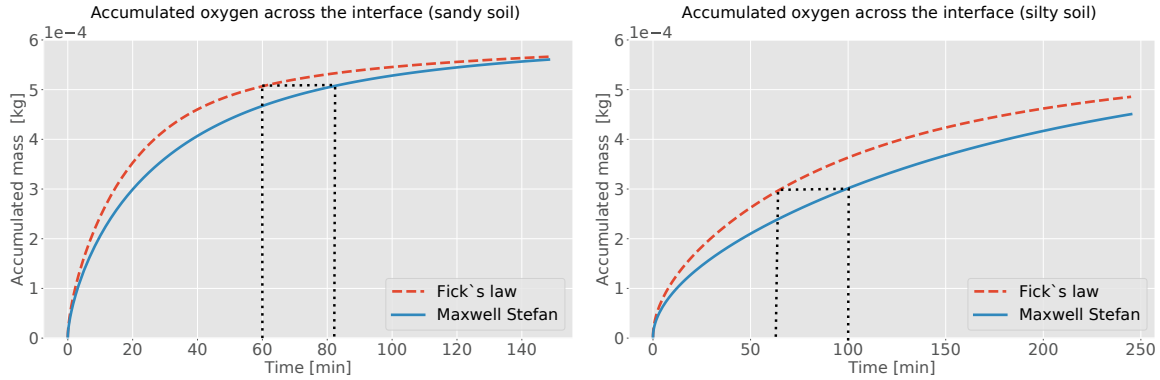

Figure 6.15: Accumulated oxygen transport in the porous medium for sand (*left*) and silt (*right*). The black dotted lines show the difference when a certain accumulated mass is reached with Fick's law compared to the Maxwell-Stefan formulation.

Fick's law clearly predicts a faster transport and therefore equilibration of the concentration of oxygen than the Maxwell-Stefan formulation. In sand, the whole process is faster and differences vanish after a while as transport is not purely diffusive. For silt, the difference in transport persists. The accumulated rates show that in silt in order for the Maxwell-Stefan formulation to predict the same accumulated mass flux into the porous medium that is reached for the Fick's law prediction at around 60 minutes, the Maxwell-Stefan formulation needs 100 minutes.

Influence of surface undulations

As described previously, irregular surface structures can have a very high influence on the exchange process between soil and the atmosphere. The following section analyses that influence more closely.

The set-up consists of a porous medium with one rectangular porous obstacle seen in Figure 6.16. The obstacle will lead to a flow separation in the free flow, where the

boundary layer detaches when reaching the obstacle and reattaches downstream. The length of the detachment zone depends on the height of the obstacle. A similar set-up was investigated in Coltman et al. [2020] for evaporation. There, it is analysed that depending on the obstacle height and shape different flow patterns can emerge in the free flow that have a very high influence on evaporation rates. This section expands the analysis by including the transport of methane and carbon dioxide.

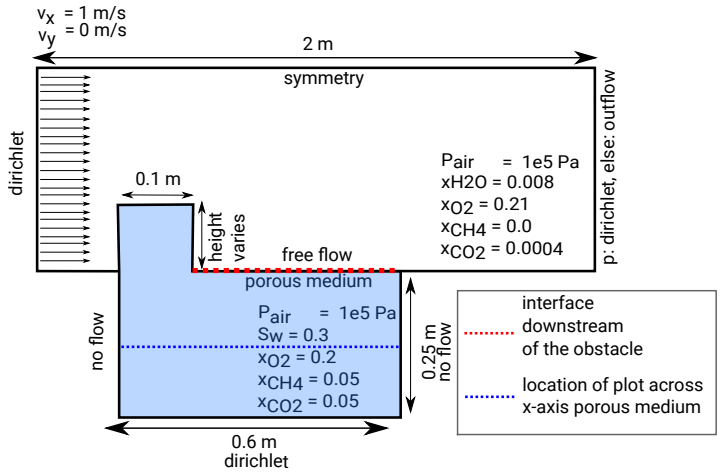

Figure 6.16: Set-up for the analysis of multicomponent transport in a coupled soil-atmosphere system with one porous obstacle at the beginning of the porous medium. The gas pressure in both domains is set with 1 bar pressure at the interface and a hydrostatic distribution in the free flow and the porous medium, depending on gas density. It is discretized with 250 cells in horizontal direction and 75 cells in vertical direction. The blue line indicates the x-axis of the porous medium, over which velocities are plotted in Figure 6.19 and the red line the interface after the obstacle, where the fluxes across the interface are compared in Figure 6.17 and 6.18.

Two soil types are compared to evaluate different flow regimes. As analysed before, the hydraulic properties of the silty soil lead to a continuous supply of water, holding evaporation rates in stage-I evaporation due to the given boundary conditions with a dirichlet condition at the bottom. In contrast, the sandy soil dries rather quickly and momentum transport from the free-flow into the porous medium has a higher impact on the transport of the components.

Figure 6.17 shows the water vapour concentration in the free flow and the water saturation in porous medium after 1 hour. The recirculation zone, developing after the obstacle can be seen. Additionally, the corner eddy, right after the obstacle is visible. This eddy is disconnected from the main stream, leading to an accumulation of water vapour, carbon dioxide and methane in the corner.

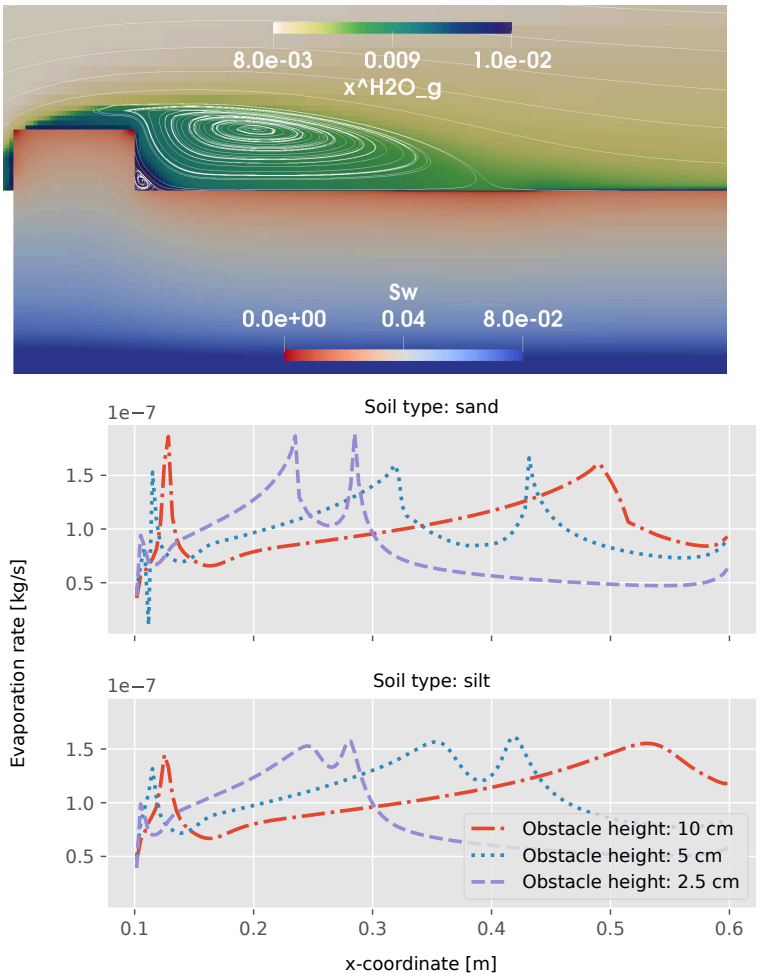

Figure 6.17: *Upper part:* Water vapour concentration in the atmosphere after 1 hour of drying and water saturation in the porous medium. The development of the recirculation zone and the corner eddy is visible in the free flow. In the corner eddy, water vapour concentrations are high as the eddy is disconnected from the main flow. *Lower part:* Evaporation rates for both soil types and varying height of the obstacle across the interface downstream of the porous obstacle (red line in Figure 6.16). The x-axis describes the x-position of the interface. The analysis starts after 10 cm, which is right after the obstacle.

In the lower part of Figure 6.17 the evaporation rates downstream of the obstacle for both soil types and varying height of the obstacle (2.5 cm, 5 cm, and 10 cm) is shown. The shape that develops is very similar as described in Coltman et al. [2020]. Water saturation are initially lower, therefore some additional effects due to local drying processes can be observed. Evaporation rates are lower beneath the corner eddy, as the exchange with the main flow is limited. The local maximum can be attributed to additional diffusive mixing in the eddy. In the larger recirculation zone that follows, evaporation rates rise

further until a steep drop in evaporation rates visible in the sandy soil. This drop can be explained by a local drying of the sand, where evaporation rates are already in stage-II evaporation. It is located at the end of the recirculation zone, where the drying during stage-I evaporation is highest, due to the recirculation of the drier atmospheric air. This is also visible in the upper part of Figure 6.17, where saturation are lowest at the end of the recirculation zone.

Evaporation rates of the silty soil are continuously in stage-I evaporation, which can be seen in the lower part of Figure 6.17. Nevertheless, a small decrease in evaporation rates is visible at the end of the recirculation zone. Here, water saturation are lowest and capillary pressures are high, leading to a decrease in vapour pressure according to the Kelvin equation (see Chapter 2.3.5), which lowers evaporation rates.

In Figure 6.18 the methane concentration in the porous medium is displayed. It can be observed, that the wind induces transport in the soil that pushes methane towards the right, increasing the concentrations downstream of the obstacle.

In the lower part of Figure 6.18 it can be observed, that the eddy development in the free-flow is not the dominating process that governs the shape of the transport curve. Instead, the transport rates are highest right after the obstacle and decrease along the recirculation zone. This is especially visible for the sand type soil.

Analysing the velocity in x-direction in the porous medium for the sandy soil in Figure 6.19 shows, that for higher obstacles, the velocity increases in the porous medium, which explains the shape of the transport rates. Higher obstacles lead to more momentum transfer in the soil. As explained before, this is already visible in Figure 6.18. For silty soil the momentum transfer is much lower, which explains the flatter curve of the transport rates. A local maximum can be seen in the curves for silty soil at the end of the recirculation zone, where fresh air is provided, which enhances the gradient and thus the transport.

It can also be observed that once the viscous sublayer reattaches, the transport rates are very similar again, as can be seen for sandy soil 50 cm downstream of the obstacle. Here, the viscous sublayer reattaches for the 5 cm high obstacle as well, which leads to transport rates very similar as for the 2.5 cm high obstacle. This shows the flow induced by the flow around the obstacle and the length of the recirculation zone have a very high influence on the transport of gaseous components.

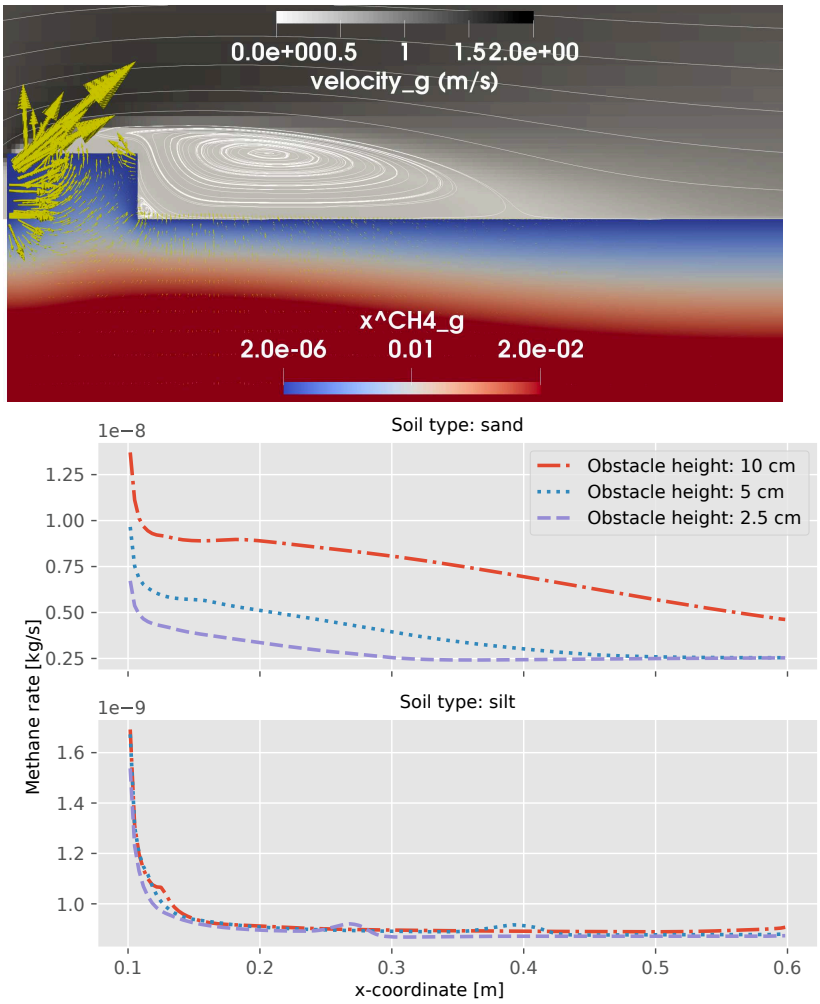

Figure 6.18: *Upper part:* Methane concentration in the soil and the atmosphere after one hour for a obstacle height of 5 cm. *Lower part:* Methane rates downstream of the porous obstacle across the interface (red line in Figure 6.16) with varying obstacle height.

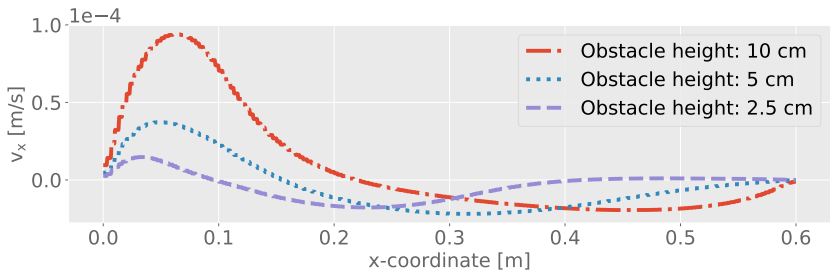

Figure 6.19: Velocity in x-direction across the x-axis in the porous medium (blue line in Figure 6.16).

6.1.3 Summary

This process analysis shows that multicomponent transport in coupled porous-medium free-flow systems are influenced by various different fluid properties and flow dynamics. The properties of the component itself show a high influence on the transport behaviour: (I) Different densities lead to different buoyancy effects, dependent on the boundary layer thickness. Moreover, different densities can lead to more or less momentum transfer in the porous medium, which exceed the influence densities have on boundary layer thickness or viscous sublayer thickness. (II) Viscosities influence the momentum transport as well, with lower viscosities enhancing the transfer.

The influence of different wind velocities in the free flow is analysed and it is shown, that although higher wind velocities lead to a faster drying, which enhances the diffusive transport of the components, and faster free-flow velocities lead to thinner viscous sublayers, still for a certain set-up increasing wind velocities lead to lower transport rates. The reason for that is found to be the higher momentum transfer that occurs with higher flow velocities, that acts against buoyancy forces. This is especially pronounced for methane compared to carbon dioxide. Methane has a low density and low viscosity making mixtures with a high methane content sensitive to wind induced fluxes in the porous medium. A comparison between turbulent and laminar flow shows that laminar boundary layers can be disturbed by the presence of components with different densities even leading to a detachment of the boundary layer. Under turbulent flow, the flow behaviour is not changed visibly.

Evaporation rates are mostly influenced by the presence of components under stage-II evaporation, where evaporation is limited by the transport in the porous medium. Then the different densities of the components show an influence on evaporation rates. Under stage-I evaporation, changes in evaporation rates due to the presence of components can only be seen for the laminar case, which agrees well with the before mentioned effect on the flow profile in the free flow under laminar conditions.

An analysis of the influence of multicomponent diffusion processes shows that the transport of methane, carbon dioxide and water vapour from the porous medium into the free flow is well represented by a Fickian diffusion approximation, where only binary diffusion is considered. The transport of oxygen into the porous medium in such a setting is overestimated when assuming that the other components do not have an influence on the

transport of oxygen. When surface obstacles are included, it can be seen that again momentum transfer from free flow into the soil influences the transport significantly. Higher obstacles lead to more momentum transfer from the free flow into the porous medium, which enhances transport of the components downstream of the obstacle. This is in contrast to the behaviour of water vapour as long as evaporation is in stage-I evaporation. Then the eddies developing in the free-flow dominate the shape of the evaporation curves.

6.2 Benchmark study: multicomponent transport [2]

This benchmark study was conducted in cooperation with Technical University of Denmark (DTU) to compare two implementations of a coupled porous-medium free-flow system. Two different software tools are used throughout the study: COMSOL Multiphysics® (version 5.4), where a one-domain approach using Brinkman's equation is implemented and DuMu^x where the two domain approach as described before is used. Both systems use the Maxwell-Stefan formulation to describe multicomponent diffusion. In both codes grid refinement was performed until the solution did not vary any more.

The examples are structured in a manner of increasing complexity. First, a porous medium with two components is analysed, highlighting the difference between mass and molar formulation of the diffusion laws, then a three component porous media system is presented, and in the last two examples a coupled porous-medium free-flow system is compared.

To decrease the problem complexity, for this study constant viscosities of the pure components and constant diffusion coefficients are assumed, which can be seen in Tables B.3 and B.4 in the appendix.

6.2.1 Diffusion of two components in a porous medium

This example highlights the differences between the mass reference system and the molar reference system, for which diffusive fluxes can be formulated. It is presented in Fen and

[2]The following section is also presented in a longer version in: Ahmadi, N., Heck, K., Rolle, M. et al. On multicomponent gas diffusion and coupling concepts for porous media and free flow: a benchmark study. Computational Geosciences (2021) https://doi.org/10.1007/s10596-021-10057-y [Ahmadi et al., 2021].

Abriola [2004] for Fick's law. Here, a comparison with Fick's law for a molar reference system and the Maxwell-Stefan formulation for a mass reference system is presented, compared to the solution presented by Fen and Abriola [2004].

The domain is set up as a 1-D column, where initially nitrogen is present and methane migrates from the right boundary into the porous media domain. The pressure is kept constant at the boundaries. Figure 6.20 shows the domain with necessary information about initial conditions and spatial parameters.

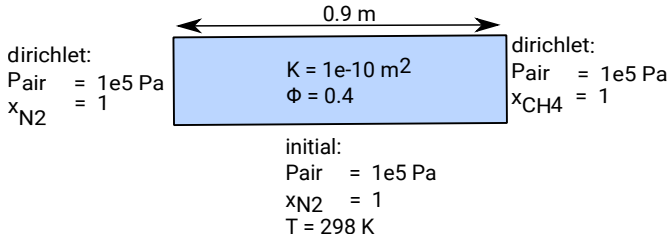

Figure 6.20: Set-up of the first benchmark example analysing multicomponent transport in a porous medium. The set-up is a 1-D column, only extruded in the sketch for better visualisation.

For the computation of the effective diffusion coefficient a constant tortuosity is assumed, which is set to 0.735. Figure 6.21 shows the comparison for the two different software frameworks after 100 and 500 minutes.

It can be observed that both simulation tools show a very good agreement with the data presented in Fen and Abriola [2004]. The difference between the diffusion laws presented in a mass reference system and a molar reference system is very visible in this set-up. Only when the average molar mass of the components are equal, the predicted fluxes in this set-up would be the same. As methane is lighter than nitrogen, here, it can be observed that both formulations lead to different results. In the mass reference system the different densities lead to an additional advective mass flux, induced by diffusion. In the molar reference system, the bulk velocity is zero.

6.2.2 Diffusion of three components in a porous medium

This example demonstrates that in multicomponent systems the Maxwell-Stefan formulation can show a different behaviour than what Fick's law predicts. The set-up consists of a porous medium with closed walls, where one half is filled with gas with a specific

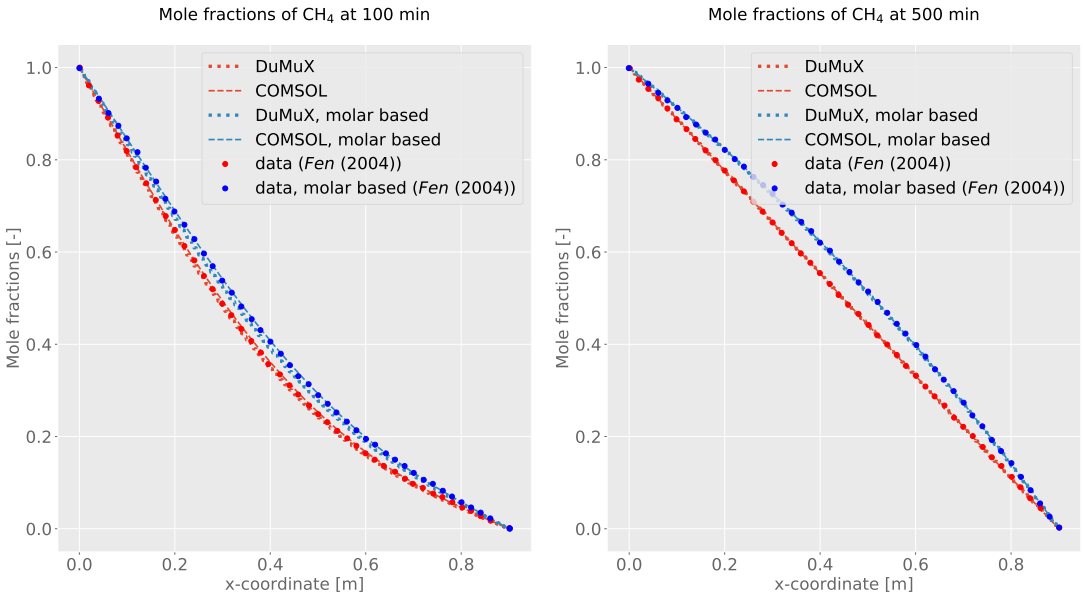

Figure 6.21: Comparison of Fick's law in the molar reference system and the Maxwell-Stefan formulation in a mass reference system for a two component set-up. (Reprinted by permission from Springer Nature Customer Service Centre GmbH: Springer Nature, Computational Geosciences, On multicomponent gas diffusion and coupling concepts for porous media and free flow: a benchmark study, Navid Ahmadi et al, Copyright (2021))

composition and the other half is filled with a different composition. This set-up can be seen in Figure 6.22.

The permeability is assumed to be $K = 2 \cdot 10^{-10}$ m^2, the porosity $\phi = 0.4$, the initial pressure is $p_g = 1 \cdot 10^5$ Pa, and the temperature $T = 308$ K. The set-up is a variation for a porous medium designed after an experiment with the same gas mixture in two glass bulbs by Duncan and Toor [1962]. In Krishna and Wesselingh [1997] it is shown, that the Maxwell-Stefan formulation is able to capture the behaviour of the three components adequately.

Figure 6.22 shows the mole fraction in the left and right half of the domain for the three components over time. Additionally, the mole fraction of nitrogen across the x-axis is displayed for different points in time.

While carbon dioxide and hydrogen show a diffusive behaviour as expected, nitrogen shows a very different behaviour. Here, three different stages can be distinguished: At first, nitrogen diffuses against the concentration gradient (uphill diffusion), which leads to a further decrease of nitrogen in the left half and an additional enrichment in the

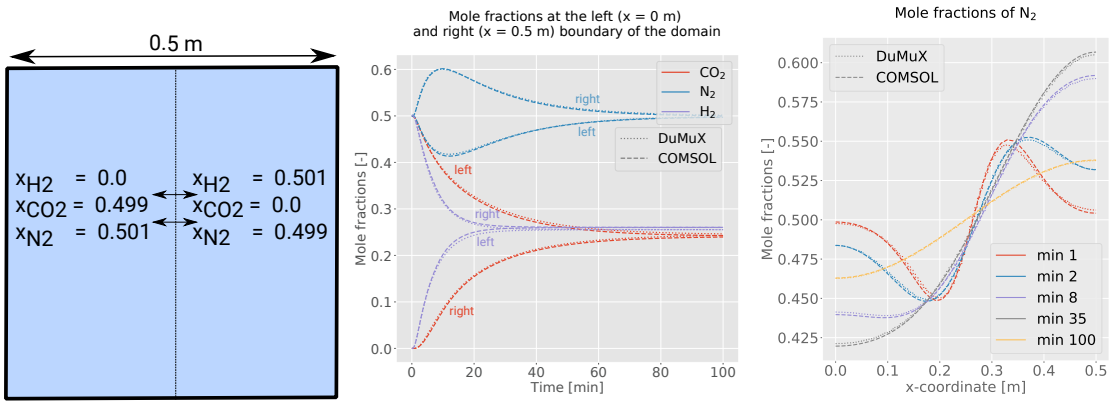

Figure 6.22: Comparison of DuMu^x and COMSOL Multiphysics® for a porous medium set-up with three components. *Left:* Set-up of the second benchmark example. *Middle:* Mole fractions for the left and right half of the domain over time for the three components for DuMu^x and COMSOL®. *Right:* Mole fraction of nitrogen over the x-axis at 0.25 m for five different points in time. (Reprinted by permission from Springer Nature Customer Service Centre GmbH: Springer Nature, Computational Geosciences, On multicomponent gas diffusion and coupling concepts for porous media and free flow: a benchmark study, Navid Ahmadi et al, Copyright (2021))

right half of the domain. Then, after around 10 minutes, diffusion reaches a plateau, and no diffusion happens, although the gradient is relatively high (diffusion barrier). Afterwards, the transport is along the gradient in mole fractions until the differences in concentrations between the two halves of the domain vanish. This behaviour is analysed in more detail in Krishna and Wesselingh [e.g. 1997]. The ternary mixture behaviour is more complex than in a binary system. The binary diffusion coefficients for the system are very different ($D_{CO_2,N_2} = 1.68 \cdot 10^{-5}$ m^2 s^{-1}, $D_{H_2,N_2} = 8.33 \cdot 10^{-5}$ m^2 s^{-1}, $D_{H_2,CO_2} = 6.8 \cdot 10^{-5}$ m^2 s^{-1}) and as explained in Chapter 3.1.2 then the influence of multicomponent diffusion is higher.

6.2.3 Flow and transport in a coupled porous-medium free-flow system

The following example describes a set-up of a coupled porous-medium free-flow system. The set-up is inspired by experiments for landfill covers, where methane and carbon dioxide migration is investigated. A column is filled with gravel and in a headspace above, air is circulated. An inlet and outlet at the top provide fresh air. Different flow velocities are analysed, but overall the flow is always laminar.

Initially, the column is filled with a gas mixture with an oxygen concentration of 21 % and a nitrogen concentration of 79 %. Figure 6.23 shows the set-up for the first analysis. Here, the focus is on a comparison of a Fickian description of diffusion and the Maxwell-Stefan formulation.

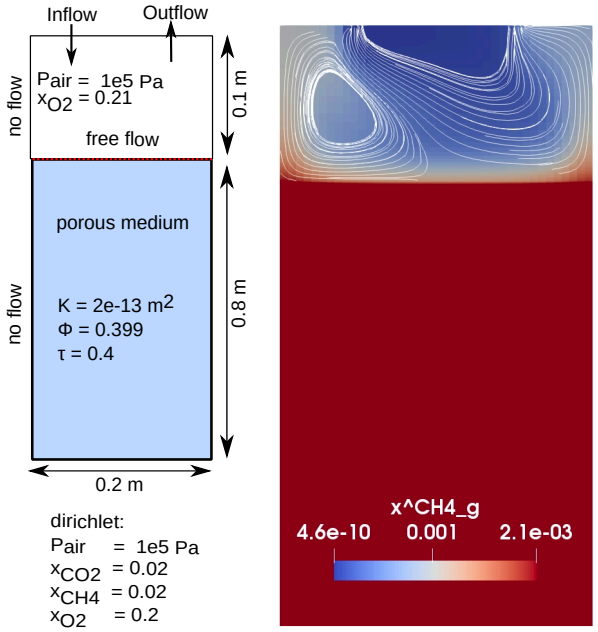

Figure 6.23: *Left:* Set-up of the coupled benchmark example. *Right:* mole fraction in the free flow and porous medium after 20 hours for an injection rate at the top of 109 ml/min. The flow is injected at the inlet at the top and separates towards the interface, leading to the development of an eddy at the left corner.

Figure 6.24 and 6.25 show the fluxes across the interface for methane, carbon dioxide and oxygen for an injection rate of air in the head space of 0.1 mL/min and 109 mL/min. In both cases methane and carbon dioxide migrate through the porous medium and into the headspace. After some time a steady state is reached and the transport reaches a plateau.

It can be observed, that for the low flow velocity at the top, the steady state flow in carbon dioxide and methane is reached more slowly. While for the top flow rate of 109 mL/min after 10 hours the transport rates do not change substantially anymore, for the lower top flow velocity, the transport rates are still increasing. This can be explained by the different gradient that establishes between the porous medium and the free flow, when less methane and carbon dioxide are removed from the interface due to the lower free-flow velocity.

Additionally, it can be observed that for methane and carbon dioxide Fick's law and

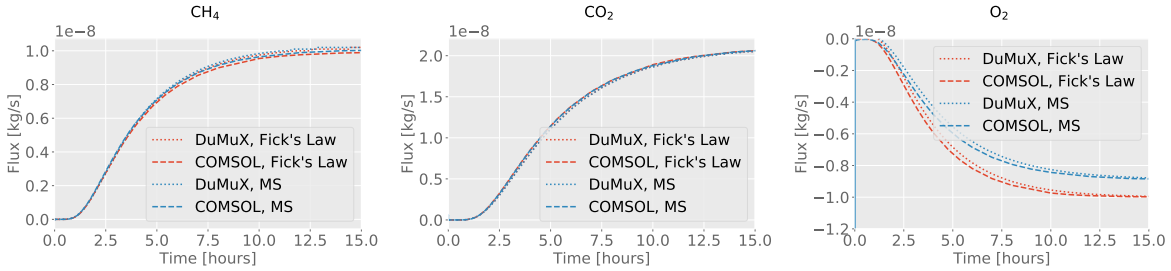

Figure 6.24: Comparison of fluxes across the interface for DuMu^x and COMSOL Multiphysics® in a coupled porous medium free flow set-up for a top flow injection rate of 0.1 ml/min of fresh air. (Reprinted by permission from Springer Nature Customer Service Centre GmbH: Springer Nature, Computational Geosciences, On multicomponent gas diffusion and coupling concepts for porous media and free flow: a benchmark study, Navid Ahmadi et al, Copyright (2021))

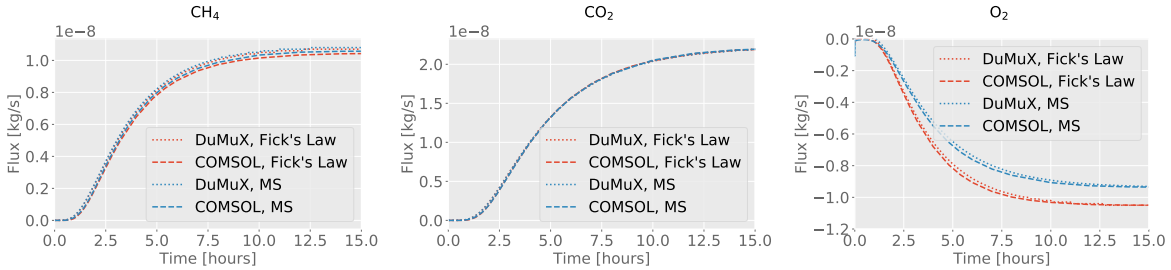

Figure 6.25: Comparison of fluxes across the interface of DuMu^x and COMSOL Multiphysics® for a top flow injection rate of 109 ml/min of fresh air. (Reprinted by permission from Springer Nature Customer Service Centre GmbH: Springer Nature, Computational Geosciences, On multicomponent gas diffusion and coupling concepts for porous media and free flow: a benchmark study, Navid Ahmadi et al, Copyright (2021))

the Maxwell-Stefan formulation predict nearly the same transport rates. For oxygen the transport across the interface into the porous medium is very different though. Here, multicomponent effects seem to influence the diffusive behaviour, which agrees well with the findings in Section 6.1.2, where this was shown also in a two-phase set-up.

The last example uses the same set-up as before with the variation, that here, no dirichlet boundary condition is assumed at the bottom, but a mixture of methane gas ($x_g^{CH_4} = 0.05$) is injected with a flow rate of 5 mL/min and 50 mL/min. The set-up is compared to experimental data obtained in Thomasen et al. [2019]. The top flow rate in this comparison is 109 mL/min. Results for both codes can be seen in Figure 6.26, where mole fractions of methane and oxygen are compared to the experimental data.

For the lower flow bottom flow rate of 5 mL/min, the transport within the porous medium

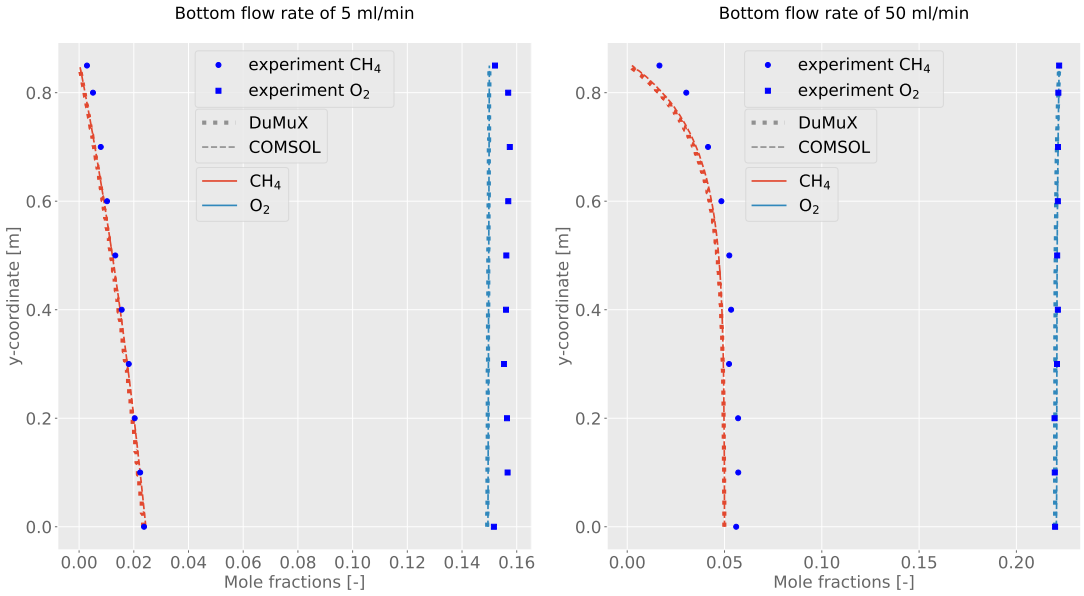

Figure 6.26: Comparison of methane and oxygen mole fractions along the column for DuMu^x and COMSOL® for top flow 109 ml/min and bottom 5 ml/min (*left*) and 50 ml/min (*right*). Experimental data is taken from Thomasen et al. [2019]. (Reprinted by permission from Springer Nature Customer Service Centre GmbH: Springer Nature, Computational Geosciences, On multicomponent gas diffusion and coupling concepts for porous media and free flow: a benchmark study, Navid Ahmadi et al, Copyright (2021))

is more diffusion dominated as can be seen at the more linear profile compared to the profile with a bottom flow rate of 50 mL/min.

Both simulation frameworks show a very good match for all the coupled porous-medium free-flow set-ups.

6.2.4 Summary

The benchmark study shows that both simulation frameworks produce very comparable results and agree well with presented data in other sources or experiments. One example demonstrates the unusual behaviour that can occur in the transport of multicomponent mixtures, leading to diffusion against the gradient of concentration. The coupled porous-medium free-flow examples analyse the transport under different flow conditions in the free-flow and the porous medium. A comparison with Fick's law shows that also in the dry set-up, same as in the previously analysed multiphase set-up, the diffusive flux of oxygen from the atmosphere in the porous medium where oxygen concentration is lower,

differs for the two diffusion formulations. Both simulation tools show a very good match when comparing fluxes across the interface for the various components. A comparison between a more diffusive set-up and a set-up where advection in the porous medium is dominating also shows, that both codes describe the transport process adequately under both conditions. A comparison with experimental data shows a good match for both cases.

7 Results and discussion III - Multicomponent transport and solar radiation

The following evaluations combine the analysis of the transport of multiple gaseous components with the investigation of the influence of radiation. The set-up is similar to the set-ups investigated before and starts first with a flat porous medium which can be seen in Figure 7.1. A diurnal cycle of solar irradiance is considered to evaluate the transport at different times of the day.

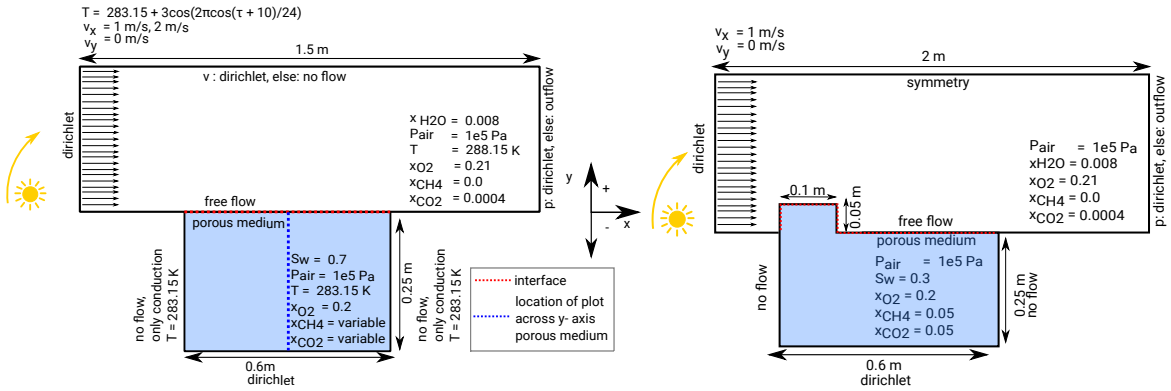

Figure 7.1: *Left:* Set-up for the analysis of multicomponent transport under the influence of radiation. The set-up is discretized with 80 cells in horizontal direction an 60 in vertical direction a refinement towards the interface. *Right:* Set-up for the analysis of the influence of a porous obstacle, analysed in the last section. The gas pressure in both domains is set with 1 bar pressure at the interface and a hydrostatic distribution in the free flow and the porous medium, depending on gas density. It is discretized with 250 cells in horizontal direction and 75 cells in vertical direction.

The investigated soil types are the silty soil type and the sandy soil type as analysed as well in the previous chapters. The relevant parameters for the soils can be found in Table 5.1.

The last section evaluates a set-up with one porous obstacle as described in the previous section for multicomponent transport but with a diurnal cycle of radiation where the sun rises on the left side of the obstacle and sets on the right. The set-up can also be seen in Figure 7.1.

7.1 Influence of soil types

In this section it is analysed how the transport of methane in different soil types is influenced by radiation and a diurnal cycle of evaporation.

Figure 7.2 shows the accumulated mass of methane transported across the interface in a time span of five days. On the left the rates for a sandy soil are displayed and on the right the ones for silty soil. One simulation shows the influence of radiation, while the other radiation is neglected.

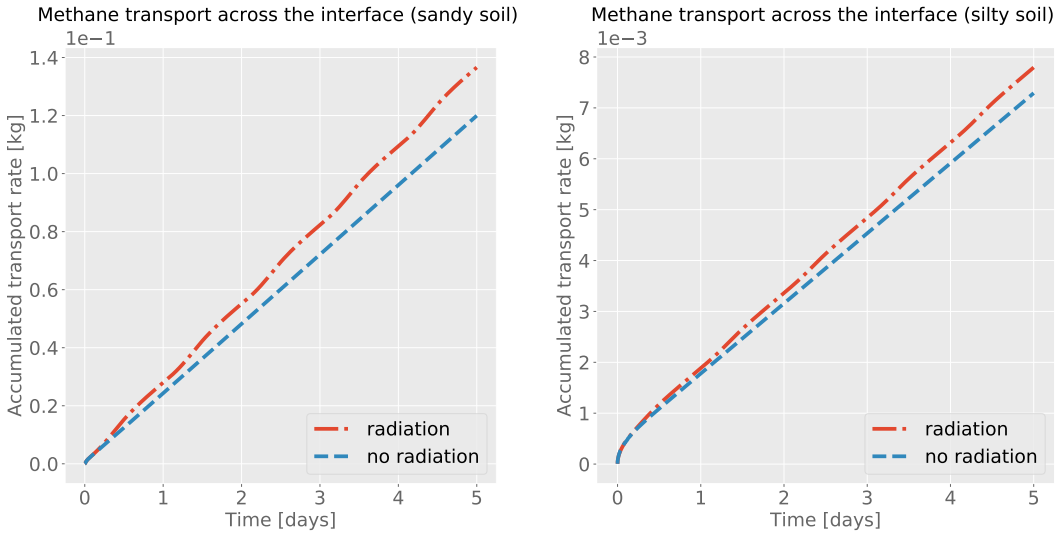

Figure 7.2: Accumulated transport across the interface for one simulation with and one without radiation for sandy soil (*left*) and silty soil (*right*).

It is obvious, that after the initial increase in methane transport, which can be explained by the initial conditions, without radiation the transport rates rise nearly linearly. When a diurnal cycle of radiation is included, the behaviour is non-linear, as the transport also exhibits a diurnal cycle.

In sandy soil the difference between the two cases is much higher than for silty soil. One reason for that is that silty soil is still in stage-I evaporation and therefore surface temperatures do not rise as much as for the sandy soil. Therefore, the influence of the temperature change is more pronounced for the sandy soil than for silty soil. Additionally, in sandy soil, the effects of buoyancy and changes in advective transport parameters have a greater influence. The diurnal cycle of radiation leads to density differences in the porous medium that can change the flow behaviour and lead to additional advective transport. In Figure 7.3 the transport across the interface split into total and diffusive transport can be seen.

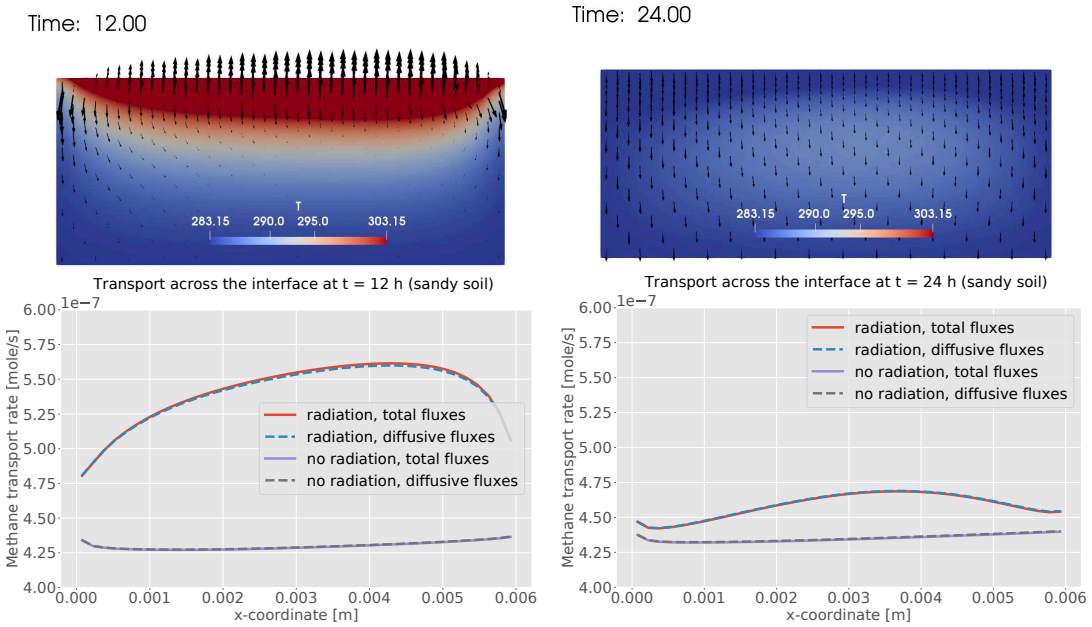

Figure 7.3: Transport across the interface at midday (*left*) and at midnight (*right*). In the upper part, the temperature in the porous medium to that times is displayed. The arrows indicate the flow direction.

It is visible that for the case where radiation is included as well as for the case without radiation, the transport across the interface is mostly diffusive. Still, at midday the transport is strongly enhanced by the solar irradiation, which can be explained by the higher temperatures in the porous medium that can be seen in the upper part of Figure 7.3.

The shift in the curve towards the right boundary can be explained by temperature differences between the left and the right side of the interface. On the left side more the arriving air from the atmosphere is cooler and evaporation rates are highest as the air is very dry. This leads to more enhanced evaporative cooling and conductive heat

exchange, lowering the temperatures. The drop in transport rates at the sides can be explained by the boundary conditions as conductive heat exchange at the left and right side of the porous medium leads to cooler temperatures.

It can be observed that even at midnight, transport rates of methane are still higher than in the case where radiation is neglected. The temperature in the soil is still higher, which leads to higher diffusive fluxes as well as higher advective fluxes due to buoyancy effects. This was also found experimentally for high permeability soils in Ganot et al. [2014].

To analyse that differences between day and night further, Figure 7.4 shows the concentration of methane, the density of the gas phase, and the temperature in the porous medium plotted across the y-axis of the porous tank for 4 different times during a day.

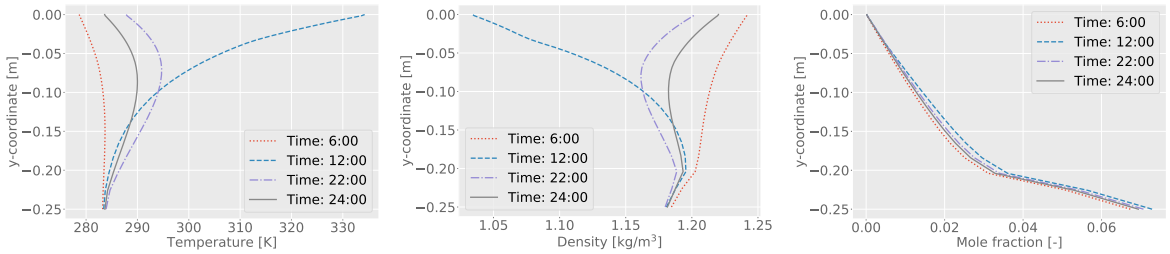

Figure 7.4: Temperature (*left*), density (*middle*), and mole fraction of methane (*right*) across the y-axis (blue line in Figure 7.1) in the porous medium for four different times during a diurnal cycle of radiation.

It can be observed that during the night (at 10 p.m and at midnight) the temperatures are still elevated in the porous medium although they decrease towards the interface due to the evaporative cooling. This higher temperature in the porous medium leads to non-linear density distributions: At the bottom of the porous medium the density is controlled by the dirichlet boundary, that fixes the methane content as well as the temperature. As the methane content decreases towards the top, the density should increase due to changes in composition. As the temperature increases though, the density is dominated by that temperature change and instead densities decrease further. At the interface due to evaporative cooling temperatures are lower again, which leads to a subsequent increase in density.

At six in the morning this higher temperature lens in the porous medium is not visible any longer, the temperature decreases from the bottom to the top of the porous medium due to the lower temperature at the top. During the day, the temperature increases tremendously (here visible at midday) and the density decreases drastically. These changes

in temperature and its influence on the transport process is also reflected in the mole fractions, plotted on the right.

7.2 Influence of different components

The influence of different components can be seen in Figure 7.5 for methane and carbon dioxide, where the fluxes of each component across the interface of an unsaturated sandy soil into the atmosphere can be observed for a time period of five days.

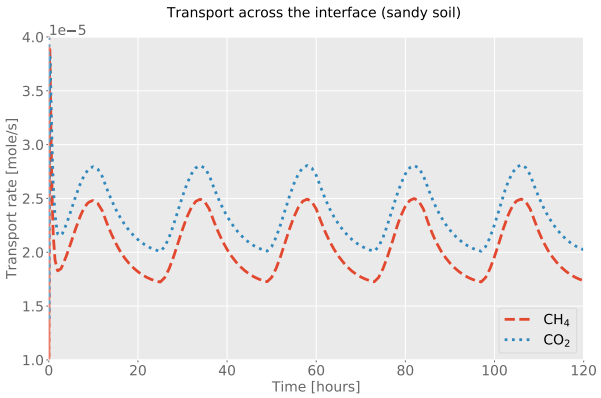

Figure 7.5: Transport across the interface for carbon dioxide and methane.

Both components show a very similar behaviour. The temperature due to solar radiation leads to a decrease of density independent of the component, because both are treated as ideal gases.

However, it can be seen that in this set-up more carbon dioxide is released into the atmosphere than methane. This is in contrast to the previous analysis in a dry set-up and with low water saturation analysed in Chapter 6.

In the current set-up the water saturation at the bottom of the porous medium is relatively high due to the dirichlet boundary condition. Therefore, diffusion in the gas phase is limited. That is why in the current set-up the transport in the liquid phase plays a more dominant role. As carbon dioxide is much more soluble in the liquid phase than methane, this explains the higher transport rates.

This can also be seen in Figure 7.6, where the mole fraction in the gas phase and in the liquid phase is shown at midday and midnight. For both components mole fractions in the gas phase are higher at midday than at midnight. For the liquid phase, the mole

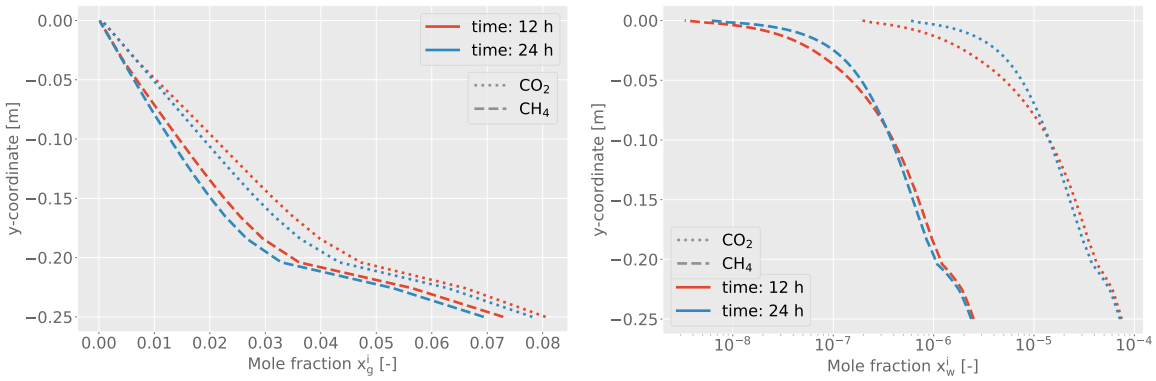

Figure 7.6: *Left:* Mole fraction of carbon dioxide and methane at midday and midnight in the gas phase. *Right:* Mole fraction of the components in the liquid phase.

fractions at the interface are much lower at midday than at midnight which can be explained by the lower solubility when temperatures are higher.

7.3 Influence of free-flow velocity

As previously analysed, different wind velocities influence the transport of the components. At the same time, temperature changes in the porous medium are influenced by radiation and evaporation. As different wind velocities lead to different evaporation rates, a diurnal cycle of radiation can induce different temperature gradients in the porous medium depending on wind speed. This then can change the behaviour of the components. This is analysed in Figure 7.7 that shows evaporation rates for both soil types over the course of five days for two different turbulent wind speeds.

The silty soil is continuously in stage-I evaporation and as seen before as well, evaporation rates are higher for higher wind speeds due to the thinner boundary layer thickness and more mixing. This leads to more evaporative cooling and lower temperatures (Figure 7.8). Additionally, this results in dryer soil, which increases the effective diffusion coefficients of the gaseous components. The transport rates of methane are then greater for the higher wind speeds, which can be seen in Figure 7.9. The difference is small though and transport rates are low in general for both velocities.

The sandy soil is in stage-II evaporation from the beginning. Here, higher wind speeds result in lower peak evaporation rates. As can be seen in Figure 7.8, peak surface

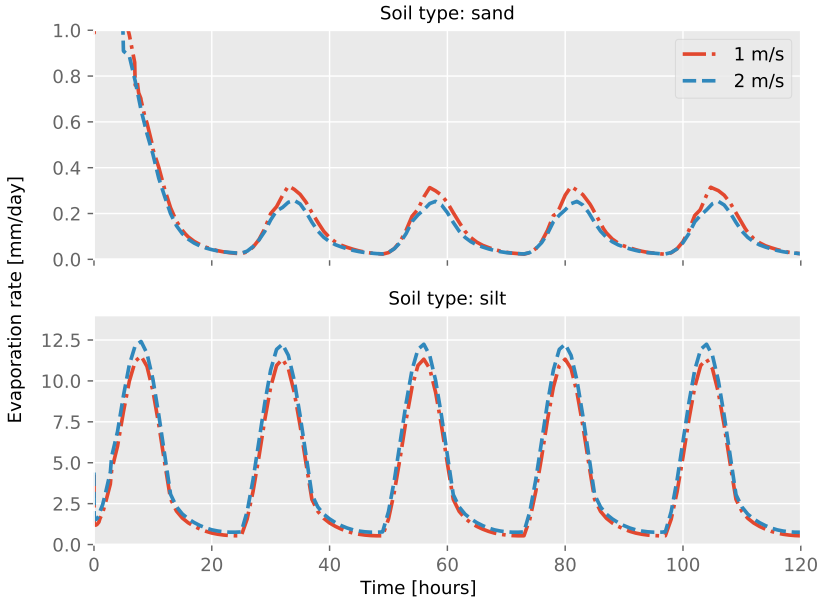

Figure 7.7: Evaporation rates depending on soil type and velocity over five days.

temperatures are lower for higher wind speed. This can be attributed to more conductive cooling with the cooler atmosphere due to the thinner boundary layer.

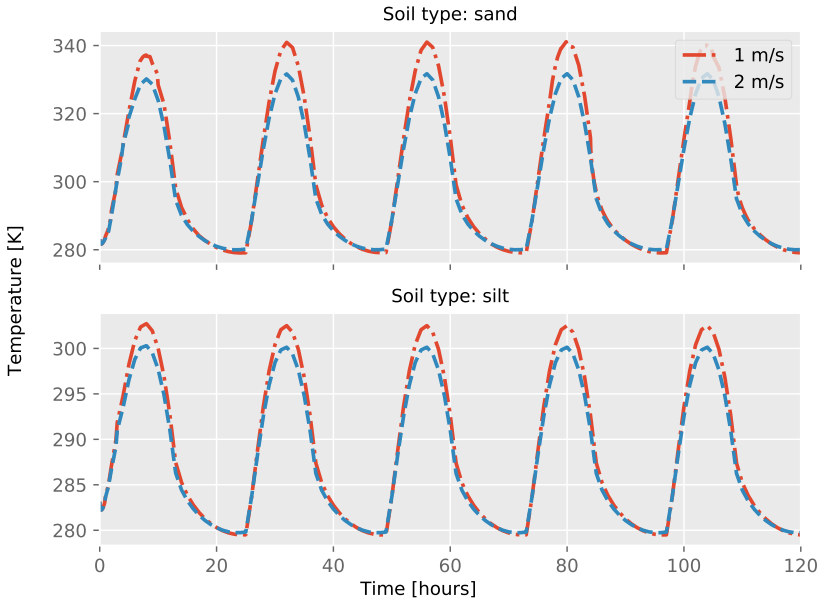

Figure 7.8: Average temperature at the soil surface depending on soil type and velocity over five days.

The temperatures for both soil types are higher for the lower wind velocity. While for the sandy soil this can be explained by the before mentioned conductive heat exchange with

the cooler atmosphere, for the silty soil, additionally the effect of evaporative cooling is greater for higher wind velocities. That is why temperature peaks are lower for the silty soil.

These different temperatures then can also lead to a varying influences on the transport behaviour of methane for the two soil types, which can be seen in Figure 7.9.

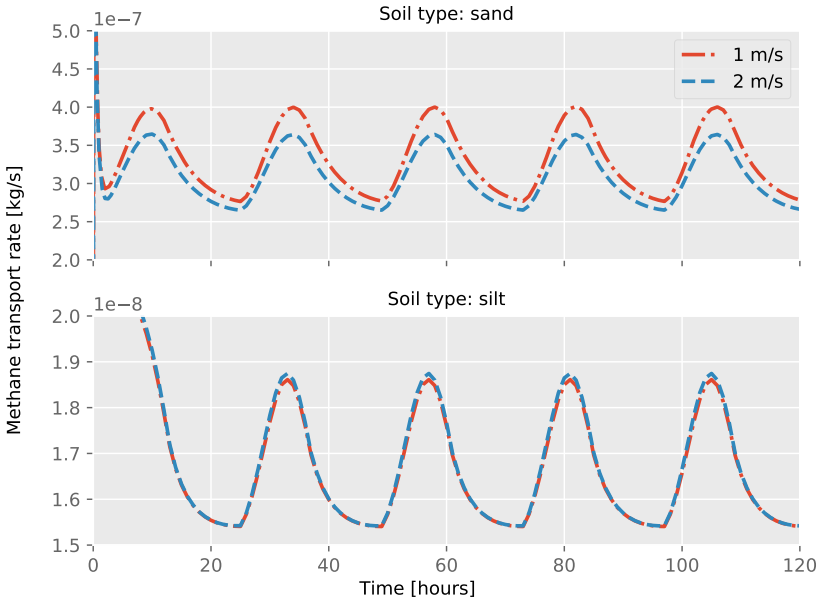

Figure 7.9: Methane rates depending on soil type and velocity over five days.

For the silty soil, the effect of a thinner boundary layer due higher velocities in the free flow is dominating. Methane transport rates are then lower for lower wind velocities. The effect is rather small though as in general the transport is limited by the transport in the porous medium.

However, for the sandy soil, the effect of the temperature difference is dominating. Here, higher wind velocities lead to less transport, as the temperatures at the interface and in the porous medium are lower for higher flow velocities. Therefore, for sandy soil, higher flow velocities result in lower methane transport rates.

7.4 Influence of a surface obstacle

A five centimetre high obstacle is placed at the beginning of the porous medium to evaluate the influence of a diurnal cycle of radiation in such a setting. Again, the transport behaviour in the silty soil and the sandy soil are compared.

Figure 7.10 shows evaporation rates downstream of the porous obstacles for both soil types at three different points in time during a day.

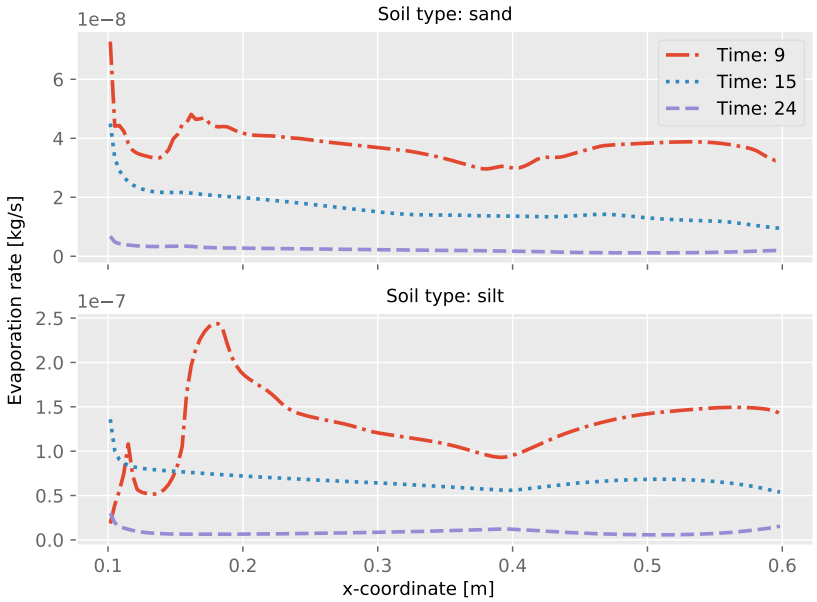

Figure 7.10: Evaporation rate across the interface downstream of the porous obstacle for three different points in time. The obstacle ends at the x-position of 0.1 m after the beginning of the porous medium.

The sandy soil drains very quickly and evaporation rates are in stage-II evaporation. Still, the influence of the surface obstacle is visible. At 9 in the morning, the area close to the obstacle (in the region between 0.1 - 0.15 m) is still in the shade, therefore, evaporation rates are lower there than in the rest of the domain, where the sun heats the soil surface. The dip in the evaporation rate at a position of x = 0.4 m can be explained by the end of the recirculation zone, where temperatures are lower due to more turbulent mixing with the cooler atmosphere. This leads to lower evaporation rates locally. At 3 in the afternoon and in the night, evaporation rates are highest right after the obstacle, which can be explained by the higher water saturation which can also be seen in Figure 7.11.

At 9 a.m. the silty soil is still in stage-I evaporation, which can be seen in the shape of the evaporation curve, that is still governed by the formation of the corner eddy and the recirculation zone downstream of the obstacle. Later, evaporation rates are in a transition from stage-I evaporation to stage-II evaporation. Both at 3 p.m. and at midnight, the capillary pressure is high as the soil is relatively dry already. This leads to a reduction of the vapour pressure and therefore lower evaporation rates.

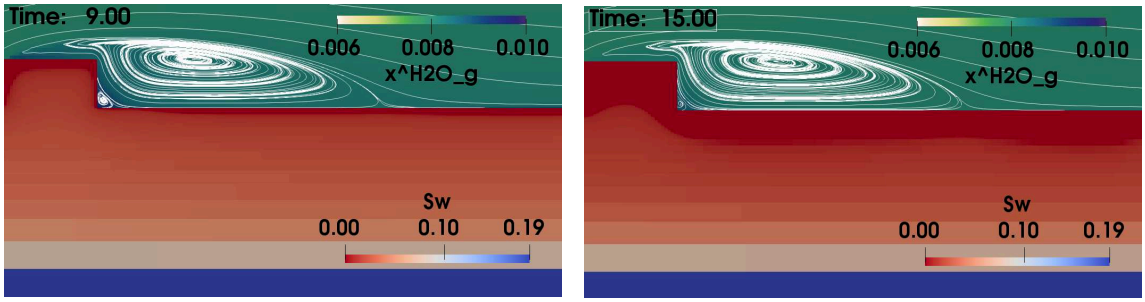

Figure 7.11: Temperature distribution and water saturation in the porous medium at 9 a.m. and 3 p.m. for a set-up of one porous obstacle and a diurnal cycle of radiation.

The methane flux from the porous medium into the free flow downstream of the obstacle can be seen in Figure 7.12.

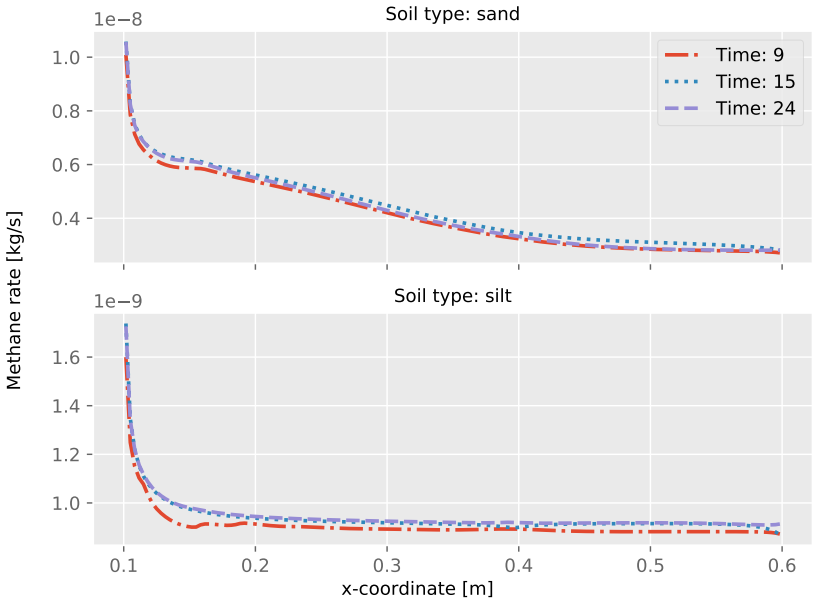

Figure 7.12: Methane transport across the interface downstream of the porous obstacle for three different points in time.

For sandy soil, the shape of the curve is clearly governed by the momentum transfer from the free flow into the soil, which could be observed in the example without radiation in

Chapter 6 as well. Radiation only has a minor influence on the profile, with the lowest transport rates at 9 a.m. and highest rates at 3 p.m., when temperatures are higher. In the morning, it can also be observed that transport rates are lower in the corner right after the obstacle. At 9 a.m. this location is still in the shade, which leads to lower temperatures and less transport. Here, the split of the curves between the different times of the day is highest, as later in the day the transport is increased at this location as well due to the higher temperatures. This temperature difference is also visible in Figure 7.13.

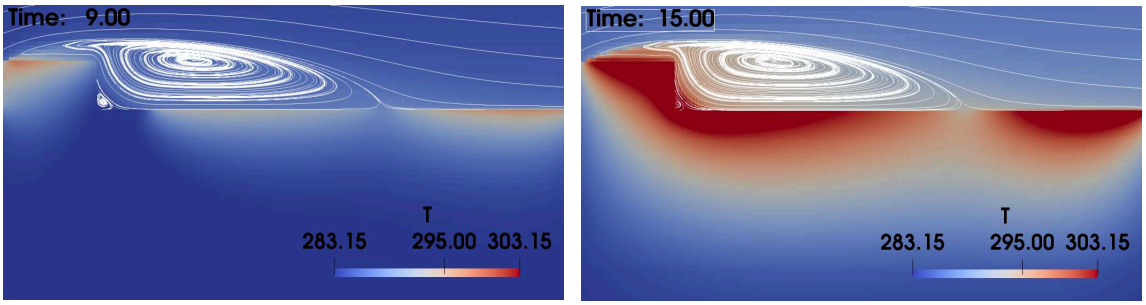

Figure 7.13: Temperature distribution at 9 a.m. and 3 p.m. in the sandy soil.

The silty soil, as before, is not so much influenced by the momentum transfer. Here, the lowest transport rates are also observed for the morning, when temperatures are low and the water saturation is higher. This decreases the effective diffusion coefficients and therefore reduces the diffusive transport through the soil.

7.5 Summary

This analysis of multicomponent transport under the influence of solar radiation shows that radiation and the subsequent temperature changes in the porous medium can have a high influence on the transport of gaseous components from the soil into the atmosphere.

A comparison of a silty soil type with a sandy soil type shows that for the silty soil type the influence of radiation is lower than for sandy soil. One reason is that in the analysed set-up the silty soil is continuously in stage-I evaporation, therefore temperature rises due to solar radiation are limited by evaporative cooling. Additionally, the temperature difference mainly affects diffusive fluxes in the silty soil because advective fluxes are limited due to the low permeability. Therefore, the influence of the temperature on

densities and viscosities does not influence the transport of the components in the soil substantially.

Comparing the influence of a diurnal cycle of radiation on methane and carbon dioxide, it can be seen that both components show enhanced transport rates due to the higher temperatures. Due to the relative high saturation in the analysed set-up, in this case the transport of carbon dioxide in the water phase also plays a role and leads to higher fluxes of carbon dioxide compared to methane. Methane mainly migrates in the gas phase, where the flux is limited due to the low gas saturation.

Analysing different wind speeds and their influence on component transport shows that for different soil types and wind speeds, the diurnal cycle of radiation can have a different impact depending on which effect is dominating. For silty soil, higher wind speeds lead to higher fluxes although the surface temperatures are lower for higher wind velocities. Still, the smaller boundary layer that develops due to the higher wind velocity results in higher diffusive fluxes. For the sandy soil, this effect is not dominating. Here, the higher surface temperature of the lower wind velocity enhances the methane transport in the porous medium, therefore increasing the fluxes of methane into the atmosphere.

The last section evaluates the effect of a surface obstacle. Here, evaporation rates and transport of methane across the interface downstream of the obstacle are analysed for the two different soil types, silt and sand. While evaporation rates are clearly influenced by diurnal cycle of radiation, methane transport is dominated by the momentum transfer from the free flow into the atmosphere and less by the diurnal cycle of radiation. Still, it can be seen that higher temperatures during the day lead to higher transport for both soil types.

8 Summary and Outlook

8.1 Summary

The focus of this work is analysing multicomponent transport between a porous medium and a free flow. Furthermore, radiation is included in the coupling conditions of the two domains, which makes it possible to evaluate the effect of a diurnal cycle of radiation on evaporation and the transport of other gaseous components. This is highly relevant for predicting greenhouse gas emissions and evaporation rates under natural conditions from soil.

The Maxwell-Stefan formulation is implemented in the numerical software tool DuMu$^{\text{x}}$ to describe multicomponent diffusion in the gas and the liquid phase of an unsaturated porous medium and in the free flow. This formulation is applied to calculate diffusive fluxes and used in the transport equations of the free flow and the porous medium as well as in the coupling conditions. The radiation concept is implemented by expanding an existing implementation of a coupled porous-medium free-flow model with an additional term in the coupling conditions. Parametrizations depending on water saturation are used for soil emissivity and soil albedo.

Turbulent free-flow behaviour is described with a RANS approach and the $k-\omega$-turbulence-model. In the porous medium a two-phase multicomponent transport equation using Darcy's law as the momentum balance is applied. The free flow is discretized with a staggered grid scheme, while the porous medium uses a cell-centred TPFA approach. Time discretization is applied with a fully implicit Euler scheme. Both domains are coupled with a monolithic approach. The discretized equations are linearised with Newton's method and solved by a direct linear solver.

Summary of the main results: Three main research topics are analysed in this work. (I) Evaporation under the influence of radiation, where first a comprehensive process analysis is conducted and then model results are compared to experimental results. (II) Multicomponent transport from the porous medium into the atmosphere is investigated, beginning with a process analysis and followed by a benchmark study, where model results are compared to results from the commercially available software COMSOL Multiphysics®. (III) Multicomponent transport is analysed under the influence of a diurnal cycle of radiation. In the following, the main findings are described in more detail.

(I) Analysing evaporation under the influence of a cycle of diurnal radiation shows that evaporation rates exhibit a diurnal cycle as well, both for stage-I evaporation and stage-II evaporation. However, different soil types still strongly influence the transition from stage-I evaporation to stage-II evaporation. The influence of surface obstacles is analysed, showing that the diurnal cycle of evaporation also has a very high impact on the drying process. The height of surface undulations also plays a role as well as the direction of the sun in comparison to the wind direction. A comparison with experimental data taken from lysimeters, shows that the near surface parameters have a high influence on predicting the correct evaporation rates. While stage-I evaporation rates are fairly well approximated, stage-II evaporation rates are not well matched. This shows, that the description of the free flow is able to capture the right boundary layer development and the radiation model describes a diurnal cycle adequately. However, under stage-II evaporation an analysis of different parameters shows that uncertainties in the soil parameters at the interface can lead to drastic changes in evaporation rates. With adapted parameters for the van-Genuchten relationship, simulated and measured evaporation rates can be well matched even for stage-II evaporation.

(II) Multicomponent transport under dry and unsaturated conditions is analysed for the transport of the two main greenhouse gases, methane and carbon dioxide. Apart from a high relevance for environmental aspects, these components are also very interesting to analyse because their fluid properties differ from nitrogen and oxygen, therefore enabling the analysis of the transport behaviour under different conditions. The analysis under dry conditions shows that densities of the gaseous components influence the momentum transfer from the porous medium into the free flow substantially, a result that is also shown experimentally and numerically in Bahlmann et al. [2020]. The analysis presented in this work shows that additionally a change in viscosities can have a high influence on that momentum transfer. Analysing the transport for two different soil types under unsaturated conditions shows that the behaviour of the components can change, depend-

ing on which transport process is dominating. For sandy soil, the momentum transfer from the free flow to the porous medium is dominating, while for silty soil, the diffusive exchange across the boundary layer thickness is more decisive. In the investigated set-up multicomponent diffusion plays a role in predicting oxygen fluxes from the porous medium into the free flow, while methane fluxes and carbon dioxide fluxes out of the porous medium are approximated sufficiently with Fick's law, assuming diluted components. The benchmark study under dry conditions shows that there is an excellent agreement between the implemented version of the Maxwell-Stefan formulation in both software tools. The key processes in a coupled porous-medium free-flow system can be captured by both models.

(III) Investigating multicomponent transport with a diurnal cycle of radiation shows the transport of methane and carbon dioxide is also influenced by solar radiation. Even during night, elevated temperatures in the porous medium due to solar radiation during the day can lead to higher transport rates as densities are lower and diffusion coefficients higher. A comparison of different soil types shows this phenomenon especially for sandy soil. Silty soil dries slower due to a different capillary pressure - saturation relationship and therefore does not exhibit that pronounced temperature changes during day and night. The influence of one porous obstacle is analysed and shows that the transport of the gaseous components is strongly influenced by the momentum transfer from the free flow into the porous medium.

8.2 Outlook

This work analyses multicomponent transport in coupled porous-medium free-flow processes under the focus of radiation and surface roughness. However, there are still some open questions concerning the processes that are involved in transfer of mass, momentum, and energy between a porous medium and a free flow and possible model extensions.

Physical processes and parameters: In order to expand the presented analysis of the transport of multiple components from the soil into the atmosphere to other components, several other aspects can become relevant. Especially of interest are the fluid properties. As previously described for the computation of the liquid diffusion coefficients infinite dilution is assumed. For the presented analysis of methane and carbon dioxide this

approximation will give sufficient results as the main transport of the components is in the gas phase. However, when this analysis should be expanded to other components such as salts, this assumption might not be valid any more. Then also the assumption that mixtures are ideal needs to be questioned. Comparison with fluid properties that are calculated based on thermodynamically consistent relationships will help to gain more insight.

Another aspect that can be included is turbulent pressure pumping, which was found to have a high influence on the transport of gaseous components in high permeability material such as gravels [Maier et al., 2010, Mohr et al., 2016, Laemmel et al., 2017]. These fluctuations occur on a time scale that cannot be captured by current turbulence models and could be included by dispersion concepts.

When analysing a system of methane and carbon dioxide, another aspect that can be included in the evaluation are reactions, especially the oxidation of methane to carbon dioxide. This is e.g. investigated for single phase transport in Ahmadi et al. [2020], Molins et al. [2008], Binning et al. [2007]. Especially when considering longer time scales, this reaction has a strong influence on the transport of the components.

From an environmental perspective, especially focussing on outdoor conditions and assessing the greenhouse gas transport there, another important point would be the inclusion of plants and transpiration [e.g. Koch et al., 2018] or precipitation.

Extension to 3-d domains: In this work all set-ups consider only a 2-d analysis of the processes. However, it is possible that 3-d effects can influence the analysis, especially when analysing experiments in small domains, when wall effects also might play a role. Ahmadi et al. [2020] show that 3-d calculations in a column set-up of multicomponent transport produces better comparisons with experiments. In further work, when more comparisons with experiments are analysed, this extension might have to be taken into account.

Extensions of the numerical model: As previously described the processes close to the interface are decisive for estimating the correct transport of a quantity from the porous medium into the free flow. In Fetzer [2018] it is shown that an interface solver, where an additional degree of freedom at the interface is introduced, can lead to different results than the implementation of the coupling conditions as used in this work. Here, model

results depend on the grid refinement at the interface. Therefore, using an interface solver or a different discretization scheme, where degrees of freedom are available at the interface would make this work less grid dependent and potentially less computationally costly as a coarser grid could be used. Moreover, currently the discretization in the free flow is not adapted to resolve the investigated surface heterogeneities effectively. A locally adaptive grid discretization could improve compu-tational costs by allowing grid refinement close to the porous obstacles while keeping the grid discretization coarse in the rest of the free-flow domain [e.g. Lipp and Helmig, 2020]. Additionally, the radiation model could be generalized to include arbitrary shapes of surface geometries and angles of the sun, potentially with the help of view factors [e.g. Modest, 2013, Saneinejad et al., 2012].

Experimental investigations: Comparison of numerical results with experimental measurements are crucial for evaluating the suitability of the models. In this work, evaporation rates under outdoor conditions are compared to model results. Additionally, experimental results are compared to model results in the benchmark study in a single phase set-up. However, multiphase experiments and a comparison of the model result are still missing and would be and important step to analyse the transport processes more closely.

A Derivation of Fick's law in the mass reference system

This section adds to the derivation of Fick's law in the mass reference system from the Maxwell-Stefan formulation for two components in Chapter 3.1.2. To show that:

$$\nabla X^a = \frac{M^a M^b}{M_{avg}^2}(\nabla \mathrm{x}^a) \tag{A.1}$$

one can begin with the the relationship between mass and mole fractions:

$$x^a = \frac{M_{avg}}{M^a}\mathrm{X}^a \tag{A.2}$$

The gradient of a mole fraction therefore can be split into:

$$\nabla x^a = \nabla(\frac{M_{avg}}{M^a}\mathrm{X}^a) = \frac{\mathrm{X}^a}{M^a}\nabla M_{avg} + \frac{M_{avg}}{M^a}\nabla X^a \tag{A.3}$$

In a binary system the gradient of the average molar mass can be written as $\nabla M_{avg} = \nabla x^a M^a + \nabla x^b M^b$. With $\nabla x^a = -\nabla x^b$, $\nabla M_{avg} = (M^a - M^b)\nabla x^a$.

This can then be used in the above equation to get:

$$\nabla x^a = \frac{\mathrm{X}^a}{M^a}\nabla x^a(M^a - M^b) + \frac{M_{avg}}{M^a}\nabla X^a \tag{A.4}$$

Rearranging leads to:

$$\nabla x^a(1 - \frac{\mathrm{X}^a}{M^a}(M^a - M^b)) = \frac{M_{avg}}{M^a}\nabla X^a \tag{A.5}$$

now using that $1 - X^a = X^b$, this can be written as:

$$\nabla x^a (M^a X^b + M^b X^a) = M_{avg} \nabla X^a \tag{A.6}$$

using again the conversion from mass fraction to mole fraction and rearranging leads to:

$$\nabla x^a (M^a M^b x^b + M^a M^b x^a) = M_{avg}^2 \nabla X^a \tag{A.7}$$

with $x^a + x^b = 1$ this then leads to the equation given before with:

$$\nabla X^a = \frac{M^a M^b}{M_{avg}^2} (\nabla \mathrm{x}^a) \tag{A.8}$$

B Results and discussion - additonal material

B.1 Evaporation and radiation

This section presents additional material for chapter 5.

Figure B.1 shows the boundary conditions and initial conditions for the analysis of a non-flat surface under the influence of solar radiation.

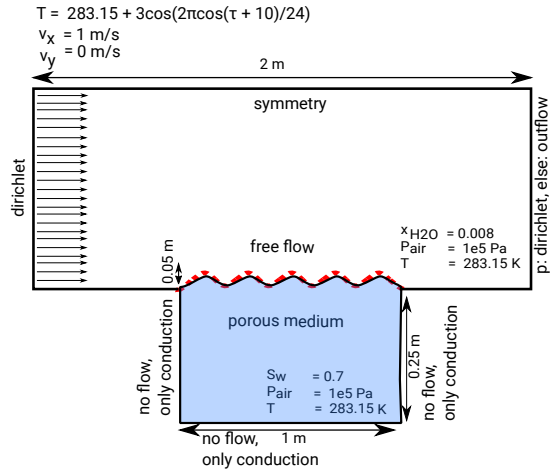

Figure B.1: Initial and boundary conditions for the evaluation of radiation with surface undulations. The set-up is discretized with 270 cells in the horizontal direction and 45 in vertical direction.

Table B.1 shows the spatial parameters as analysed for the first two horizons of the soil Sauerbach (SB-10) of the TERENO SoilCan project. Table 5.1 shows the initial conditions taken from measurement data of the two years that are analysed in chapter 5.2.

parameter	horizon 1	horizon 2	
n	1.5	1.59	[-]
α	7.54332e-5	6.6e-5	[1/Pa]
Snr	0.00814	0.073	[-]
Swr	0.18	0.14	[-]
ϕ	0.376	0.398	[-]
K	1.68e-12	7.7e-14	[m^2]

Table B.1: Spatial parameters for the first two horizons from experimental data for the soil Sb-10.

parameter	2016	2017	
$[x_g^{H_2O}]^{\text{ff}}$	0.001	0.02	[-]
$[p_g]^{\text{ff}}$	1e5	1e5	[Pa]
$[T]^{\text{ff}}$	289.15	291.65	[-]
$[S_w]^{\text{pm}}$	0.757	0.63	[-]
$[T]^{\text{pm}}$	293.15	292.42	[-]

Table B.2: Initial conditions for the two years

B.2 Multicomponent transport

This section presents additional material for chapter 6.

Figure B.2 shows the evaporation rates for silty depending on varying concentration of methane and carbon dioxide present in the soil. The left side shows the transport for the first 10 minutes, while the right shows the transport for 72 hours of drying.

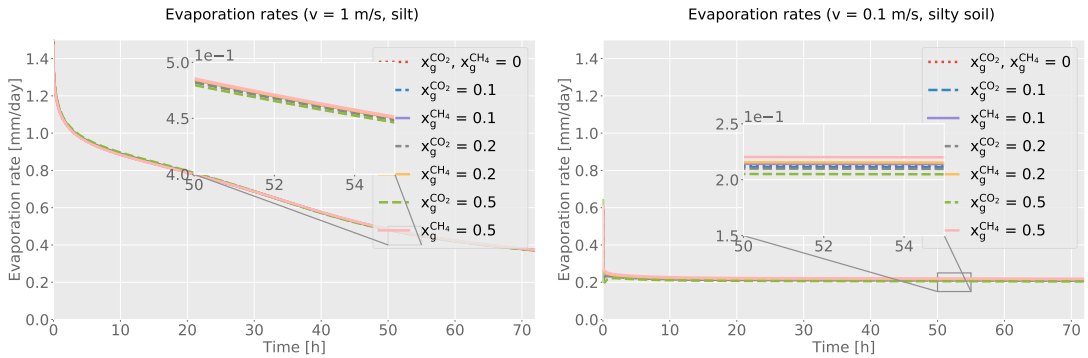

Figure B.2: Evaporation rates of the silty soil dependent on methane and carbon dioxide content.

The diffusion coefficients in Table B.3 are used as constant in the benchmark study for multicomponent diffusion. In Table B.4 the pure component viscosities are presented as they are used in the benchmark. Mixture viscosities are then calculated depending on the concentration.

	D^{ij} $[\mathrm{m^2\,s^{-1}}]$
$CH_4 - O_2$	$2.26 \cdot 10^{-5}$
$CH_4 - CO_2$	$1.71 \cdot 10^{-5}$
$CH_4 - N_2$	$2.14 \cdot 10^{-5}$
$O_2 - CO_2$	$1.64 \cdot 10^{-5}$
$O_2 - N_2$	$2.08 \cdot 10^{-5}$
$CO_2 - N_2$	$1.68 \cdot 10^{-5}$
$H_2 - N_2$	$8.33 \cdot 10^{-5}$
$H_2 - CO_2$	$6.80 \cdot 10^{-5}$

Table B.3: Diffusion coefficients for the benchmark study on multicomponent diffusion.

	μ_g^i [Pa s]
CH_4	$1.09 \cdot 10^{-5}$
O_2	$2.05 \cdot 10^{-5}$
CO_2	$1.47 \cdot 10^{-5}$
N_2	$1.76 \cdot 10^{-5}$

Table B.4: Pure component viscosities for the benchmark study.

Bibliography

N. Ahmadi, K. Mosthaf, C. Scheutz, P. Kjeldsen, and M. Rolle. Model-based interpretation of methane oxidation and respiration processes in landfill biocovers: 3-d simulation of laboratory and pilot experiments. *Waste Management*, 108:160–171, 2020. doi: 10.1016/j.wasman.2020.04.025.

N. Ahmadi, K. Heck, M. Rolle, R. Helmig, and K. Mosthaf. On multicomponent gas diffusion and coupling concepts for porous media and free flow: a benchmark study. *Computational Geosciences*, 2021. doi: 10.1007/s10596-021-10057-y.

J. S. Aronofsky. Effect of gas slip on unsteady flow of gas through porous media. *Journal of Applied Physics*, 25(1):48–53, 1954. doi: 10.1063/1.1721519.

K. Baber, B. Flemisch, and R. Helmig. Modeling drop dynamics at the interface between free and porous-medium flow using the mortar method. *International Journal of Heat and Mass Transfer*, 99:660–671, 2016. doi: 10.1016/j.ijheatmasstransfer.2016.04.014.

L. M. Bahlmann, K. Smits, K. Heck, E. Coltman, R. Helmig, and I. Neuweiler. Gas component transport across the soil-atmosphere-interface for gases of different density: Experiments and modeling. *Water Resources Research*, 2020. doi: 10.1029/2020wr027600.

F. Basirat, P. Sharma, F. Fagerlund, and A. Niemi. Experimental and modeling investigation of CO 2 flow and transport in a coupled domain of porous media and free flow. *International Journal of Greenhouse Gas Control*, 42:461–470, 2015. doi: 10.1016/j.ijggc.2015.08.024.

P. Bastian, M. Blatt, A. Dedner, C. Engwer, R. Klöfkorn, R. Kornhuber, M. Ohlberger, and O. Sander. A generic grid interface for parallel and adaptive scientific computing. Part II: implementation and tests in DUNE. *Computing*, 82(2-3):121–138, 2008a. doi: 10.1007/s00607-008-0004-9.

P. Bastian, M. Blatt, A. Dedner, C. Engwer, R. Klöfkorn, M. Ohlberger, and O. Sander. A generic grid interface for parallel and adaptive scientific computing. Part I: abstract framework. *Computing*, 82(2-3):103–119, 2008b. doi: 10.1007/s00607-008-0003-x.

J. Bear. *Modeling Phenomena of Flow and Transport in Porous Media* -. Springer, Berlin, Heidelberg, 1st ed. 2018 edition, 2018. ISBN 978-3-319-72826-1.

G. S. Beavers and D. D. Joseph. Boundary conditions at a naturally permeable wall. *Journal of Fluid Mechanics*, 30(1):197–207, 1967. doi: 10.1017/s0022112067001375.

P. J. Binning, D. Postma, T. F. Russell, J. A. Wesselingh, and P. F. Boulin. Advective and diffusive contributions to reactive gas transport during pyrite oxidation in the unsaturated zone. *Water Resources Research*, 43(2), 2007. doi: 10.1029/2005WR004474.

R. B. Bird, W. E. Stewart, and E. N. Lightfoot. *Transport Phenomena* -. John Wiley Sons, New York, 2. aufl. edition, 2006. ISBN 978-0-470-11539-8.

J. Boussinesq. *Essai sur la théorie des eaux courantes*. Mémoires présentés par divers savants à l'Académie des sciences de l'Institut national de France. Imprimerie Nationale, 1877.

S. A. Bowers and R. J. Hanks. Reflection of radiant energy from soils. *Soil Science*, 100 (2):130–138, 1965. doi: 10.1097/00010694-196508000-00009.

H. C. Brinkman. A calculation of the viscous force exerted by a flowing fluid on a dense swarm of particles. *Flow, Turbulence and Combustion*, 1(1), 1949. doi: 10.1007/bf02120313.

W. Brutsaert. *Evaporation into the Atmosphere*. Springer, Dordrecht, 1982. ISBN 90-277-1247-6. doi: 10.1007/978-94-017-1497-6.

T. H. Chung, M. Ajlan, L. L. Lee, and K. E. Starling. Generalized multiparameter correlation for nonpolar and polar fluid transport properties. *Industrial & Engineering Chemistry Research*, 27(4):671–679, 1988. doi: 10.1021/ie00076a024.

H. Class. *Theorie und numerische Modellierung nichtisothermer Mehrphasenprozesse in NAPL-kontaminierten porösen Medien*. Dissertation, Technische Universität Braunschweig, 2001.

H. Class, R. Helmig, and P. Bastian. Numerical simulation of non-isothermal multiphase multicomponent processes in porous media. *Advances in Water Resources*, 25(5):533–550, 2002. doi: 10.1016/s0309-1708(02)00014-3.

E. Coltman, M. Lipp, A. Vescovini, and R. Helmig. Obstacles, interfacial forms, and turbulence: A numerical analysis of soil–water evaporation across different interfaces. *Transport in Porous Media*, 2020. doi: 10.1007/s11242-020-01445-6.

E. L. Cussler. *Diffusion: Mass Transfer in Fluid Systems (Cambridge Series in Chemical Engineering)*. Cambridge University Press, 2009. ISBN 0521871212.

H. Darcy. *Les fontaines publiques de la ville de Dijon. Exposition et application des principes à suivre et des formules à employer dans les questions de distribution d'eau: ouvrage terminé par un appendice relatif aux fournitures d'eau de plusieurs villes au filtrage des eaux et à la fabrication des tuyaux de fonte, de plomb, de tole et de bitume.* Dalmont, 1856.

H. Davarzani, K. Smits, R. M. Tolene, and T. Illangasekare. Study of the effect of wind speed on evaporation from soil through integrated modeling of the atmospheric boundary layer and shallow subsurface. *Water Resources Research*, 50(1):661–680, 2014. doi: 10.1002/2013wr013952.

E. L. Davin, S. I. Seneviratne, P. Ciais, A. Olioso, and T. Wang. Preferential cooling of hot extremes from cropland albedo management. *Proceedings of the National Academy of Sciences*, 111(27):9757–9761, 2014. doi: 10.1073/pnas.1317323111.

T. A. Davis. Algorithm 832: Umfpack v4.3—an unsymmetric-pattern multifrontal method. *ACM Trans. Math. Softw.*, 30(2):196–199, 2004. ISSN 0098-3500. doi: 10.1145/992200.992206.

T. C. Deepagoda, K. M. Smits, and C. M. Oldenburg. Effect of subsurface soil moisture variability and atmospheric conditions on methane gas migration in shallow subsurface. *International Journal of Greenhouse Gas Control*, 55:105–117, 2016. doi: 10.1016/j.ijggc.2016.10.016.

T. Defraeye and A. Martynenko. Electrohydrodynamic drying of food: New insights from conjugate modeling. *Journal of Cleaner Production*, 198:269–284, 2018. doi: 10.1016/j.jclepro.2018.06.250.

M. Dimitrov, J. Vanderborght, K. Kostov, B. Debecker, P. Schulze Lammers, L. Damerow, and H. Vereecken. Soil hydraulic parameters of bare soil plots with different soil structure inversely derived from l-band brightness temperatures. *Vadose Zone Journal*, 14, 2015. doi: 10.2136/vzj2014.09.0133.

J. B. Duncan and H. L. Toor. An experimental study of three component gas diffusion. *AIChE Journal*, 8(1):38–41, 1962. doi: 10.1002/aic.690080112.

E. Eggenweiler and I. Rybak. Unsuitability of the Beavers–Joseph interface condition for filtration problems. *Journal of Fluid Mechanics*, 892, 2020. doi: 10.1017/jfm.2020.194.

C.-S. Fen and L. M. Abriola. A comparison of mathematical model formulations for organic vapor transport in porous media. *Advances in Water Resources*, 27(10):1005–1016, 2004. doi: 10.1016/j.advwatres.2004.07.006.

A. Fenghour, W. A. Wakeham, and V. Vesovic. The viscosity of carbon dioxide. *Journal of Physical and Chemical Reference Data*, 27(1):31–44, 1998. doi: 10.1063/1.556013.

R. Fernández-Prini, J. L. Alvarez, and A. H. Harvey. Henry's constants and vapor–liquid distribution constants for gaseous solutes in H2O and D2O at high temperatures. *Journal of Physical and Chemical Reference Data*, 32(2):903–916, 2003. doi: 10.1063/1.1564818.

R. T. Ferrell and D. M. Himmelblau. Diffusion coefficients of nitrogen and oxygen in water. *Journal of chemical and engineering data*, 12(1):111–115, 1967.

T. Fetzer. *Coupled free and porous-medium flow processes affected by turbulence and roughness: models, concepts and analysis*. Dissertation, Universität Stuttgart, 2018.

T. Fetzer, K. M. Smits, and R. Helmig. Effect of turbulence and roughness on coupled porous-medium/free-flow exchange processes. *Transport in Porous Media*, 114(2):395–424, 2016. doi: 10.1007/s11242-016-0654-6.

T. Fetzer, J. Vanderborght, K. Mosthaf, K. M. Smits, and R. Helmig. Heat and water transport in soils and across the soil-atmosphere interface: 2. numerical analysis. *Water Resources Research*, 53(2):1080–1100, 2017. doi: 10.1002/2016wr019983.

A. Fick. Ueber Diffusion. *Annalen der Physik und Chemie*, 170(1):59–86, 1855. doi: 10.1002/andp.18551700105.

B. Flemisch, M. Darcis, K. Erbertseder, B. Faigle, A. Lauser, K. Mosthaf, S. Müthing, P. Nuske, A. Tatomir, M. Wolff, and R. Helmig. DuMux: DUNE for multi-{phase, component, scale, physics, ...} flow and transport in porous media. *Advances in Water Resources*, 34(9):1102–1112, 2011. doi: 10.1016/j.advwatres.2011.03.007.

E. N. Fuller, P. D. Schettler, and J. C. Giddings. New method for prediction of binary gas-phase diffusion coefficients. *Industrial & Engineering Chemistry*, 58(5):18–27, 1966. doi: 10.1021/ie50677a007.

Y. Ganot, M. I. Dragila, and N. Weisbrod. Impact of thermal convection on CO2 flux across the earth–atmosphere boundary in high-permeability soils. *Agricultural and Forest Meteorology*, 184:12–24, 2014. doi: 10.1016/j.agrformet.2013.09.001.

B. Gao, H. Davarzani, R. Helmig, and K. M. Smits. Experimental and numerical study of evaporation from wavy surfaces by coupling free flow and porous media flow. *Water Resources Research*, 54(11):9096–9117, 2018. doi: 10.1029/2018wr023423.

B. Gao, J. Farnsworth, and K. M. Smits. Evaporation from undulating soil surfaces under turbulent airflow through numerical and experimental approaches. *Vadose Zone Journal*, 19(1), 2020. doi: 10.1002/vzj2.20038.

J. Gebert, I. Rachor, A. Gröngröft, and E.-M. Pfeiffer. Temporal variability of soil gas composition in landfill covers. *Waste Management*, 31(5):935–945, 2011. doi: 10.1016/j.wasman.2010.10.007.

C. Gräser and O. Sander. The dune-subgrid module and some applications. *Computing*, 86(4):269–290, 2009. doi: 10.1007/s00607-009-0067-2.

E. Haghighi and D. Or. Evaporation from wavy porous surfaces into turbulent airflows. *Transport in Porous Media*, 110(2):225–250, 2015. ISSN 1573-1634. doi: 10.1007/s11242-015-0512-y 10.1007/s11242-015-0512-y.

E. Haghighi, E. Shahraeeni, P. Lehmann, and D. Or. Evaporation rates across a convective air boundary layer are dominated by diffusion. *Water Resources Research*, 49 (3):1602–1610, 2013. doi: 10.1002/wrcr.20166.

N. S. Hanspal, A. N. Waghode, V. Nassehi, and R. J. Wakeman. Numerical analysis of coupled Stokes/Darcy flows in industrial filtrations. *Transport in Porous Media*, 64 (1):73–101, 2006. doi: 10.1007/s11242-005-1457-3.

F. H. Harlow and J. E. Welch. Numerical calculation of time-dependent viscous incompressible flow of fluid with free surface. *Physics of Fluids*, 8(12):2182, 1965. doi: 10.1063/1.1761178.

K. Heck, E. Coltman, J. Schneider, and R. Helmig. Influence of radiation on evaporation rates: A numerical analysis. *Water Resources Research*, 56(10):e2020WR027332, 2020. doi: 10.1029/2020WR027332. e2020WR027332 10.1029/2020WR027332.

R. Helmig. *Multiphase Flow and Transport Processes in the Subsurface: A Contribution to the Modeling of Hydrosystems*. Springer, 1997. ISBN 0534378439.

J. Herrero and M. J. Polo. Parameterization of atmospheric longwave emissivity in a mountainous site for all sky conditions. *Hydrology and Earth System Sciences*, 16(9): 3139–3147, 2012. doi: 10.5194/hess-16-3139-2012.

J. Hou, F. Simons, and R. Hinkelmann. Improved total variation diminishing schemes for advection simulation on arbitrary grids. *International Journal for Numerical Methods in Fluids*, 70(3):359–382, 2011. doi: 10.1002/fld.2700.

IAPWS. Revised Release on the IAPWS Industrial Formulation 1997 for the Thermodynamic Properties of Water and Steam. `http://www.iapws.org/IF97-Rev.pdf`, 1997.

IPCC. *Climate Change 2013: The Physical Science Basis. Contribution of Working Group I to the Fifth Assessment Report of the Intergovernmental Panel on Climate Change*. Cambridge University Press, Cambridge, United Kingdom and New York, NY, USA, 2013. ISBN ISBN 978-1-107-66182-0. doi: 10.1017/CBO9781107415324. URL `www.climatechange2013.org`.

R. S. Jassal, M. D. Novak, and T. A. Black. Effect of surface layer thickness on simultaneous transport of heat and water in a bare soil and its implications for land surface schemes. *Atmosphere-Ocean*, 41(4):259–272, 2003. doi: 10.3137/ao.410401.

K. Joback. *A Unified Approach to Physical Property Estimation Using Multivariate Statistical Techniques*. Massachusetts Institute of Technology, Department of Chemical Engineering, 1984.

I. P. Jones. Low Reynolds number flow past a porous spherical shell. *Mathematical Proceedings of the Cambridge Philosophical Society*, 73(1):231–238, 1973. doi: 10.1017/S0305004100047642.

W. Kast and C.-R. Hohenthanner. Mass transfer within the gas-phase of porous media. *International Journal of Heat and Mass Transfer*, 43(5):807 – 823, 2000. ISSN 0017-9310. doi: 10.1016/S0017-9310(99)00158-1.

S. Kjelstrup, D. Bedeaux, E. Johannessen, and J. Gross. *Non-equilibrium Thermodynamics for Engineers*. World Scientific Publishing Company, 2010. ISBN 9814322156.

T. Koch, K. Heck, N. Schröder, H. Class, and R. Helmig. A new simulation framework for soil–root interaction, evaporation, root growth, and solute transport. *Vadose Zone Journal*, 17(1):170210, 2018. doi: 10.2136/vzj2017.12.0210.

T. Koch, D. Gläser, K. Weishaupt, S. Ackermann, M. Beck, B. Becker, S. Burbulla, H. Class, E. Coltman, S. Emmert, T. Fetzer, C. Grüninger, K. Heck, J. Hommel, T. Kurz, M. Lipp, F. Mohammadi, S. Scherrer, M. Schneider, G. Seitz, L. Stadler, M. Utz, F. Weinhardt, and B. Flemisch. Dumux 3 – an open-source simulator for solving flow and transport problems in porous media with a focus on model coupling. *Computers & Mathematics with Applications*, 2020. ISSN 0898-1221. doi: 10.1016/j.camwa.2020.02.012.

R. Krishna and J. M. van Baten. The Darken relation for multicomponent diffusion in liquid mixtures of linear alkanes: an investigation using molecular dynamics (MD) simulations. *Industrial & Engineering Chemistry Research*, 44(17):6939–6947, 2005. doi: 10.1021/ie050146c.

R. Krishna and J. Wesselingh. The Maxwell-Stefan approach to mass transfer. *Chemical Engineering Science*, 52(6):861 – 911, 1997. ISSN 0009-2509. doi: 10.1016/S0009-2509(96)00458-7.

T. Laemmel, M. Mohr, H. Schack-Kirchner, D. Schindler, and M. Maier. Direct observation of wind-induced pressure-pumping on gas transport in soil. *Soil Science Society of America Journal*, 81(4):770–774, July 2017. doi: 10.2136/sssaj2017.01.0034n.

P. Lehmann, S. Assouline, and D. Or. Characteristic lengths affecting evaporative drying of porous media. *Phys. Rev. E*, 77:056309, 2008. doi: 10.1103/PhysRevE.77.056309.

P. Linstrom and W. Mallard, editors. *NIST Chemistry WebBook, NIST Standard Reference Database 69*. National Institute of Standards and Technology, Gaithersburg MD, 20899. doi: 10.18434/T4D303.

M. Lipp and R. Helmig. A locally-refined locally-conservative quadtree finite-volume staggered-grid scheme. In G. Lamanna, S. Tonini, G. E. Cossali, and B. Weigand, editors, *Droplet Interactions and Spray Processes*, pages 149–159, Cham, 2020. Springer International Publishing. ISBN 978-3-030-33338-6.

X. Liu, A. Martín-Calvo, E. McGarrity, S. K. Schnell, S. Calero, J.-M. Simon, D. Bedeaux, S. Kjelstrup, A. Bardow, and T. J. H. Vlugt. Fick diffusion coefficients in ternary liquid systems from equilibrium molecular dynamics simulations. *Industrial & Engineering Chemistry Research*, 51(30):10247–10258, 2012. doi: 10.1021/ie301009v.

M. Maier, H. Schack-Kirchner, E. E. Hildebrand, and J. Holst. Pore-space CO2 dynamics in a deep, well-aerated soil. *European Journal of Soil Science*, 61(6):877–887, 2010. doi: 10.1111/j.1365-2389.2010.01287.x.

N. Martys, D. P. Bentz, and E. J. Garboczi. Computer simulation study of the effective viscosity in Brinkman's equation. *Physics of Fluids*, 6(4):1434–1439, 1994. doi: 10.1063/1.868258.

J. Massmann and D. F. Farrier. Effects of atmospheric pressures on gas transport in the vadose zone. *Water Resources Research*, 28(3):777–791, 1992. doi: 10.1029/91wr02766.

A. Matthias, A. Fimbres, E. Sano, D. Post, L. Accioly, A. Batchily, and L. Ferreira. Surface roughness effects on soil albedo. *Soil Science Society of America Journal - SSSAJ*, 64, 2000. doi: 10.2136/sssaj2000.6431035x.

R. J. Millington and J. P. Quirk. Permeability of porous solids. *Transactions of the Faraday Society*, 57:1200, 1961. doi: 10.1039/tf9615701200.

M. F. Modest. Chapter 4 - view factors. In M. F. Modest, editor, *Radiative Heat Transfer (Third Edition)*, pages 129 – 159. Academic Press, Boston, third edition edition, 2013. ISBN 978-0-12-386944-9. doi: 10.1016/B978-0-12-386944-9.50004-2.

M. Mohr, T. Laemmel, M. Maier, and D. Schindler. Analysis of air pressure fluctuations and topsoil gas concentrations within a scots pine forest. *Atmosphere*, 7(10):125, 2016. doi: 10.3390/atmos7100125.

S. Molins, K. U. Mayer, C. Scheutz, and P. Kjeldsen. Transport and reaction processes affecting the attenuation of landfill gas in cover soils. *Journal of Environmental Quality*, 37(2):459–468, 2008. doi: 10.2134/jeq2007.0250.

S. Molins, K. Mayer, R. Amos, and B. Bekins. Vadose zone attenuation of organic compounds at a crude oil spill site — interactions between biogeochemical reactions and multicomponent gas transport. *Journal of Contaminant Hydrology*, 112(1-4):15–29, 2010. doi: 10.1016/j.jconhyd.2009.09.002.

J. L. Monteith. Evaporation and surface temperature. *Quarterly Journal of the Royal Meteorological Society*, 107(451):1–27, 1981. doi: 10.1002/qj.49710745102.

K. Mosthaf. *Modeling and analysis of coupled porous-medium and free flow with application to evaporation processes*. Dissertation, Universität Stuttgart, 2014.

K. Mosthaf, K. Baber, B. Flemisch, R. Helmig, A. Leijnse, I. Rybak, and B. Wohlmuth. A coupling concept for two-phase compositional porous-medium and single-phase compositional free flow. *Water Resources Research*, 47(10), 2011. doi: 10.1029/2011wr010685.

K. Mosthaf, R. Helmig, and D. Or. Modeling and analysis of evaporation processes from porous media on the REV scale. *Water Resources Research*, 50(2):1059–1079, 2014. ISSN 1944-7973. doi: 10.1002/2013WR014442.

Y. Mualem. A new model for predicting the hydraulic conductivity of unsaturated porous media. *Water Resources Research*, 12(3):513–522, 1976. doi: 10.1029/wr012i003p00513.

U. Nachshon, N. Weisbrod, and M. I. Dragila. Quantifying air convection through surface-exposed fractures: A laboratory study. *Vadose Zone Journal*, 7(3):948–956, 2008. doi: 10.2136/vzj2007.0165.

M. Nastev, R. Therrien, R. Lefebvre, and P. Gélinas. Gas production and migration in landfills and geological materials. *Journal of Contaminant Hydrology*, 52(1-4):187–211, 2001. doi: 10.1016/s0169-7722(01)00158-9.

M. D. Novak. *The moisture and thermal regimes of a bare soil in the lower Fraser Valley during spring*. PhD thesis, University of British Columbia, 1981.

M. D. Novak. Dynamics of the near-surface evaporation zone and corresponding effects on the surface energy balance of a drying bare soil. *Agricultural and Forest Meteorology*, 150(10):1358–1365, 2010. doi: 10.1016/j.agrformet.2010.06.005.

J. Ochoa-Tapia and S. Whitaker. Heat transfer at the boundary between a porous medium and a homogeneous fluid. *International Journal of Heat and Mass Transfer*, 40(11):2691–2707, 1997. doi: 10.1016/s0017-9310(96)00250-5.

C. Oertel, J. Matschullat, K. Zurba, F. Zimmermann, and S. Erasmi. Greenhouse gas emissions from soils—a review. *Geochemistry*, 76(3):327–352, 2016. doi: 10.1016/j.chemer.2016.04.002.

C. Oldenburg and A. Unger. Coupled vadose zone and atmospheric surface-layer transport of carbon dioxide from geologic carbon sequestration sites. *Vadose Zone Journal - VADOSE ZONE J*, 3:848–857, 2004. doi: 10.2113/3.3.848.

H. L. Penman and B. A. Keen. Natural evaporation from open water, bare soil and grass. *Proceedings of the Royal Society of London. Series A. Mathematical and Physical Sciences*, 193(1032):120–145, 1948. doi: 10.1098/rspa.1948.0037.

B. E. Poling. *The Properties of Gases and Liquids*. McGraw-Hill Education, 2000. ISBN 0070116822.

D. F. Post, A. Fimbres, A. D. Matthias, E. E. Sano, L. Accioly, A. K. Batchily, and L. Ferreira. Predicting soil albedo from soil color and spectral reflectance data. *Soil Science Society of America Journal*, 64(3):1027–1034, 2000. doi: 10.2136/sssaj2000.6431027x.

T. G. Poulsen. Linking below-surface horizontal pore velocity profiles in porous media with near-surface wind conditions and porous medium gas permeability. *European Journal of Soil Science*, 2019. doi: 10.1111/ejss.12833.

T. G. Poulsen, M. Christophersen, P. Moldrup, and P. Kjeldsen. Modeling lateral gas transport in soil adjacent to old landfill. *Journal of Environmental Engineering*, 127 (2):145–153, 2001. doi: 10.1061/(ASCE)0733-9372(2001)127:2(145).

T. G. Poulsen, M. Christophersen, P. Moldrup, and P. Kjeldsen. Relating landfill gas emissions to atmospheric pressure using numerical modelling and state-space analysis. *Waste Management & Research*, 21(4):356–366, 2003. doi: 10.1177/0734242x0302100408.

T. G. Poulsen, A. Pourber, A. Furman, and K. Papadikis. Relating wind-induced gas exchange to near-surface wind speed characteristics in porous media. *Vadose Zone Journal*, 16(8):vzj2017.02.0039, 2017. doi: 10.2136/vzj2017.02.0039.

A. Pourbakhtiar, T. G. Poulsen, S. Wilkinson, and J. W. Bridge. Effect of wind turbulence on gas transport in porous media: experimental method and preliminary results. *European Journal of Soil Science*, 68(1):48–56, 2017. doi: 10.1111/ejss.12403.

D. Reicosky, W. Dugas, and H. Torbert. Tillage-induced soil carbon dioxide loss from different cropping systems. *Soil and Tillage Research*, 41(1-2):105–118, 1997. doi: 10.1016/s0167-1987(96)01080-x.

S. A. Reinecke and B. E. Sleep. Knudsen diffusion, gas permeability, and water content in an unconsolidated porous medium. *Water Resources Research*, 38(12):16–1–16–15, 2002. doi: 10.1029/2002wr001278.

A. W. Rose and W. Guo. Thermal convection of soil air on hillsides. *Environmental Geology*, 25(4):258–262, 1995. doi: 10.1007/bf00766755.

R. Rosenzweig and U. Shavit. The laminar flow field at the interface of a sierpinski carpet configuration. *Water Resources Research*, 43(10), 2007. doi: 10.1029/2006wr005801.

E. J. Russell and A. Appleyard. The atmosphere of the soil: Its composition and the causes of variation. *The Journal of Agricultural Science*, 7(1):1–48, 1915. doi: 10.1017/s0021859600002410.

P. G. Saffman. On the boundary condition at the surface of a porous medium. *Studies in Applied Mathematics*, 50(2):93–101, 1971. doi: 10.1002/sapm197150293.

S. Saneinejad, P. Moonen, T. Defraeye, D. Derome, and J. Carmeliet. Coupled CFD, radiation and porous media transport model for evaluating evaporative cooling in an urban environment. *Journal of Wind Engineering and Industrial Aerodynamics*, 104-106:455 – 463, 2012. ISSN 0167-6105. doi: 10.1016/j.jweia.2012.02.006. 13th International Conference on Wind Engineering.

H. Schlichting and K. Gersten. *Grenzschicht-Theorie* -. Springer Science and Business Media, Berlin Heidelberg, 2006. ISBN 978-3-540-23004-5.

S. I. Seneviratne, D. Lüthi, M. Litschi, and C. Schär. Land–atmosphere coupling and climate change in Europe. *Nature*, 443(7108):205–209, 2006. doi: 10.1038/nature05095.

E. Shahraeeni, P. Lehmann, and D. Or. Coupling of evaporative fluxes from drying porous surfaces with air boundary layer: Characteristics of evaporation from discrete pores. *Water Resources Research*, 48(9), 2012. doi: 10.1029/2012wr011857.

U. Shavit, R. Rosenzweig, and S. Assouline. Free flow at the interface of porous surfaces: A generalization of the Taylor Brush configuration. *Transport in Porous Media*, 54(3): 345–360, 2004. doi: 10.1023/b:tipm.0000003623.55005.97.

J. B. Silva, D. C. Gaio, L. F. A. Curado, J. D. S. Nogueira, L. C. G. V. Júnior, and T. R. Rodrigues. Evaluation of methods for estimating atmospheric emissivity in Mato-Grossense Cerrado. *Ambiente e Agua - An Interdisciplinary Journal of Applied Science*, 14(3):1, 2019. doi: 10.4136/ambi-agua.2288.

B. E. Sleep. Modeling transient organic vapor transport in porous media with the dusty gas model. *Advances in Water Resources*, 22(3):247–256, 1998. doi: 10.1016/s0309-1708(98)00011-6.

S. Solomon, D. Qin, M. Manning, Z. Chen, M. Marquis, K. Avery, M. Tignor, and H. Miller. *Climate Change 2007: The Physical Science Basis. Working Group I Contribution to the Fourth Assessment Report of the IPCC*, volume 1. 01 2007.

W. Somerton, J. Keese, and S. Chu. Thermal behavior of unconsolidated oil sands. *Society of Petroleum Engineers Journal*, 14(05):513–521, 1974. doi: 10.2118/4506-pa.

R. Span and W. Wagner. A new equation of state for carbon dioxide covering the fluid region from the triple-point temperature to 1100 K at pressures up to 800 MPa. *Journal of physical and chemical reference data*, 25(6):1509–1596, 1996.

L. R. Stingaciu, L. Weihermüller, S. Haber-Pohlmeier, S. Stapf, H. Vereecken, and A. Pohlmeier. Determination of pore size distribution and hydraulic properties using nuclear magnetic resonance relaxometry: A comparative study of laboratory methods. *Water Resources Research*, 46(11), 2010. doi: 10.1029/2009wr008686.

R. Taylor and R. Krishna. *Multicomponent Mass Transfer*. Wiley-Interscience, 1993. ISBN 0471574171.

A. Terzis, I. Zarikos, K. Weishaupt, G. Yang, X. Chu, R. Helmig, and B. Weigand. Microscopic velocity field measurements inside a regular porous medium adjacent to a low Reynolds number channel flow. *Physics of Fluids*, 31(4):042001, 2019. doi: 10.1063/1.5092169.

T. B. Thomasen, C. Scheutz, and P. Kjeldsen. Treatment of landfill gas with low methane content by biocover systems. *Waste Management*, 84:29 – 37, 2019. ISSN 0956-053X. doi: 10.1016/j.wasman.2018.11.011.

W. Thomson. 4. on the equilibrium of vapour at a curved surface of liquid. *Proceedings of the Royal Society of Edinburgh*, 7:63–68, 1872. doi: 10.1017/s0370164600041729.

M. T. van Genuchten. A closed-form equation for predicting the hydraulic conductivity of unsaturated soils. *Soil Science Society of America Journal*, 44(5):892, 1980. doi: 10.2136/sssaj1980.03615995004400050002x.

H. K. Versteeg and W. Malalasekera. *An Introduction to Computational Fluid Dynamics - The Finite Volume Method*. Pearson Education, Amsterdam, 2007. ISBN 978-0-131-27498-3.

A. Vescovini. A fully implicit formulation for Navier-Stokes/Darcy coupling. Master's thesis, Politecnico Milano, 2018.

J. E. Vivian and C. J. King. Diffusivities of slightly soluble gases in water. *AIChE Journal*, 10(2):220–221, 1964. doi: 10.1002/aic.690100217.

S. W. Webb and K. Pruess. The use of Fick's law for modeling trace gas diffusion in porous media. *Transport in Porous Media*, 51(3):327–341, 2003. ISSN 1573-1634. doi: 10.1023/A:1022379016613.

S. Whitaker. Derivation and application of the Stefan-Maxwell equations. *Revista Mexicana de Ingenieria Quimica*, 68:213–243, 2009.

F. M. White. *Fluid Mechanics*. McGraw-Hill Education, New York, 2016. ISBN 978-9-814-72017-5.

D. C. Wilcox. *Turbulence Modeling for CFD (Third Edition)*. D C W Industries, 2006. ISBN 1928729088.

D. C. Wilcox. Formulation of the k-w turbulence model revisited. *AIAA Journal*, 46 (11):2823–2838, 2008. doi: 10.2514/1.36541.

C. R. Wilke. A viscosity equation for gas mixtures. *The Journal of Chemical Physics*, 18(4):517–519, 1950. doi: 10.1063/1.1747673.

P. A. Witherspoon and D. N. Saraf. Diffusion of Methane, Ethane, Propane, and n-Butane in Water from 25 to 43°. *The Journal of Physical Chemistry*, 69(11):3752–3755, 1965. doi: 10.1021/j100895a017.

T. Yamanaka, A. Takeda, and J. Shimada. Evaporation beneath the soil surface: some observational evidence and numerical experiments. *Hydrological Processes*, 12(13-14):2193–2203, 1998. doi: 10.1002/(SICI)1099-1085(19981030)12:13/14¡2193::AID-HYP729¿3.0.CO;2-P.

A. G. Yiotis, I. N. Tsimpanogiannis, A. K. Stubos, and Y. C. Yortsos. Coupling between external and internal mass transfer during drying of a porous medium. *Water Resources Research*, 43(6), 2007. doi: 10.1029/2006WR005558.

S. Zacharias, H. Bogena, L. Samaniego, M. Mauder, R. Fuß, T. Pütz, M. Frenzel, M. Schwank, C. Baessler, K. Butterbach-Bahl, O. Bens, E. Borg, A. Brauer, P. Dietrich, I. Hajnsek, G. Helle, R. Kiese, H. Kunstmann, S. Klotz, J. C. Munch, H. Papen, E. Priesack, H. P. Schmid, R. Steinbrecher, U. Rosenbaum, G. Teutsch, and H. Vereecken. A network of terrestrial environmental observatories in Germany. *Vadose Zone Journal*, 10(3):955–973, 2011. doi: 10.2136/vzj2010.0139.

Institut für Wasser- und Umweltsystemmodellierung
Universität Stuttgart

Pfaffenwaldring 61
70569 Stuttgart (Vaihingen)
Telefon (0711) 685 - 60156
Telefax (0711) 685 - 51073
E-Mail: iws@iws.uni-stuttgart.de
http://www.iws.uni-stuttgart.de

Verzeichnis der Mitteilungshefte

1 Röhnisch, Arthur: *Die Bemühungen um eine Wasserbauliche Versuchsanstalt an der Technischen Hochschule Stuttgart*, und
Fattah Abouleid, Abdel: *Beitrag zur Berechnung einer in lockeren Sand gerammten, zweifach verankerten Spundwand*, 1963

2 Marotz, Günter: *Beitrag zur Frage der Standfestigkeit von dichten Asphaltbelägen im Großwasserbau*, 1964

3 Gurr, Siegfried: *Beitrag zur Berechnung zusammengesetzter ebener Flächentrag-werke unter besonderer Berücksichtigung ebener Stauwände, mit Hilfe von Rand-wert- und Lastwertmatrizen*, 1965

4 Plica, Peter: *Ein Beitrag zur Anwendung von Schalenkonstruktionen im Stahlwasserbau*, und
Petrikat, Kurt: *Möglichkeiten und Grenzen des wasserbaulichen Versuchswesens*, 1966

5 Plate, Erich: *Beitrag zur Bestimmung der Windgeschwindigkeitsverteilung in der durch eine Wand gestörten bodennahen Luftschicht*, und
Röhnisch, Arthur; Marotz, Günter: *Neue Baustoffe und Bauausführungen für den Schutz der Böschungen und der Sohle von Kanälen, Flüssen und Häfen; Gestehungskosten und jeweilige Vorteile*, sowie
Unny, T.E.: *Schwingungsuntersuchungen am Kegelstrahlschieber*, 1967

6 Seiler, Erich: *Die Ermittlung des Anlagenwertes der bundeseigenen Binnenschiffahrtsstraßen und Talsperren und des Anteils der Binnenschiffahrt an diesem Wert*, 1967

7 *Sonderheft anläßlich des 65. Geburtstages von Prof. Arthur Röhnisch mit Beiträgen von* Benk, Dieter; Breitling, J.; Gurr, Siegfried; Haberhauer, Robert; Honekamp, Hermann; Kuz, Klaus Dieter; Marotz, Günter; Mayer-Vorfelder, Hans-Jörg; Miller, Rudolf; Plate, Erich J.; Radomski, Helge; Schwarz, Helmut; Vollmer, Ernst; Wildenhahn, Eberhard; 1967

8 Jumikis, Alfred: *Beitrag zur experimentellen Untersuchung des Wassernachschubs in einem gefrierenden Boden und die Beurteilung der Ergebnisse*, 1968

9 Marotz, Günter: *Technische Grundlagen einer Wasserspeicherung im natürlichen Untergrund*, 1968

10 Radomski, Helge: *Untersuchungen über den Einfluß der Querschnittsform wellenförmiger Spundwände auf die statischen und rammtechnischen Eigenschaften*, 1968

11 Schwarz, Helmut: *Die Grenztragfähigkeit des Baugrundes bei Einwirkung vertikal gezogener Ankerplatten als zweidimensionales Bruchproblem*, 1969

12 Erbel, Klaus: *Ein Beitrag zur Untersuchung der Metamorphose von Mittelgebirgsschneedecken unter besonderer Berücksichtigung eines Verfahrens zur Bestimmung der thermischen Schneequalität*, 1969

13 Westhaus, Karl-Heinz: *Der Strukturwandel in der Binnenschiffahrt und sein Einfluß auf den Ausbau der Binnenschiffskanäle*, 1969

14 Mayer-Vorfelder, Hans-Jörg: *Ein Beitrag zur Berechnung des Erdwiderstandes unter Ansatz der logarithmischen Spirale als Gleitflächenfunktion*, 1970

15 Schulz, Manfred: *Berechnung des räumlichen Erddruckes auf die Wandung kreiszylindrischer Körper*, 1970

16 Mobasseri, Manoutschehr: *Die Rippenstützmauer. Konstruktion und Grenzen ihrer Standsicherheit*, 1970

17 Benk, Dieter: *Ein Beitrag zum Betrieb und zur Bemessung von Hochwasserrückhaltebecken*, 1970

18 Gàl, Attila: *Bestimmung der mitschwingenden Wassermasse bei überströmten Fischbauchklappen mit kreiszylindrischem Staublech*, 1971, vergriffen

19 Kuz, Klaus Dieter: *Ein Beitrag zur Frage des Einsetzens von Kavitationserscheinungen in einer Düsenströmung bei Berücksichtigung der im Wasser gelösten Gase*, 1971, vergriffen

20 Schaak, Hartmut: *Verteilleitungen von Wasserkraftanlagen*, 1971

21 *Sonderheft zur Eröffnung der neuen Versuchsanstalt des Instituts für Wasserbau der Universität Stuttgart mit Beiträgen von* Brombach, Hansjörg; Dirksen, Wolfram; Gàl, Attila; Gerlach, Reinhard; Giesecke, Jürgen; Holthoff, Franz-Josef; Kuz, Klaus Dieter; Marotz, Günter; Minor, Hans-Erwin; Petrikat, Kurt; Röhnisch, Arthur; Rueff, Helge; Schwarz, Helmut; Vollmer, Ernst; Wildenhahn, Eberhard; 1972

22 Wang, Chung-su: *Ein Beitrag zur Berechnung der Schwingungen an Kegelstrahlschiebern*, 1972

23 Mayer-Vorfelder, Hans-Jörg: *Erdwiderstandsbeiwerte nach dem Ohde-Variationsverfahren*, 1972

24 Minor, Hans-Erwin: *Beitrag zur Bestimmung der Schwingungsanfachungsfunktionen überströmter Stauklappen*, 1972, vergriffen

25 Brombach, Hansjörg: *Untersuchung strömungsmechanischer Elemente (Fluidik) und die Möglichkeit der Anwendung von Wirbelkammerelementen im Wasserbau*, 1972, vergriffen

26 Wildenhahn, Eberhard: *Beitrag zur Berechnung von Horizontalfilterbrunnen*, 1972

27 Steinlein, Helmut: *Die Eliminierung der Schwebstoffe aus Flußwasser zum Zweck der unterirdischen Wasserspeicherung, gezeigt am Beispiel der Iller*, 1972

28 Holthoff, Franz Josef: *Die Überwindung großer Hubhöhen in der Binnenschiffahrt durch Schwimmerhebewerke*, 1973

29 Röder, Karl: *Einwirkungen aus Baugrundbewegungen auf trog- und kastenförmige Konstruktionen des Wasser- und Tunnelbaues*, 1973

30 Kretschmer, Heinz: *Die Bemessung von Bogenstaumauern in Abhängigkeit von der Talform*, 1973

31 Honekamp, Hermann: *Beitrag zur Berechnung der Montage von Unterwasserpipelines*, 1973

32 Giesecke, Jürgen: *Die Wirbelkammertriode als neuartiges Steuerorgan im Wasserbau*, und Brombach, Hansjörg: *Entwicklung, Bauformen, Wirkungsweise und Steuereigenschaften von Wirbelkammerverstärkern*, 1974

33 Rueff, Helge: *Untersuchung der schwingungserregenden Kräfte an zwei hintereinander angeordneten Tiefschützen unter besonderer Berücksichtigung von Kavitation*, 1974

34 Röhnisch, Arthur: *Einpreßversuche mit Zementmörtel für Spannbeton - Vergleich der Ergebnisse von Modellversuchen mit Ausführungen in Hüllwellrohren*, 1975

35 *Sonderheft anläßlich des 65. Geburtstages von Prof. Dr.-Ing. Kurt Petrikat mit Beiträgen von*: Brombach, Hansjörg; Erbel, Klaus; Flinspach, Dieter; Fischer jr., Richard; Gàl, Attila; Gerlach, Reinhard; Giesecke, Jürgen; Haberhauer, Robert; Hafner Edzard; Hausenblas, Bernhard; Horlacher, Hans-Burkhard; Hutarew, Andreas; Knoll, Manfred; Krummet, Ralph; Marotz, Günter; Merkle, Theodor; Miller, Christoph; Minor, Hans-Erwin; Neumayer, Hans; Rao, Syamala; Rath, Paul; Rueff, Helge; Ruppert, Jürgen; Schwarz, Wolfgang; Topal-Gökceli, Mehmet; Vollmer, Ernst; Wang, Chung-su; Weber, Hans-Georg; 1975

36 Berger, Jochum: *Beitrag zur Berechnung des Spannungszustandes in rotationssymmetrisch belasteten Kugelschalen veränderlicher Wandstärke unter Gas- und Flüssigkeitsdruck durch Integration schwach singulärer Differentialgleichungen*, 1975

37 Dirksen, Wolfram: *Berechnung instationärer Abflußvorgänge in gestauten Gerinnen mittels Differenzenverfahren und die Anwendung auf Hochwasserrückhaltebecken*, 1976

38 Horlacher, Hans-Burkhard: *Berechnung instationärer Temperatur- und Wärmespannungsfelder in langen mehrschichtigen Hohlzylindern*, 1976

39 Hafner, Edzard: *Untersuchung der hydrodynamischen Kräfte auf Baukörper im Tiefwasserbereich des Meeres*, 1977, ISBN 3-921694-39-6

40 Ruppert, Jürgen: *Über den Axialwirbelkammerverstärker für den Einsatz im Wasserbau*, 1977, ISBN 3-921694-40-X

41 Hutarew, Andreas: *Beitrag zur Beeinflußbarkeit des Sauerstoffgehalts in Fließgewässern an Abstürzen und Wehren*, 1977, ISBN 3-921694-41-8, *vergriffen*

42 Miller, Christoph: *Ein Beitrag zur Bestimmung der schwingungserregenden Kräfte an unterströmten Wehren*, 1977, ISBN 3-921694-42-6

43 Schwarz, Wolfgang: *Druckstoßberechnung unter Berücksichtigung der Radial- und Längsverschiebungen der Rohrwandung*, 1978, ISBN 3-921694-43-4

44 Kinzelbach, Wolfgang: *Numerische Untersuchungen über den optimalen Einsatz variabler Kühlsysteme einer Kraftwerkskette am Beispiel Oberrhein*, 1978, ISBN 3-921694-44-2

45 Barczewski, Baldur: *Neue Meßmethoden für Wasser-Luftgemische und deren Anwendung auf zweiphasige Auftriebsstrahlen*, 1979, ISBN 3-921694-45-0

46 Neumayer, Hans: *Untersuchung der Strömungsvorgänge in radialen Wirbelkammerverstärkern*, 1979, ISBN 3-921694-46-9

47 Elalfy, Youssef-Elhassan: *Untersuchung der Strömungsvorgänge in Wirbelkammerdioden und -drosseln*, 1979, ISBN 3-921694-47-7

48 Brombach, Hansjörg: *Automatisierung der Bewirtschaftung von Wasserspeichern*, 1981, ISBN 3-921694-48-5

49 Geldner, Peter: *Deterministische und stochastische Methoden zur Bestimmung der Selbstdichtung von Gewässern*, 1981, ISBN 3-921694-49-3, *vergriffen*

50 Mehlhorn, Hans: *Temperaturveränderungen im Grundwasser durch Brauchwassereinleitungen*, 1982, ISBN 3-921694-50-7, *vergriffen*

51 Hafner, Edzard: *Rohrleitungen und Behälter im Meer*, 1983, ISBN 3-921694-51-5

52 Rinnert, Bernd: *Hydrodynamische Dispersion in porösen Medien: Einfluß von Dichteunterschieden auf die Vertikalvermischung in horizontaler Strömung*, 1983, ISBN 3-921694-52-3, *vergriffen*

53 Lindner, Wulf: *Steuerung von Grundwasserentnahmen unter Einhaltung ökologischer Kriterien*, 1983, ISBN 3-921694-53-1, *vergriffen*

54 Herr, Michael; Herzer, Jörg; Kinzelbach, Wolfgang; Kobus, Helmut; Rinnert, Bernd: *Methoden zur rechnerischen Erfassung und hydraulischen Sanierung von Grundwasserkontaminationen*, 1983, ISBN 3-921694-54-X

55 Schmitt, Paul: *Wege zur Automatisierung der Niederschlagsermittlung*, 1984, ISBN 3-921694-55-8, *vergriffen*

56 Müller, Peter: *Transport und selektive Sedimentation von Schwebstoffen bei gestautem Abfluß*, 1985, ISBN 3-921694-56-6

57 El-Qawasmeh, Fuad: *Möglichkeiten und Grenzen der Tropfbewässerung unter besonderer Berücksichtigung der Verstopfungsanfälligkeit der Tropfelemente*, 1985, ISBN 3-921694-57-4, *vergriffen*

58 Kirchenbaur, Klaus: *Mikroprozessorgesteuerte Erfassung instationärer Druckfelder am Beispiel seegangsbelasteter Baukörper*, 1985, ISBN 3-921694-58-2

59 Kobus, Helmut (Hrsg.): *Modellierung des großräumigen Wärme- und Schadstofftransports im Grundwasser*, Tätigkeitsbericht 1984/85 (DFG-Forschergruppe an den Universitäten Hohenheim, Karlsruhe und Stuttgart), 1985, ISBN 3-921694-59-0, *vergriffen*

60 Spitz, Karlheinz: *Dispersion in porösen Medien: Einfluß von Inhomogenitäten und Dichteunterschieden*, 1985, ISBN 3-921694-60-4, *vergriffen*

61 Kobus, Helmut: *An Introduction to Air-Water Flows in Hydraulics*, 1985, ISBN 3-921694-61-2

62 Kaleris, Vassilios: *Erfassung des Austausches von Oberflächen- und Grundwasser in horizontalebenen Grundwassermodellen*, 1986, ISBN 3-921694-62-0

63 Herr, Michael: *Grundlagen der hydraulischen Sanierung verunreinigter Porengrundwasserleiter*, 1987, ISBN 3-921694-63-9

64 Marx, Walter: *Berechnung von Temperatur und Spannung in Massenbeton infolge Hydratation*, 1987, ISBN 3-921694-64-7

65 Koschitzky, Hans-Peter: *Dimensionierungskonzept für Sohlbelüfter in Schußrinnen zur Vermeidung von Kavitationsschäden*, 1987, ISBN 3-921694-65-5

66 Kobus, Helmut (Hrsg.): *Modellierung des großräumigen Wärme- und Schadstofftransports im Grundwasser*, Tätigkeitsbericht 1986/87 (DFG-Forschergruppe an den Universitäten Hohenheim, Karlsruhe und Stuttgart) 1987, ISBN 3-921694-66-3

67 Söll, Thomas: *Berechnungsverfahren zur Abschätzung anthropogener Temperaturanomalien im Grundwasser*, 1988, ISBN 3-921694-67-1

68 Dittrich, Andreas; Westrich, Bernd: *Bodenseeufererosion, Bestandsaufnahme und Bewertung*, 1988, ISBN 3-921694-68-X, *vergriffen*

69 Huwe, Bernd; van der Ploeg, Rienk R.: *Modelle zur Simulation des Stickstoffhaushaltes von Standorten mit unterschiedlicher landwirtschaftlicher Nutzung*, 1988, ISBN 3-921694-69-8, *vergriffen*

70 Stephan, Karl: *Integration elliptischer Funktionen*, 1988, ISBN 3-921694-70-1

71 Kobus, Helmut; Zilliox, Lothaire (Hrsg.): *Nitratbelastung des Grundwassers, Auswirkungen der Landwirtschaft auf die Grundwasser- und Rohwasserbeschaffenheit und Maßnahmen zum Schutz des Grundwassers*. Vorträge des deutsch-französischen Kolloquiums am 6. Oktober 1988, Universitäten Stuttgart und Louis Pasteur Strasbourg (Vorträge in deutsch oder französisch, Kurzfassungen zweisprachig), 1988, ISBN 3-921694-71-X

72 Soyeaux, Renald: *Unterströmung von Stauanlagen auf klüftigem Untergrund unter Berücksichtigung laminarer und turbulenter Fließzustände*,1991, ISBN 3-921694-72-8

73 Kohane, Roberto: *Berechnungsmethoden für Hochwasserabfluß in Fließgewässern mit überströmten Vorländern*, 1991, ISBN 3-921694-73-6

74 Hassinger, Reinhard: *Beitrag zur Hydraulik und Bemessung von Blocksteinrampen in flexibler Bauweise*, 1991, ISBN 3-921694-74-4, vergriffen

75 Schäfer, Gerhard: *Einfluß von Schichtenstrukturen und lokalen Einlagerungen auf die Längsdispersion in Porengrundwasserleitern*, 1991, ISBN 3-921694-75-2

76 Giesecke, Jürgen: *Vorträge, Wasserwirtschaft in stark besiedelten Regionen; Umweltforschung mit Schwerpunkt Wasserwirtschaft*, 1991, ISBN 3-921694-76-0

77 Huwe, Bernd: *Deterministische und stochastische Ansätze zur Modellierung des Stickstoffhaushalts landwirtschaftlich genutzter Flächen auf unterschiedlichem Skalenniveau*, 1992, ISBN 3-921694-77-9, vergriffen

78 Rommel, Michael: *Verwendung von Kluftdaten zur realitätsnahen Generierung von Kluftnetzen mit anschließender laminar-turbulenter Strömungsberechnung*, 1993, ISBN 3-92 1694-78-7

79 Marschall, Paul: *Die Ermittlung lokaler Stofffrachten im Grundwasser mit Hilfe von Einbohrloch-Meßverfahren*, 1993, ISBN 3-921694-79-5, vergriffen

80 Ptak, Thomas: *Stofftransport in heterogenen Porenaquiferen: Felduntersuchungen und stochastische Modellierung*, 1993, ISBN 3-921694-80-9, vergriffen

81 Haakh, Frieder: *Transientes Strömungsverhalten in Wirbelkammern,* 1993, ISBN 3-921694-81-7

82 Kobus, Helmut; Cirpka, Olaf; Barczewski, Baldur; Koschitzky, Hans-Peter: *Versuchseinrichtung zur Grundwasser- und Altlastensanierung VEGAS, Konzeption und Programmrahmen*, 1993, ISBN 3-921694-82-5

83 Zang, Weidong: *Optimaler Echtzeit-Betrieb eines Speichers mit aktueller Abflußregenerierung*, 1994, ISBN 3-921694-83-3, vergriffen

84 Franke, Hans-Jörg: *Stochastische Modellierung eines flächenhaften Stoffeintrages und Transports in Grundwasser am Beispiel der Pflanzenschutzmittelproblematik*, 1995, ISBN 3-921694-84-1

85 Lang, Ulrich: *Simulation regionaler Strömungs- und Transportvorgänge in Karstaquiferen mit Hilfe des Doppelkontinuum-Ansatzes: Methodenentwicklung und Parameteridentifikation*, 1995, ISBN 3-921694-85-X, vergriffen

86 Helmig, Rainer: *Einführung in die Numerischen Methoden der Hydromechanik*, 1996, ISBN 3-921694-86-8, vergriffen

87 Cirpka, Olaf: *CONTRACT: A Numerical Tool for Contaminant Transport and Chemical Transformations - Theory and Program Documentation -*, 1996, ISBN 3-921694-87-6

88 Haberlandt, Uwe: *Stochastische Synthese und Regionalisierung des Niederschlages für Schmutzfrachtberechnungen*, 1996, ISBN 3-921694-88-4

89 Croisé, Jean: *Extraktion von flüchtigen Chemikalien aus natürlichen Lockergesteinen mittels erzwungener Luftströmung*, 1996, ISBN 3-921694-89-2, vergriffen

90 Jorde, Klaus: *Ökologisch begründete, dynamische Mindestwasserregelungen bei Ausleitungskraftwerken*, 1997, ISBN 3-921694-90-6, vergriffen

91 Helmig, Rainer: *Gekoppelte Strömungs- und Transportprozesse im Untergrund - Ein Beitrag zur Hydrosystemmodellierung-*, 1998, ISBN 3-921694-91-4, vergriffen

92 Emmert, Martin: *Numerische Modellierung nichtisothermer Gas-Wasser Systeme in porösen Medien,* 1997, ISBN 3-921694-92-2

93 Kern, Ulrich: *Transport von Schweb- und Schadstoffen in staugeregelten Fließgewässern am Beispiel des Neckars*, 1997, ISBN 3-921694-93-0, vergriffen

94 Förster, Georg: *Druckstoßdämpfung durch große Luftblasen in Hochpunkten von Rohrleitungen 1997*, ISBN 3-921694-94-9

95 Cirpka, Olaf: *Numerische Methoden zur Simulation des reaktiven Mehrkomponententransports im Grundwasser*, 1997, ISBN 3-921694-95-7, *vergriffen*

96 Färber, Arne: *Wärmetransport in der ungesättigten Bodenzone: Entwicklung einer thermischen In-situ-Sanierungstechnologie*, 1997, ISBN 3-921694-96-5

97 Betz, Christoph: *Wasserdampfdestillation von Schadstoffen im porösen Medium: Entwicklung einer thermischen In-situ-Sanierungstechnologie*, 1998, SBN 3-921694-97-3

98 Xu, Yichun: *Numerical Modeling of Suspended Sediment Transport in Rivers*, 1998, ISBN 3-921694-98-1, *vergriffen*

99 Wüst, Wolfgang: *Geochemische Untersuchungen zur Sanierung CKW-kontaminierter Aquifere mit Fe(0)-Reaktionswänden,* 2000, ISBN 3-933761-02-2

100 Sheta, Hussam: *Simulation von Mehrphasenvorgängen in porösen Medien unter Einbeziehung von Hysterese-Effekten*, 2000, ISBN 3-933761-03-4

101 Ayros, Edwin: *Regionalisierung extremer Abflüsse auf der Grundlage statistischer Verfahren*, 2000, ISBN 3-933761-04-2, *vergriffen*

102 Huber, Ralf: *Compositional Multiphase Flow and Transport in Heterogeneous Porous Media*, 2000, ISBN 3-933761-05-0

103 Braun, Christopherus: *Ein Upscaling-Verfahren für Mehrphasenströmungen in porösen Medien*, 2000, ISBN 3-933761-06-9

104 Hofmann, Bernd: *Entwicklung eines rechnergestützten Managementsystems zur Beurteilung von Grundwasserschadensfällen*, 2000, ISBN 3-933761-07-7

105 Class, Holger: *Theorie und numerische Modellierung nichtisothermer Mehrphasenprozesse in NAPL-kontaminierten porösen Medien,* 2001, ISBN 3-933761-08-5

106 Schmidt, Reinhard: *Wasserdampf- und Heißluftinjektion zur thermischen Sanierung kontaminierter Standorte*, 2001, ISBN 3-933761-09-3

107 Josef, Reinhold: *Schadstoffextraktion mit hydraulischen Sanierungsverfahren unter Anwendung von grenzflächenaktiven Stoffen*, 2001, ISBN 3-933761-10-7

108 Schneider, Matthias: *Habitat- und Abflussmodellierung für Fließgewässer mit unscharfen Berechnungsansätzen*, 2001, ISBN 3-933761-11-5

109 Rathgeb, Andreas: *Hydrodynamische Bemessungsgrundlagen für Lockerdeckwerke an überströmbaren Erddämmen*, 2001, ISBN 3-933761-12-3

110 Lang, Stefan: *Parallele numerische Simulation instätionärer Probleme mit adaptiven Methoden auf unstrukturierten Gittern*, 2001, ISBN 3-933761-13-1

111 Appt, Jochen; Stumpp Simone: *Die Bodensee-Messkampagne 2001, IWS/CWR Lake Constance Measurement Program 2001*, 2002, ISBN 3-933761-14-X

112 Heimerl, Stephan: *Systematische Beurteilung von Wasserkraftprojekten,* 2002, ISBN 3-933761-15-8, *vergriffen*

113 Iqbal, Amin: *On the Management and Salinity Control of Drip Irrigation,* 2002, ISBN 3-933761-16-6

114 Silberhorn-Hemminger, Annette: *Modellierung von Kluftaquifersystemen: Geostatistische Analyse und deterministisch-stochastische Kluftgenerierung,* 2002, ISBN 3-933761-17-4

115 Winkler, Angela: *Prozesse des Wärme- und Stofftransports bei der In-situ-Sanierung mit festen Wärmequellen,* 2003, ISBN 3-933761-18-2

116 Marx, Walter: *Wasserkraft, Bewässerung, Umwelt - Planungs- und Bewertungsschwerpunkte der Wasserbewirtschaftung,* 2003, ISBN 3-933761-19-0

117 Hinkelmann, Reinhard: *Efficient Numerical Methods and Information-Processing Techniques in Environment Water,* 2003, ISBN 3-933761-20-4

118 Samaniego-Eguiguren, Luis Eduardo: *Hydrological Consequences of Land Use / Land Cover and Climatic Changes in Mesoscale Catchments*, 2003, ISBN 3-933761-21-2

119 Neunhäuserer, Lina: *Diskretisierungsansätze zur Modellierung von Strömungs- und Transportprozessen in geklüftet-porösen Medien*, 2003, ISBN 3-933761-22-0

120 Paul, Maren: *Simulation of Two-Phase Flow in Heterogeneous Poros Media with Adaptive Methods*, 2003, ISBN 3-933761-23-9

121 Ehret, Uwe: *Rainfall and Flood Nowcasting in Small Catchments using Weather Radar*, 2003, ISBN 3-933761-24-7

122 Haag, Ingo: *Der Sauerstoffhaushalt staugeregelter Flüsse am Beispiel des Neckars - Analysen, Experimente, Simulationen -,* 2003, ISBN 3-933761-25-5

123 Appt, Jochen: *Analysis of Basin-Scale Internal Waves in Upper Lake Constance,* 2003, ISBN 3-933761-26-3

124 Hrsg.: Schrenk, Volker; Batereau, Katrin; Barczewski, Baldur; Weber, Karolin und Koschitzky, Hans-Peter: *Symposium Ressource Fläche und VEGAS - Statuskolloquium 2003, 30. September und 1. Oktober 2003,* 2003, ISBN 3-933761-27-1

125 Omar Khalil Ouda: *Optimisation of Agricultural Water Use: A Decision Support System for the Gaza Strip,* 2003, ISBN 3-933761-28-0

126 Batereau, Katrin: *Sensorbasierte Bodenluftmessung zur Vor-Ort-Erkundung von Schadensherden im Untergrund*, 2004, ISBN 3-933761-29-8

127 Witt, Oliver: *Erosionsstabilität von Gewässersedimenten mit Auswirkung auf den Stofftransport bei Hochwasser am Beispiel ausgewählter Stauhaltungen des Oberrheins*, 2004, ISBN 3-933761-30-1

128 Jakobs, Hartmut: *Simulation nicht-isothermer Gas-Wasser-Prozesse in komplexen Kluft-Matrix-Systemen*, 2004, ISBN 3-933761-31-X

129 Li, Chen-Chien: *Deterministisch-stochastisches Berechnungskonzept zur Beurteilung der Auswirkungen erosiver Hochwasserereignisse in Flussstauhaltungen,* 2004, ISBN 3-933761-32-8

130 Reichenberger, Volker; Helmig, Rainer; Jakobs, Hartmut; Bastian, Peter; Niessner, Jennifer: *Complex Gas-Water Processes in Discrete Fracture-Matrix Systems: Up-scaling, Mass-Conservative Discretization and Efficient Multilevel Solution,* 2004, ISBN 3-933761-33-6

131 Hrsg.: Barczewski, Baldur; Koschitzky, Hans-Peter; Weber, Karolin; Wege, Ralf: *VEGAS - Statuskolloquium 2004,* Tagungsband zur Veranstaltung am 05. Oktober 2004 an der Universität Stuttgart, Campus Stuttgart-Vaihingen, 2004, ISBN 3-933761-34-4

132 Asie, Kemal Jabir: *Finite Volume Models for Multiphase Multicomponent Flow through Porous Media*. 2005, ISBN 3-933761-35-2

133 Jacoub, George: *Development of a 2-D Numerical Module for Particulate Contaminant Transport in Flood Retention Reservoirs and Impounded Rivers,* 2004, ISBN 3-933761-36-0

134 Nowak, Wolfgang: *Geostatistical Methods for the Identification of Flow and Transport Parameters in the Subsurface,* 2005, ISBN 3-933761-37-9

135 Süß, Mia: *Analysis of the influence of structures and boundaries on flow and transport processes in fractured porous media*, 2005, ISBN 3-933761-38-7

136 Jose, Surabhin Chackiath: *Experimental Investigations on Longitudinal Dispersive Mixing in Heterogeneous Aquifers,* 2005, ISBN: 3-933761-39-5

137 Filiz, Fulya: *Linking Large-Scale Meteorological Conditions to Floods in Mesoscale Catchments,* 2005, ISBN 3-933761-40-9

138 Qin, Minghao: *Wirklichkeitsnahe und recheneffiziente Ermittlung von Temperatur und Spannungen bei großen RCC-Staumauern*, 2005, ISBN 3-933761-41-7

139 Kobayashi, Kenichiro: *Optimization Methods for Multiphase Systems in the Subsurface - Application to Methane Migration in Coal Mining Areas*, 2005, ISBN 3-933761-42-5

140 Rahman, Md. Arifur: *Experimental Investigations on Transverse Dispersive Mixing in Heterogeneous Porous Media,* 2005, ISBN 3-933761-43-3

141 Schrenk, Volker: *Ökobilanzen zur Bewertung von Altlastensanierungsmaßnahmen,* 2005, ISBN 3-933761-44-1

142 Hundecha, Hirpa Yeshewatesfa: *Regionalization of Parameters of a Conceptual Rainfall-Runoff Model*, 2005, ISBN: 3-933761-45-X

143 Wege, Ralf: *Untersuchungs- und Überwachungsmethoden für die Beurteilung natürlicher Selbstreinigungsprozesse im Grundwasser,* 2005, ISBN 3-933761-46-8

144 Breiting, Thomas: *Techniken und Methoden der Hydroinformatik - Modellierung von komplexen Hydrosystemen im Untergrund*, 2006, ISBN 3-933761-47-6

145 Hrsg.: Braun, Jürgen; Koschitzky, Hans-Peter; Müller, Martin: *Ressource Untergrund: 10 Jahre VEGAS: Forschung und Technologieentwicklung zum Schutz von Grundwasser und Boden,* Tagungsband zur Veranstaltung am 28. und 29. September 2005 an der Universität Stuttgart, Campus Stuttgart-Vaihingen, 2005, ISBN 3-933761-48-4

146 Rojanschi, Vlad: *Abflusskonzentration in mesoskaligen Einzugsgebieten unter Berücksichtigung des Sickerraumes,* 2006, ISBN 3-933761-49-2

147 Winkler, Nina Simone: *Optimierung der Steuerung von Hochwasserrückhaltebeckensystemen,* 2006, ISBN 3-933761-50-6

148 Wolf, Jens: *Räumlich differenzierte Modellierung der Grundwasserströmung alluvialer Aquifere für mesoskalige Einzugsgebiete*, 2006, ISBN: 3-933761-51-4

149 Kohler, Beate: *Externe Effekte der Laufwasserkraftnutzung*, 2006, ISBN 3-933761-52-2

150 Hrsg.: Braun, Jürgen; Koschitzky, Hans-Peter; Stuhrmann, Matthias: *VEGAS-Statuskolloquium 2006,* Tagungsband zur Veranstaltung am 28. September 2006 an der Universität Stuttgart, Campus Stuttgart-Vaihingen, 2006, ISBN 3-933761-53-0

151 Niessner, Jennifer: *Multi-Scale Modeling of Multi-Phase - Multi-Component Processes in Heterogeneous Porous Media*, 2006, ISBN 3-933761-54-9

152 Fischer, Markus: *Beanspruchung eingeerdeter Rohrleitungen infolge Austrocknung bindiger Böden,* 2006, ISBN 3-933761-55-7

153 Schneck, Alexander: *Optimierung der Grundwasserbewirtschaftung unter Berücksichtigung der Belange der Wasserversorgung, der Landwirtschaft und des Naturschutzes*, 2006, ISBN 3-933761-56-5

154 Das, Tapash: *The Impact of Spatial Variability of Precipitation on the Predictive Uncertainty of Hydrological Models,* 2006, ISBN 3-33761-57-3

155 Bielinski, Andreas: *Numerical Simulation of CO_2 sequestration in geological formations*, 2007, ISBN 3-933761-58-1

156 Mödinger, Jens: *Entwicklung eines Bewertungs- und Entscheidungsunterstützungssystems für eine nachhaltige regionale Grundwasserbewirtschaftung*, 2006, ISBN 3-933761-60-3

157 Manthey, Sabine: *Two-phase flow processes with dynamic effects in porous media - parameter estimation and simulation,* 2007, ISBN 3-933761-61-1

158 Pozos Estrada, Oscar: *Investigation on the Effects of Entrained Air in Pipelines,* 2007, ISBN 3-933761-62-X

159 Ochs, Steffen Oliver: *Steam injection into saturated porous media – process analysis including experimental and numerical investigations*, 2007, ISBN 3-933761-63-8

160 Marx, Andreas: *Einsatz gekoppelter Modelle und Wetterradar zur Abschätzung von Niederschlagsintensitäten und zur Abflussvorhersage, 2007,* ISBN 3-933761-64-6

161 Hartmann, Gabriele Maria: *Investigation of Evapotranspiration Concepts in Hydrological Modelling for Climate Change Impact Assessment*, 2007, ISBN 3-933761-65-4

162 Kebede Gurmessa, Tesfaye: *Numerical Investigation on Flow and Transport Characteristics to Improve Long-Term Simulation of Reservoir Sedimentation*, 2007, ISBN 3-933761-66-2

163 Trifković, Aleksandar: *Multi-objective and Risk-based Modelling Methodology for Planning, Design and Operation of Water Supply Systems*, 2007, ISBN 3-933761-67-0

164 Götzinger, Jens: *Distributed Conceptual Hydrological Modelling - Simulation of Climate, Land Use Change Impact and Uncertainty Analysis*, 2007, ISBN 3-933761-68-9

165 Hrsg.: Braun, Jürgen; Koschitzky, Hans-Peter; Stuhrmann, Matthias: *VEGAS – Kolloquium 2007,* Tagungsband zur Veranstaltung am 26. September 2007 an der Universität Stuttgart, Campus Stuttgart-Vaihingen, 2007, ISBN 3-933761-69-7

166 Freeman, Beau: *Modernization Criteria Assessment for Water Resources Planning; Klamath Irrigation Project, U.S.*, 2008, ISBN 3-933761-70-0

167 Dreher, Thomas: *Selektive Sedimentation von Feinstschwebstoffen in Wechselwirkung mit wandnahen turbulenten Strömungsbedingungen*, 2008, ISBN 3-933761-71-9

168 Yang, Wei: *Discrete-Continuous Downscaling Model for Generating Daily Precipitation Time Series*, 2008, ISBN 3-933761-72-7

169 Kopecki, Ianina: *Calculational Approach to FST-Hemispheres for Multiparametrical Benthos Habitat Modelling,* 2008*,* ISBN 3-933761-73-5

170 Brommundt, Jürgen: *Stochastische Generierung räumlich zusammenhängender Niederschlagszeitreihen*, 2008, ISBN 3-933761-74-3

171 Papafotiou, *Alexandros: Numerical Investigations of the Role of Hysteresis in Heterogeneous Two-Phase Flow Systems*, 2008, ISBN 3-933761-75-1

172 He, Yi: *Application of a Non-Parametric Classification Scheme to Catchment Hydrology*, 2008, ISBN 978-3-933761-76-7

173 Wagner, Sven: *Water Balance in a Poorly Gauged Basin in West Africa Using Atmospheric Modelling and Remote Sensing Information*, 2008, ISBN 978-3-933761-77-4

174 Hrsg.: Braun, Jürgen; Koschitzky, Hans-Peter; Stuhrmann, Matthias; Schrenk, Volker: *VEGAS-Kolloquium 2008 Ressource Fläche III*, Tagungsband zur Veranstaltung am 01. Oktober 2008 an der Universität Stuttgart, Campus Stuttgart-Vaihingen, 2008, ISBN 978-3-933761-78-1

175 Patil, Sachin: *Regionalization of an Event Based Nash Cascade Model for Flood Predictions in Ungauged Basins*, 2008, ISBN 978-3-933761-79-8

176 Assteerawatt, Anongnart: *Flow and Transport Modelling of Fractured Aquifers based on a Geostatistical Approach,* 2008, ISBN 978-3-933761-80-4

177 Karnahl, Joachim Alexander: *2D numerische Modellierung von multifraktionalem Schwebstoff- und Schadstofftransport in Flüssen*, 2008, ISBN 978-3-933761-81-1

178 Hiester, Uwe: *Technologieentwicklung zur In-situ-Sanierung der ungesättigten Bodenzone mit festen Wärmequellen,* 2009, ISBN 978-3-933761-82-8

179 Laux, Patrick: *Statistical Modeling of Precipitation for Agricultural Planning in the Volta Basin of West Africa,* 2009, ISBN 978-3-933761-83-5

180 Ehsan, Saqib: *Evaluation of Life Safety Risks Related to Severe Flooding,* 2009, ISBN 978-3-933761-84-2

181 Prohaska, Sandra: *Development and Application of a 1D Multi-Strip Fine Sediment Transport Model for Regulated Rivers,* 2009, ISBN 978-3-933761-85-9

182 Kopp, Andreas: *Evaluation of CO_2 Injection Processes in Geological Formations for Site Screening,* 2009, ISBN 978-3-933761-86-6

183 Ebigbo, Anozie: *Modelling of biofilm growth and its influence on CO_2 and water (two-phase) flow in porous media,* 2009, ISBN 978-3-933761-87-3

184 Freiboth, Sandra: *A phenomenological model for the numerical simulation of multiphase multicomponent processes considering structural alterations of porous media*, 2009, ISBN 978-3-933761-88-0

185 Zöllner, Frank: *Implementierung und Anwendung netzfreier Methoden im Konstruktiven Wasserbau und in der Hydromechanik*, 2009, ISBN 978-3-933761-89-7

186 Vasin, Milos: *Influence of the soil structure and property contrast on flow and transport in the unsaturated zone*, 2010, ISBN 978-3-933761-90-3

187 Li, Jing: *Application of Copulas as a New Geostatistical Tool*, 2010, ISBN 978-3-933761-91-0

188 AghaKouchak, Amir: *Simulation of Remotely Sensed Rainfall Fields Using Copulas*, 2010, ISBN 978-3-933761-92-7

189 Thapa, Pawan Kumar: *Physically-based spatially distributed rainfall runoff modelling for soil erosion estimation*, 2010, ISBN 978-3-933761-93-4

190 Wurms, Sven: *Numerische Modellierung der Sedimentationsprozesse in Retentionsanlagen zur Steuerung von Stoffströmen bei extremen Hochwasserabflussereignissen*, 2011, ISBN 978-3-933761-94-1

191 Merkel, Uwe: *Unsicherheitsanalyse hydraulischer Einwirkungen auf Hochwasserschutzdeiche und Steigerung der Leistungsfähigkeit durch adaptive Strömungsmodellierung*, 2011, ISBN 978-3-933761-95-8

192 Fritz, Jochen: *A Decoupled Model for Compositional Non-Isothermal Multiphase Flow in Porous Media and Multiphysics Approaches for Two-Phase Flow*, 2010, ISBN 978-3-933761-96-5

193 Weber, Karolin (Hrsg.): *12. Treffen junger WissenschaftlerInnen an Wasserbauinstituten*, 2010, ISBN 978-3-933761-97-2

194 Bliefernicht, Jan-Geert: *Probability Forecasts of Daily Areal Precipitation for Small River Basins,* 2011, ISBN 978-3-933761-98-9

195 Hrsg.: Koschitzky, Hans-Peter; Braun, Jürgen: *VEGAS-Kolloquium 2010 In-situ-Sanierung - Stand und Entwicklung Nano und ISCO -,* Tagungsband zur Veranstaltung am 07. Oktober 2010 an der Universität Stuttgart, Campus Stuttgart-Vaihingen*,* 2010*,* ISBN 978-3-933761-99-6

196 Gafurov, Abror: *Water Balance Modeling Using Remote Sensing Information - Focus on Central Asia,* 2010, ISBN 978-3-942036-00-9

197 Mackenberg, Sylvia: *Die Quellstärke in der Sickerwasserprognose: Möglichkeiten und Grenzen von Labor- und Freilanduntersuchungen,* 2010, ISBN 978-3-942036-01-6

198 Singh, Shailesh Kumar: *Robust Parameter Estimation in Gauged and Ungauged Basins,* 2010, ISBN 978-3-942036-02-3

199 Doğan, Mehmet Onur: *Coupling of porous media flow with pipe flow,* 2011, ISBN 978-3-942036-03-0

200 Liu, Min: *Study of Topographic Effects on Hydrological Patterns and the Implication on Hydrological Modeling and Data Interpolation,* 2011, ISBN 978-3-942036-04-7

201 Geleta, Habtamu Itefa: *Watershed Sediment Yield Modeling for Data Scarce Areas,* 2011, ISBN 978-3-942036-05-4

202 Franke, Jörg: *Einfluss der Überwachung auf die Versagenswahrscheinlichkeit von Staustufen,* 2011, ISBN 978-3-942036-06-1

203 Bakimchandra, Oinam: *Integrated Fuzzy-GIS approach for assessing regional soil erosion risks,* 2011, ISBN 978-3-942036-07-8

204 Alam, Muhammad Mahboob: *Statistical Downscaling of Extremes of Precipitation in Mesoscale Catchments from Different RCMs and Their Effects on Local Hydrology,* 2011, ISBN 978-3-942036-08-5

205 Hrsg.: Koschitzky, Hans-Peter; Braun, Jürgen: *VEGAS-Kolloquium 2011 Flache Geothermie - Perspektiven und Risiken,* Tagungsband zur Veranstaltung am 06. Oktober 2011 an der Universität Stuttgart, Campus Stuttgart-Vaihingen*,* 2011*,* ISBN 978-3-933761-09-2

206 Haslauer, Claus: *Analysis of Real-World Spatial Dependence of Subsurface Hydraulic Properties Using Copulas with a Focus on Solute Transport Behaviour,* 2011, ISBN 978-3-942036-10-8

207 Dung, Nguyen Viet: *Multi-objective automatic calibration of hydrodynamic models – development of the concept and an application in the Mekong Delta,* 2011, ISBN 978-3-942036-11-5

208 Hung, Nguyen Nghia: *Sediment dynamics in the floodplain of the Mekong Delta, Vietnam,* 2011, ISBN 978-3-942036-12-2

209 Kuhlmann, Anna: *Influence of soil structure and root water uptake on flow in the unsaturated zone,* 2012, ISBN 978-3-942036-13-9

210 Tuhtan, Jeffrey Andrew: *Including the Second Law Inequality in Aquatic Ecodynamics: A Modeling Approach for Alpine Rivers Impacted by Hydropeaking,* 2012, ISBN 978-3-942036-14-6

211 Tolossa, Habtamu: *Sediment Transport Computation Using a Data-Driven Adaptive Neuro-Fuzzy Modelling Approach,* 2012, ISBN 978-3-942036-15-3

212 Tatomir, Alexandru-Bodgan: *From Discrete to Continuum Concepts of Flow in Fractured Porous Media,* 2012, ISBN 978-3-942036-16-0

213 Erbertseder, Karin: *A Multi-Scale Model for Describing Cancer-Therapeutic Transport in the Human Lung,* 2012, ISBN 978-3-942036-17-7

214 Noack, Markus: *Modelling Approach for Interstitial Sediment Dynamics and Reproduction of Gravel Spawning Fish,* 2012, ISBN 978-3-942036-18-4

215 De Boer, Cjestmir Volkert: *Transport of Nano Sized Zero Valent Iron Colloids during Injection into the Subsurface*, 2012, ISBN 978-3-942036-19-1

216 Pfaff, Thomas: *Processing and Analysis of Weather Radar Data for Use in Hydrology*, 2013, ISBN 978-3-942036-20-7

217 Lebrenz, Hans-Henning: *Addressing the Input Uncertainty for Hydrological Modeling by a New Geostatistical Method*, 2013, ISBN 978-3-942036-21-4

218 Darcis, Melanie Yvonne: *Coupling Models of Different Complexity for the Simulation of CO_2 Storage in Deep Saline Aquifers*, 2013, ISBN 978-3-942036-22-1

219 Beck, Ferdinand: *Generation of Spatially Correlated Synthetic Rainfall Time Series in High Temporal Resolution - A Data Driven Approach*, 2013, ISBN 978-3-942036-23-8

220 Guthke, Philipp: *Non-multi-Gaussian spatial structures: Process-driven natural genesis, manifestation, modeling approaches, and influences on dependent processes*, 2013, ISBN 978-3-942036-24-5

221 Walter, Lena: *Uncertainty studies and risk assessment for CO_2 storage in geological formations*, 2013, ISBN 978-3-942036-25-2

222 Wolff, Markus: *Multi-scale modeling of two-phase flow in porous media including capillary pressure effects,* 2013, ISBN 978-3-942036-26-9

223 Mosthaf, Klaus Roland: *Modeling and analysis of coupled porous-medium and free flow with application to evaporation processes,* 2014, ISBN 978-3-942036-27-6

224 Leube, Philipp Christoph: *Methods for Physically-Based Model Reduction in Time: Analysis, Comparison of Methods and Application*, 2013, ISBN 978-3-942036-28-3

225 Rodríguez Fernández, Jhan Ignacio: *High Order Interactions among environmental variables: Diagnostics and initial steps towards modeling*, 2013, ISBN 978-3-942036-29-0

226 Eder, Maria Magdalena: *Climate Sensitivity of a Large Lake*, 2013, ISBN 978-3-942036-30-6

227 Greiner, Philipp: *Alkoholinjektion zur In-situ-Sanierung von CKW Schadensherden in Grundwasserleitern: Charakterisierung der relevanten Prozesse auf unterschiedlichen Skalen*, 2014, ISBN 978-3-942036-31-3

228 Lauser, Andreas: *Theory and Numerical Applications of Compositional Multi-Phase Flow in Porous Media*, 2014, ISBN 978-3-942036-32-0

229 Enzenhöfer, Rainer: *Risk Quantification and Management in Water Production and Supply Systems*, 2014, ISBN 978-3-942036-33-7

230 Faigle, Benjamin: *Adaptive modelling of compositional multi-phase flow with capillary pressure*, 2014, ISBN 978-3-942036-34-4

231 Oladyshkin, Sergey: *Efficient modeling of environmental systems in the face of complexity and uncertainty*, 2014, ISBN 978-3-942036-35-1

232 Sugimoto, Takayuki: *Copula based Stochastic Analysis of Discharge Time Series*, 2014, ISBN 978-3-942036-36-8

233 Koch, Jonas: *Simulation, Identification and Characterization of Contaminant Source Architectures in the Subsurface*, 2014, ISBN 978-3-942036-37-5

234 Zhang, Jin: *Investigations on Urban River Regulation and Ecological Rehabilitation Measures, Case of Shenzhen in China*, 2014, ISBN 978-3-942036-38-2

235 Siebel, Rüdiger: *Experimentelle Untersuchungen zur hydrodynamischen Belastung und Standsicherheit von Deckwerken an überströmbaren Erddämmen,* 2014, ISBN 978-3-942036-39-9

236 Baber, Katherina: *Coupling free flow and flow in porous media in biological and technical applications: From a simple to a complex interface description,* 2014, ISBN 978-3-942036-40-5

237 Nuske, Klaus Philipp: *Beyond Local Equilibrium — Relaxing local equilibrium assumptions in multiphase flow in porous media,* 2014, ISBN 978-3-942036-41-2

238 Geiges, Andreas: *Efficient concepts for optimal experimental design in nonlinear environmental systems*, 2014, ISBN 978-3-942036-42-9

239 Schwenck, Nicolas: *An XFEM-Based Model for Fluid Flow in Fractured Porous Media*, 2014, ISBN 978-3-942036-43-6

240 Chamorro Chávez, Alejandro: *Stochastic and hydrological modelling for climate change prediction in the Lima region, Peru*, 2015, ISBN 978-3-942036-44-3

241 Yulizar: *Investigation of Changes in Hydro-Meteorological Time Series Using a Depth-Based Approach*, 2015, ISBN 978-3-942036-45-0

242 Kretschmer, Nicole: *Impacts of the existing water allocation scheme on the Limarí watershed – Chile, an integrative approach*, 2015, ISBN 978-3-942036-46-7

243 Kramer, Matthias: *Luftbedarf von Freistrahlturbinen im Gegendruckbetrieb*, 2015, ISBN 978-3-942036-47-4

244 Hommel, Johannes: *Modeling biogeochemical and mass transport processes in the subsurface: Investigation of microbially induced calcite precipitation*, 2016, ISBN 978-3-942036-48-1

245 Germer, Kai: *Wasserinfiltration in die ungesättigte Zone eines makroporösen Hanges und deren Einfluss auf die Hangstabilität*, 2016, ISBN 978-3-942036-49-8

246 Hörning, Sebastian: *Process-oriented modeling of spatial random fields using copulas*, 2016, ISBN 978-3-942036-50-4

247 Jambhekar, Vishal: *Numerical modeling and analysis of evaporative salinization in a coupled free-flow porous-media system,* 2016, ISBN 978-3-942036-51-1

248 Huang, Yingchun: *Study on the spatial and temporal transferability of conceptual hydrological models*, 2016, ISBN 978-3-942036-52-8

249 Kleinknecht, Simon Matthias: *Migration and retention of a heavy NAPL vapor and remediation of the unsaturated zone*, 2016, ISBN 978-3-942036-53-5

250 Kwakye, Stephen Oppong: *Study on the effects of climate change on the hydrology of the West African sub-region*, 2016, ISBN 978-3-942036-54-2

251 Kissinger, Alexander: *Basin-Scale Site Screening and Investigation of Possible Impacts of CO_2 Storage on Subsurface Hydrosystems*, 2016, ISBN 978-3-942036-55-9

252 Müller, Thomas: *Generation of a Realistic Temporal Structure of Synthetic Precipitation Time Series for Sewer Applications*, 2017, ISBN 978-3-942036-56-6

253 Grüninger, Christoph: *Numerical Coupling of Navier-Stokes and Darcy Flow for Soil-Water Evaporation*, 2017, ISBN 978-3-942036-57-3

254 Suroso: *Asymmetric Dependence Based Spatial Copula Models: Empirical Investigations and Consequences on Precipitation Fields*, 2017, ISBN 978-3-942036-58-0

255 Müller, Thomas; Mosthaf, Tobias; Gunzenhauser, Sarah; Seidel, Jochen; Bárdossy, András: *Grundlagenbericht Niederschlags-Simulator (NiedSim3)*, 2017, ISBN 978-3-942036-59-7

256 Mosthaf, Tobias: *New Concepts for Regionalizing Temporal Distributions of Precipitation and for its Application in Spatial Rainfall Simulation,* 2017, ISBN 978-3-942036-60-3

257 Fenrich, Eva Katrin: *Entwicklung eines ökologisch-ökonomischen Vernetzungsmodells für Wasserkraftanlagen und Mehrzweckspeicher,* 2018, ISBN 978-3-942036-61-0

258 Schmidt, Holger: *Microbial stabilization of lotic fine sediments*, 2018, ISBN 978-3-942036-62-7

259 Fetzer, Thomas: *Coupled Free and Porous-Medium Flow Processes Affected by Turbulence and Roughness – Models, Concepts and Analysis*, 2018, ISBN 978-3-942036-63-4

260 Schröder, Hans Christoph: *Large-scale High Head Pico Hydropower Potential Assessment*, 2018, ISBN 978-3-942036-64-1

261 Bode, Felix: *Early-Warning Monitoring Systems for Improved Drinking Water Resource Protection*, 2018, ISBN 978-3-942036-65-8

262 Gebler, Tobias: *Statistische Auswertung von simulierten Talsperrenüberwachungsdaten zur Identifikation von Schadensprozessen an Gewichtsstaumauern*, 2018, ISBN 978-3-942036-66-5

263 Harten, Matthias von: *Analyse des Zuppinger-Wasserrades – Hydraulische Optimierungen unter Berücksichtigung ökologischer Aspekte*, 2018, ISBN 978-3-942036-67-2

264 Yan, Jieru: *Nonlinear estimation of short time precipitation using weather radar and surface observations*, 2018, ISBN 978-3-942036-68-9

265 Beck, Martin: *Conceptual approaches for the analysis of coupled hydraulic and geomechanical processes*, 2019, ISBN 978-3-942036-69-6

266 Haas, Jannik: *Optimal planning of hydropower and energy storage technologies for fully renewable power systems*, 2019, ISBN 978-3-942036-70-2

267 Schneider, Martin: *Nonlinear Finite Volume Schemes for Complex Flow Processes and Challenging Grids*, 2019, ISBN 978-3-942036-71-9

268 Most, Sebastian Christopher: *Analysis and Simulation of Anomalous Transport in Porous Media*, 2019, ISBN 978-3-942036-72-6

269 Buchta, Rocco: *Entwicklung eines Ziel- und Bewertungssystems zur Schaffung nachhaltiger naturnaher Strukturen in großen sandgeprägten Flüssen des norddeutschen Tieflandes*, 2019, ISBN 978-3-942036-73-3

270 Thom, Moritz: *Towards a Better Understanding of the Biostabilization Mechanisms of Sediment Beds*, 2019, ISBN 978-3-942036-74-0

271 Stolz, Daniel: *Die Nullspannungstemperatur in Gewichtsstaumauern unter Berücksichtigung der Festigkeitsentwicklung des Betons*, 2019, ISBN 978-3-942036-75-7

272 Rodriguez Pretelin, Abelardo: *Integrating transient flow conditions into groundwater well protection*, 2020, ISBN: 978-3-942036-76-4

273 Weishaupt, Kilian: *Model Concepts for Coupling Free Flow with Porous Medium Flow at the Pore-Network Scale: From Single-Phase Flow to Compositional Non-Isothermal Two-Phase Flow*, 2020, ISBN: 978-3-942036-77-1

274 Koch, Timo: *Mixed-dimension models for flow and transport processes in porous media with embedded tubular network systems*, 2020, ISBN: 978-3-942036-78-8

275 Gläser, Dennis: *Discrete fracture modeling of multi-phase flow and deformation in fractured poroelastic media*, 2020, ISBN: 978-3-942036-79-5

276 Seitz, Lydia: *Development of new methods to apply a multi-parameter approach – A first step towards the determination of colmation*, 2020, ISBN: 978-3-942036-80-1

277 Ebrahim Bakhshipour, Amin: *Optimizing hybrid decentralized systems for sustainable urban drainage infrastructures planning*, 2021, ISBN: 978-3-942036-81-8

278 Seitz, Gabriele: *Modeling Fixed-Bed Reactors for Thermochemical Heat Storage with the Reaction System CaO/Ca(OH)$_2$*, 2021, ISBN: 978-3-942036-82-5

279 Emmert, Simon: *Developing and Calibrating a Numerical Model for Microbially Enhanced Coal-Bed Methane Production*, 2021, ISBN: 978-3-942036-83-2

280 Heck, Katharina Klara: *Modelling and analysis of multicomponent transport at the interface between free- and porous-medium flow - influenced by radiation and roughness*, 2021, ISBN: 978-3-942036-84-9

Die Mitteilungshefte ab der Nr. 134 (Jg. 2005) stehen als pdf-Datei über die Homepage des Instituts: www.iws.uni-stuttgart.de zur Verfügung.